Structural and Functional Studies of Picornaviruses

Ling Zhu

St Cross College

and

Division of Structural Biology

Nuffield Department of Medicine

University of Oxford

A thesis submitted in partial fulfillment for

the degree of Doctor of Philosophy

Trinity Term 2017

Contents

Detailed contents

List of figures

List of tables

Structural and Functional Studies of Picornaviruses

Ling Zhu

St Cross College and Division of Structural Biology

Nuffield Department of Medicine, University of Oxford

Trinity Term 2017

Abstract

Picornaviruses are responsible for a variety of human and animal diseases, ranging from hepatitis A, foot and mouth disease, through polio to hand-foot-and-mouth disease and the common cold. In addition to their importance in causing diseases, they also serve as models for understanding the basic mechanisms of host-pathogen interactions, virus entry and viral genome release.

Although the structure of a number of picornaviruses from the *Entero, Cardio, Aphtho* and *Senecavirus* genera have been determined at close to atomic resolution with X-ray crystallography, structural and functional studies on *Parecho, Kobu and Hepatovirus* are very limited. I have thus studied members of these genera: Ljungan virus, Aichi virus and hepatitis A virus to further understanding of the molecular basis of pathogenesis, viral entry, assembly and stability for these viruses in particular and for picornaviruses in general. In addition I have studied the VLPs of

CVA16 as potential vaccine candidates.

The atomic structure of Ljungan virus determined by cryo-EM, shows remarkable features, including an extended VP1 C-terminus, forming a major protuberance on the outer surface of the virus, and a basic motif at the N-terminus of VP3, which orders some 12% of the viral genome. This charge-driven RNA attachment suggests that this branch of the picornaviruses use a different mechanism of genome encapsidation.

The cryo-EM structure of Aichi virus at 3.7 Å resolution is intermediate between the enteroviruses and cardioviruses. On the outer surface a polyproline helix structure, not seen previously in picornaviruses is present at the C-terminus of VP1, corresponding to the position where integrin binding motifs are found in some other picornaviruses. A peptide corresponding to this polyproline motif somewhat attenuates virus infectivity suggesting a role in attachment to a cellular receptor.

The cryo-EM structure of a complex between hepatitis A virus and a potent neutralizing antibody, together with other data suggest that this antibody mimics receptor binding.

2A proteins from Ljungan virus, Sebokele virus and human parechovirus play a different role in these viruses compared to other members of the picornavirus family and the X-ray structures of these proteins reveal incredible plasticity and an H-box

motif that may not be catalytically active.

In summary, this thesis provides an insight into some important aspects of host-virus interactions especially the events occurring during viral assembly and receptor recognition.

Abbreviations

Å	Ångstrom (10^{-10} m)
AEV	avian encephalomyelitis virus
AiV	aichivirus
BEV	bovine enterovirus
BSA	bovine serum albumin
CD	circular dichroism
cDNA	complementary deoxyribonucleic acid
CAR	coxsackievirus and adenovirus receptor
CrPV	cricket paralysis virus
CVB	coxsackievirus B
CVA16	coxsackievirus A16
CPE	cytopathic effect
CTF	contrast transfer function
DMEM	Dulbecco's modified Eagle's medium
DNA	deoxyribonucleic acid
ELISA	enzyme-linked immunosorbent assay
EM	electron microscopy
ERAV	equine rhinitis A virus
EV71	enterovirus A71

FBS	fetal bovine serum
FMDV	foot-and-mouth disease virus
FSC	Fourier shell correlation
GMK	green monkey kidney
GSH	reduced glutathione
HAV	hepatitis A virus
HFMD	hand foot and mouth disease
HPeV	human parechovirus
HRP	horseradish peroxidase
HRV	human rhinovirus
IC50	concentration of 50 % inhibition
ICAM-1	intercelluar adhesion molecule 1
IgG	immunoglobulin G
IPTG	isopropyl β-D-1-thiogalactopyranoside
IPV	inactivated poliovirus vaccine
LDLR	low density lipoprotein receptor
LLG	log-likelihood
LV	ljungan virus
MAbs	monoclonal antibodies
MEV	mengo virus

MOI	multiplicity of infection
MOPV	monovalent oral poliovirus vaccine
NCS	non-crystallographic symmetry
OD	optical density
PaSTRy	particle stability thermal release assay
PBS	phosphate-buffered saline
PCR	polymerase chain reaction
PEG	polyethylene glycol
p.i.	post infection
PLA2	phospholipase 2
PPII helix	poly-L-proline type II helix
PSGL-1	human P-selectin glycoprotein ligand-1
PV	poliovirus
PVr	poliovirus receptor
RNA	ribonucleic acid
Rmsd	root mean square deviation
RT-PCR	reverse transcription-polymerase chain reaction
SCARB2	scavenger receptor class B, member 2
SDS-PAGE	sodium dodecyl sulfate polyacrylamide

	gel electrophoresis
SEBV	sebokele virus
SEC	size-exclusion chromatography
Sf9	spodoptera frugiperda 9 cell
SVV	seneca valley virus
TCID50	50% tissue culture infective dose
TFZ	translation functional Z-score
TIM-1	T-cell immunoglobulin and mucin domain 1
TMB	trimethylbenzene
TMEV	theilers virus
TrV	triatomavirus
USP	universal stress protein
UTR	untranslated region
VLP	viral like particles
VP	viral protein

Acknowledgements

I am indebted for the tremendous guidance, support and help from my supervisors David Stuart, Elizabeth Fry, Toby Tuthill and Nick Knowles, and for giving me the chance to study in Strubi. Also, I would like to thank the staff members in Strubi, especially Jingshan Ren for help with the data collection and for help solving difficulties during structure determination, Margaret Jones for help in the wetlab, Weixian Lu for help with tissue culture, Yuguang Zhao for help with protein purification and Tom Walter for help with protein crystallization. Thanks to Hannah Wenham and Teruo Yamashita for providing the virus materials. I want to thank Anastassis Perrakis, Zihe Rao and Xiangxi Wang for the collaborations and the support.

I feel extremely grateful to the divison, the department and Pirbright Institute for providing me with the funding.

I am very thankful for those people who supported me during my D.Phil, especially my lab mates for their help and for sharing their experience during their pursuit of science. Last but not least, I want to thank my family for giving me my life and all the love.

Declaration of work

All the described work herein is my own, except that detailed immediately below:

Chapter 3 (Ljungan virus)

This chapter is based (including figures) on an article published in Nature communications which was prepared by David Stuart and myself (Zhu *et al*. 2015). The orginal virus stock was kindly provided by Toby Tuthill; Claudine Porta provided assistance with virus cultivation; Abhay Kotecha helped with grids preparation and set up the polara microscope for data collection. Xiangxi Wang and I were both involved in cryo-EM data collection and structure reconstruction. Jingshan Ren gave valuable help in model building. Elizabeth Fry and David Stuart supervised me in structural analysis and the thesis writing.

Chapter 4 (Aichi virus)

This chapter is based (including some figures) on an article published in Nature Microbiology which was prepared by David Stuart and myself (Zhu et al. 2016). The orginal virus stock was a gift from Teruo Yamashita; Abhay Kotecha provided assistance with grids preparation and microscope set up. Xiangxi Wang supervised

me in cryo-EM data collection, data processing and structure reconstruction. Jingshan Ren and Xiangxi Wang helped me with model building and structural analysis. Elizabeth Fry and David Stuart oversaw thesis writing.

Chapter 5 (CVA VLPs)

This chapter is based (including some figures) on an article published in Journal of Virology which was prepared by David Stuart, Jingshan Ren and myself (Ren *et al*. 2015). Xiangxi Wang helped collect the diffraction data of CVA16 VLP at the Spring 8 synchrotron; Jiangshan Ren assisted me to refine and validate the atomic model. The production of neutralizing mAbs (D6, A9, C33) and neutralizing titers evaluation were done by Sinovac Company.

Chapter 6 (HAV and R10 Fab)

This chapter is based (including some figures) on an article published in PNAS which was prepared by David Stuart, Xiangxi Wang and myself (Wang *et al*. 2017). The neutralizing mAb against HAV, namely R10, was produced by Sinovac Company and neutralizing titers were measured by Xiangxi Wang. Jingshan Ren provided help with crystal mounting and diffraction data collection for Fab R10. Tom Walter helped to prepare grids and set up the microscope. Xiangxi Wang and I collected the cryo-EM data, determined the complex structure of HAV and Fab R10. RT-PCR assay was done by Xiangxi Wang.

Chapter 7 (2As)

Jingshan Ren was involved in cryo-cooling of numerous crystals and data collection, he also helped solving difficulties I came across during structure determination. Xiangxi Wang assisted me to design and explore the potential phospholipase activity. Prof. Anastassis Perrakis kindly provided the coordinates served as a search model to solve our structure of LV 2A. David Staunton gave valuable help for circular dichroism spectra analysis.

Publications:

(1) **Zhu Ling#**, Wang Xiangxi#, Ren Jingshan, Porta Claudine, Wenham Hannah, Ekstrom Jens-Ola, Panjwani Anusha, Knowles Nick J, Kotecha Abhay, Siebert C Alistair, Lindberg A Michael, Fry Elizabeth E, Rao Zihe, Tuthill Tobias J, Stuart David I. **Structure of Ljungan virus provides insight into genome packaging of this picornavirus**.，Nat Commun，2015.10.8，6：8316~8316

(2) **Zhu Ling#**，Wang Xiangxi#，Ren Jingshan，Kotecha Abhay，Walter Thomas S，Yuan Shuai，Yamashita Teruo，Tuthill Tobias J，Fry Elizabeth E，Rao Zihe，Stuart David I. **Structure of human Aichi virus and implications for receptor binding.**，Nat Microbiol，2016.9.5，1（11）：16150~16150

(3)Wang Xiangxi#，**Zhu Ling#**，Dang Minghao#，Hu Zhongyu，Gao Qiang，Yuan Shuai，Sun Yao，Zhang Bo，Ren Jingshan，Kotecha Abhay，Walter Thomas S，Wang Junzhi，Fry Elizabeth E，Stuart David，Rao Zihe . **Potent neutralization of hepatitis A virus reveals a receptor mimic mechanism and the receptor recognition site**.，Proc Natl Acad Sci U S A，2017.1.24，114（4）：770~775

(4) Ren Jingshan#，Wang Xiangxi#，**Zhu Ling#**，Hu Zhongyu，Gao Qiang，Yang Pan，Li Xuemei，Wang Junzhi，Shen Xinliang，Fry Elizabeth E，Rao Zihe，Stuart David I，**Structures of Coxsackievirus A16 Capsids with Native Antigenicity. Implications for Particle Expansion, Receptor Binding, and Immunogenicity**.，J Virol，2015.10.01，89（20）：10500~10511

# These authors contributed equally to this work.

Chapter 1
Introduction

1.1 Introduction to picornaviruses

Picornaviruses belong to the family *Picornaviridae* which consists of at least 33 genera, responsible for a range of important animal and human diseases including poliovirus (PV), human rhinovirus (HRV), enterovirus 71 (EV71), hepatitis A virus (HAV), and foot and mouth disease virus (FMDV) [1]. The term *Picornaviridae* is derived from *pico*, which means small (typically, 25-30 nm), and RNA, referring to the single-stranded positive-sense RNA common to all members of the *Picornaviridae* family [2]. Usually, picornaviruses are naked, without lipid envelopes, with RNA genomes ranging from 7.2-8.5 kb in size. They comprise one of the simplest architectures for a non-enveloped RNA virus, with a single-stranded, positive-sense RNA genome surrounded by an icosahedral capsid assembled from 60 copies of each of the structural proteins, VP4, VP2 (or uncleaved VP0), VP3 and VP1 [3]. Thus picornaviruses are model systems for how non-enveloped viruses use a protein machine to transfer their fragile genomes across a membrane into the host cell. Morphogenesis is the least-understood step in the life cycle of viruses, including picornaviruses, and this process has proved hard to study, because encapsidation is tightly related with genome structure condesing [4]. Although the structures of a number of picornaviruses have been extensively studied, mechanisms for uncoating, assembly and interaction with cellular receptor(s) are still poorly understood.

1.1.1 Biological characteristics and classification of picornaviruses

The *Picornaviridae* is a large family of RNA viruses and currently consists of 54 species grouped into 33 genera distinguished by a range of biological, biophysical, and genetic characteristics [5]. Picornaviruses have single-stranded positive sense RNA genomes of approximately 7,000–8,500 nucleotides with similar but not identical organizations across the family [6] (Fig. 1.1). The 5' end of the genome is linked to a small peptide (VPg), and the 3' end terminates with a poly(A) tract [7]. The RNA genome encodes a single polyprotein, which is processed into mature proteins by viral proteases. The picornavirus capsid comprises 60 identical subunits (protomers) and each protomer in the majority of picornavirus capsids contains a copy of the four structural viral proteins (VP1–VP4), of which VP1, VP2, and VP3 are external, whereas VP4 is completely internal and therefore not usually exposed to the host antibody response. In some cases, the final, assumed RNA-catalysed, maturation cleavage of the capsid protein precursor VP0 to VP2 and VP4 does not take place [8]. Proteins VP1–VP3 each adopt a β-barrel configuration and are arranged with icosahedral symmetry such that VP1 surrounds the five-fold axes, and VP2 and VP3 alternate about the two- and three-fold axes [9]. Typically the lengths, compositions and configurations of the connecting loops have effects on the surface topology of the virus particle and are mainly responsible for receptor binding specificities and antigenic characteristics. In some picornaviruses, canyon-like

depressions (named “canyon”) encircling the five-fold axes on capsids are found, which are frequently the sites of receptor attachment [10]. Picornaviruses can also produce empty particles, which resemble the mature virus in structure and antigenicity in some cases, sediment at ~80S and comprise 60 copies of VP0, VP1 and VP3 [11].

All the structural proteins are encoded by the P1 region of the genome and the P2 and P3 regions encode seven non-structural proteins from 2A–2C to 3A–3D, including the proteases, the putative helicase, and the RNA-dependent RNA polymerase. In some picornaviruses, two or three 2A proteins (unknown functions) may be produced, whilst in others, two or three paralogous copies of 3B (also known as VPg) are generated [12]. In enteroviruses, the 2A functions as a protease to cleave the site between the C-terminus of capsid protein VP1 and the N-terminal of the protease itself, and also shuts down the host protein synthesis through cleavage of the host eukaryotic initiation factor 4G (eIF4G) [13]. The 2C in picornaviruses is the most conserved but the least understood protein, which has been predicted to be a putative superfamily 3 (SF3) helicase that supposedly plays a pivotal role in enteroviral RNA replication [14, 15]. The 3C regions of all picornaviruses code for a protease, named $3C^{pro}$, which cleaves the precursor polyprotein to separate or mature the individual proteins [16]. 3D in all picornavirus is an RNA-dependent RNA polymerase (RdRp) which shares sequence and structural similarities with all known

DNA and RNA polymerases [17]. Some picornaviruses, like FMDV, have an additional leader (L) protein before the start of the structural gene region [18, 19].

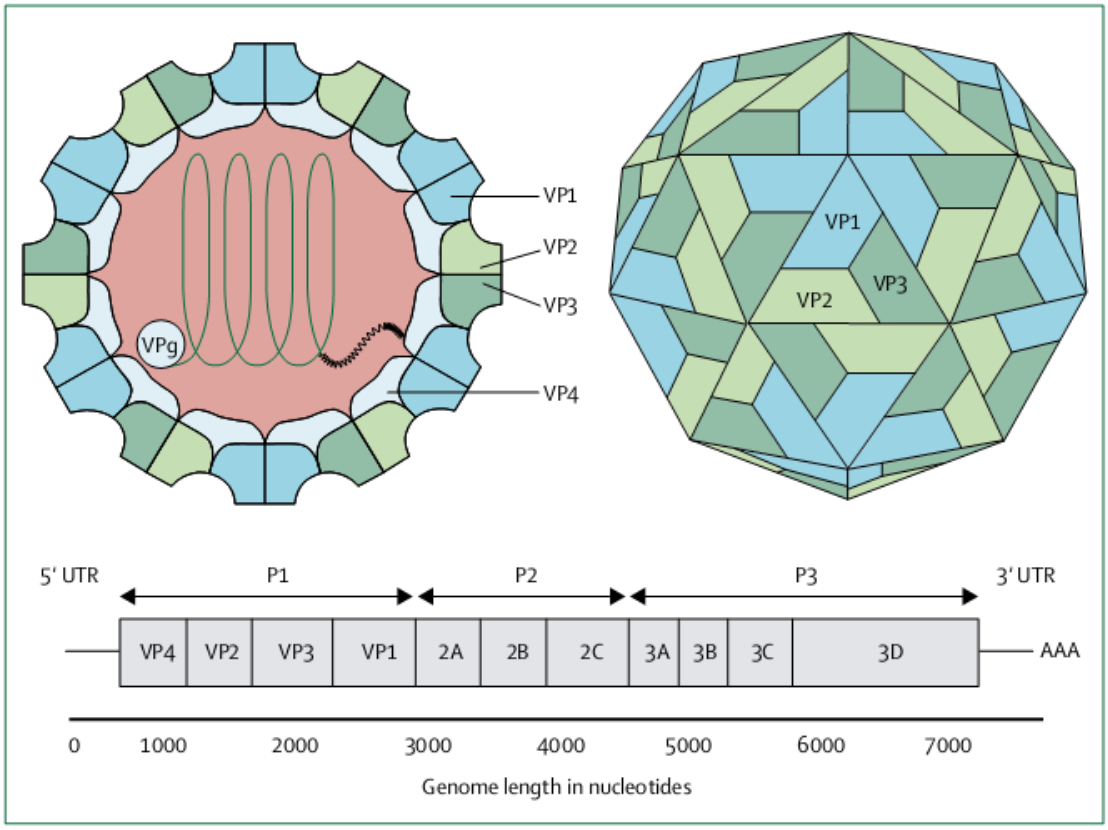

Fig. 1.1 Picornavirus structure, genome and polyprotein organization. UTR=untranslated region. VPg=virus encoded protein. Reprinted from The Lancet, Vol 10, Solomn *et al*. Virology, epidemiology, pathogenesis, and control of enterovirus 71, P 778-790., Copyright (2010) [6], with permission from Elsevier.

Picornaviruses form one of the largest and most divergent virus families. Classifications of picornaviruses were traditionally based on a combination of physical properties and serological relatedness. Recently more and more sequence data have become available, and these are now employed in a systematic framework that has become the standard for establishing viral classifications and species concepts. Evolutionary relationships among picornaviruses assist in uncovering the common features of uncharacterized viruses. A maximum likelihood phylogenetic analysis of 32 picornaviruses based on the amino acid sequences of P1 was conducted (Fig. 1.2), where they could be mainly categorized into three potential groups: Group 1, probably consisting of *Enterovirus* and *Sapelovirus* genera, in most cases, contain VP4 and a pocket factor as well as a 2A protease [20-22]. Group 2, taking FMDV as a representative, have the 2A protease replaced with a leader peptide (L) and contain VP4 but have no pocket factor [23, 24], whilst Group 3, best exemplified by parechovirus, have no VP4 or pocket factor either and the function of 2A is unclear [8, 25].

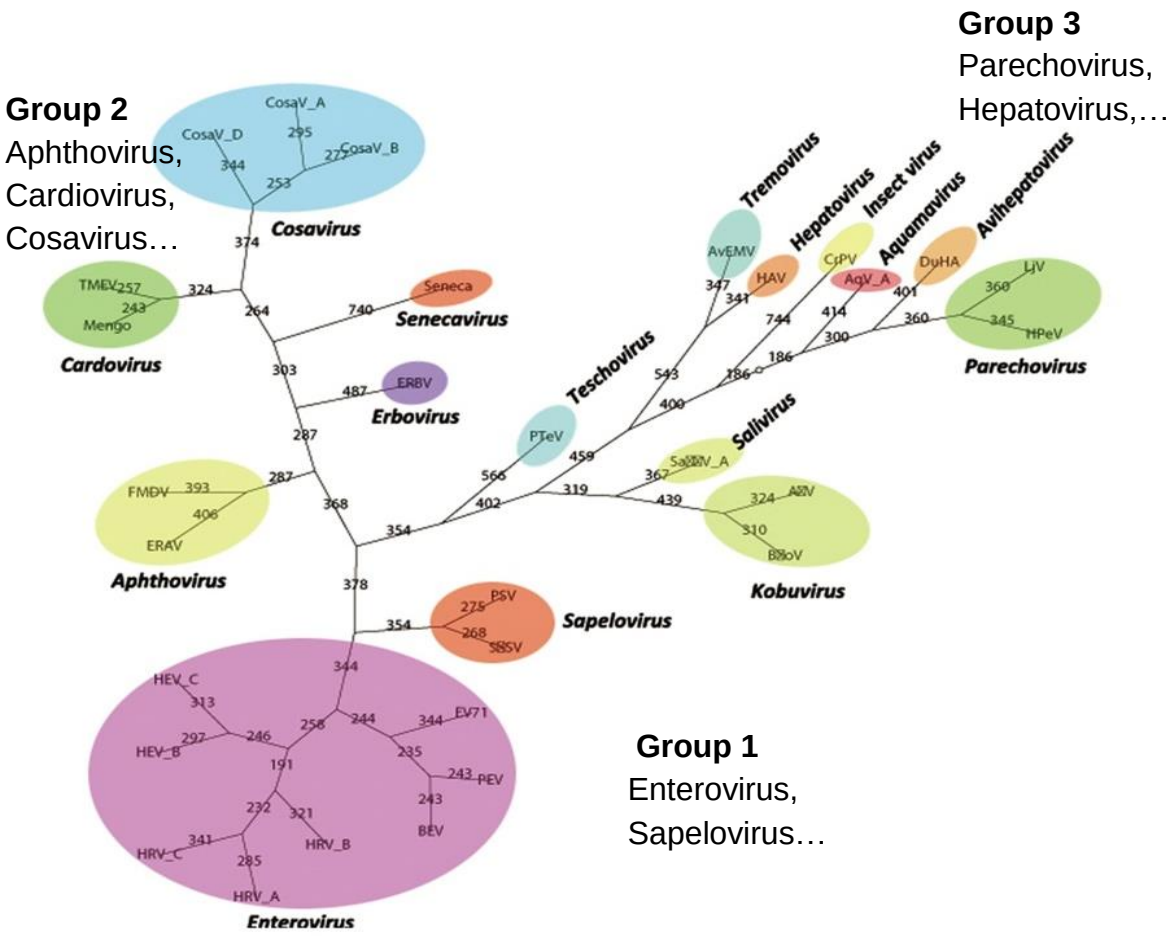

Fig. 1.2 Phylogeny of the *Picornaviridae* family. Shown is the maximum likelihood phylogenic tree of 32 picornaviruses representing species diversity based on the amino acid sequences of P1 using an online server, RAxML [26].

1.1.2 Structures of picornavirus particles

The structures of a number of picornaviruses have been determined at close to atomic resolution by X-ray crystallography and cryo-EM, mainly in Group 1 and Group 2, including PV [9], HRV [27], EV71 [20], FMDV [28] *etc*., and recently Wang X *et al.* [25] reported the first structure of a Group 3 picornavirus (HAV). For many picornaviruses, two predominant types of viral particles are produced during a natural infection, mature virus (containing packaged RNA) and empty procapsids (without RNA), which may be separated using continuous sucrose density gradient ultracentrifugation. However, such natural empty particles have not been observed for either Ljungan virus (LV) or human parechovirus (HPeV) [29]. In the mature virus, VP1–VP3 follow a pseudo T = 3 arrangement, they form a compact and icosahedrally-symmetric particle and span the thickness of the capsid [30]. Interestingly, some empty particles (e.g HAV, CVA16) resemble the mature virus in structure and antigenicity, sediment at ~80S and comprise 60 copies of VP0, VP1 and VP3 [25, 30], whilst some empty particles (e.g EV71) are markedly expanded and resemble enterovirus uncoating intermediates (Fig. 1.3) [20], but in empty particles (e.g EV71) assumed RNA-catalysed, maturation cleavage of the capsid protein precursor VP0 to VP2 and VP4 does not take place. Enteroviruses have a surface feature termed the canyon (a depression encircling the five-fold axes) (Fig. 1.3) [31], which often contains the receptor-binding site [10]. Aphthoviruses present a rather smooth surface [19, 28] (Fig. 1.3), whilst, compared to FMDV, the loops at

the five-fold and three-fold axes in HAV are slightly raised, giving the virus the appearance of a faceted triakis icosahedron [25] (Fig. 1.3). The picornavirus capsids are responsible for cellular receptors recognition, entry into host cells and the release of viral RNA.

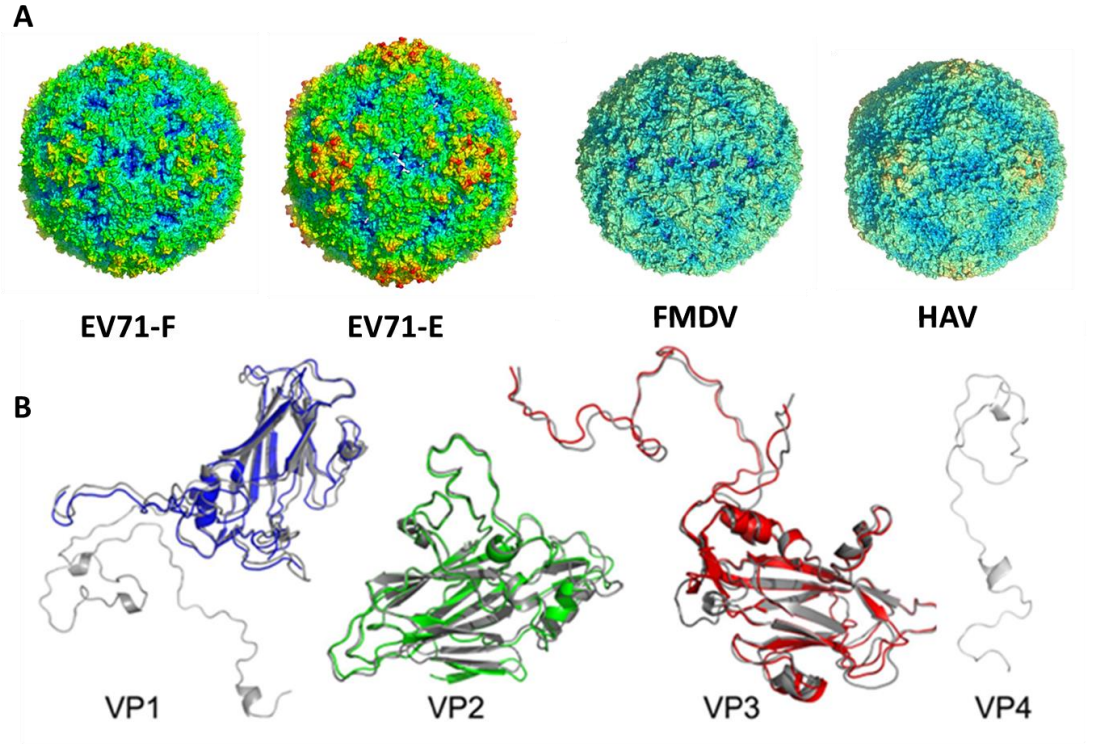

Fig. 1.3 Overall structures of EV71 full and empty particles, FMDV and HAV and structures of the EV71 capsid proteins VP1–VP4. **(A)** Radial colored structures for EV71-F, EV71-E, FMDV and HAV were generated from the

coordinates with PDB codes of 3VBH [20], 3VBO [20], 1FOD [32] and 4QPI [25] respectively. Cartoon structures were generated from the coordinates with PDB codes of 3VBH [20] and 3VBO [20] respectively. **(B)** Proteins from EV71 empty particle are colored, whereas the corresponding chains from EV71 full particle are gray. Reproduced from [20, 25].

1.1.3 Picornavirus receptors

Receptors play a fundamental role in the entry of most viruses. In the case of picornaviruses, they are involved in cell attachment, endocytosis and viral RNA genome release [7]. Although most picornaviruses share similar overall structures, they utilize a wide variety of cellular receptors for entry into host cells. Receptors used by different picornaviruses belong to the immunoglobulin superfamily [33], the low density lipoprotein receptor (LDLR) superfamily [34] and the integrin superfamily [33, 35]. However, two receptors for EV71: human P-selectin glycoprotein ligand-1 (PSGL-1) [36] and scavenger receptor class B member 2 (SCARB2) [37] are significantly different from existing picornaviruses receptors (Fig. 1.4). Some receptors only play a role in the attachment of viruses to host cells, but some are functional receptors (not only mediating viral attachment, but also assisting in viral uncoating). The integrin (αVβ6), the low density lipoprotein receptor (LDL-R), decay-accelerating factor (DAF) and T cell immunoglobulin mucin domain 1 (TIM1) serve as cellular receptors for FMDV, the minor-group

HRVs, several types of echoviruses and HAV respectively [35, 38, 39]. Recently it was determined that human rhinovirus C utilizes CDHR3 to enter host cells [40]. These receptors facilitate viral attachment and internalization, but not uncoating [7, 41], while CD155, intercellular adhesion molecule 1 (ICAM-1), coxsackievirus and adenovirus receptor (CAR), and SCARB2 are functional receptors for PV, the major-group HRVs, CVB and EV71 respectively [33, 37, 42, 43]. The canyon structure on the enterovirus surface (Fig. 1.3) is widely used as the site for capsid binding to cellular receptors [44-46], but the five-fold vertices are also exploited by picornaviruses to bind to cellular receptors [10]. In addition, a number of picornaviruses bear an ‘arginine-glycine-aspartic acid (RGD) motif’ on the capsid surface, where integrin receptor can attach [35, 47]. A number of picornaviruses have been demonstrated to require multiple receptors or co-receptors to alter the capsid structural conformation for productive infection, in particular some DAF-binding enteroviruses. For example, CVA21 utilizes ICAM-1 as a co-receptor, which binds into the “canyon” and can trigger capsid alterations to uncoat [48]. Some receptors such as PSGL-1 and DAF, just play a role in the attachment of viruses to host cells, but do not trigger viral uncoating, and therefore functional receptors are needed to mediate viral genome release [49].

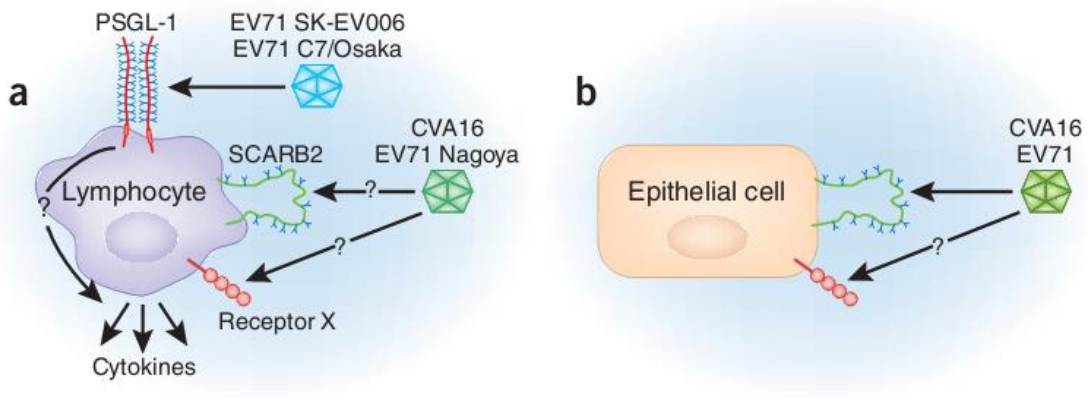

Fig. 1.4 Receptors for EV71 and CVA16. Reprinted by permission from Macmillan Publishers Ltd: Nature Medicine [50]. Copyright (2009). https://www.nature.com/nm/.

1.2 Picornavirus uncoating and assembly

1.2.1 Uncoating mode

Picornaviruses utilize a variety of receptors to facilitate binding to cell surfaces and entry of host cells through endocytosis with progressive acidification of the endosome [10]. 3 main endocytic pathways have been identified: 1) clathrin-mediated endocytosis-- some picornaviruses enter via clathrin-coated pits that are internalized to form clathrin-coated vesicles, which are then delivered to the early endosome and subsequently the late endosome; 2) caveolin-mediated

endocytosis-- some picornaviruses enter cells via caveolin-mediated endocytosis which is dependent on the presence of lipid rafts and cholesterol and are sorted into the caveosome; 3) neither clathrin- nor caveolin- mediated endocytosis [7, 51, 52]. Viral uncoating, the key step in releasing the RNA genome into the host cell cytoplasm for a productive infection, occurs in the endosome [53, 54]. To date, several modes of uncoating for picornaviruses have been clarified. PV, CVB and the major-group HRVs undergo conformational changes to release RNA (Fig. 1.5), which are induced by their uncoating receptors at neutral conditions [55, 56]. The conformationally modified intermediate particle is termed an A particle. Another pattern is the conformational alteration of the minor-group HRVs, which is dependent on an acidic pH (Fig. 1.5) [57]. For FMDV/ERAV, the virion dissociates into pentamers directly for RNA release under acidic conditions (Fig. 1.5), without the aid of its receptor [58], while EV71 uncoating requires both functional receptor (SCARB2) and low pH to convert to an A particle, followed by the release of its viral RNA genome (Fig. 1.5) [44]. However, HAV, kobuviruses and parechoviruses probably uncoat via novel mechanisms yet to be identified, and are assembled differently to the other picornaviruses discussed.

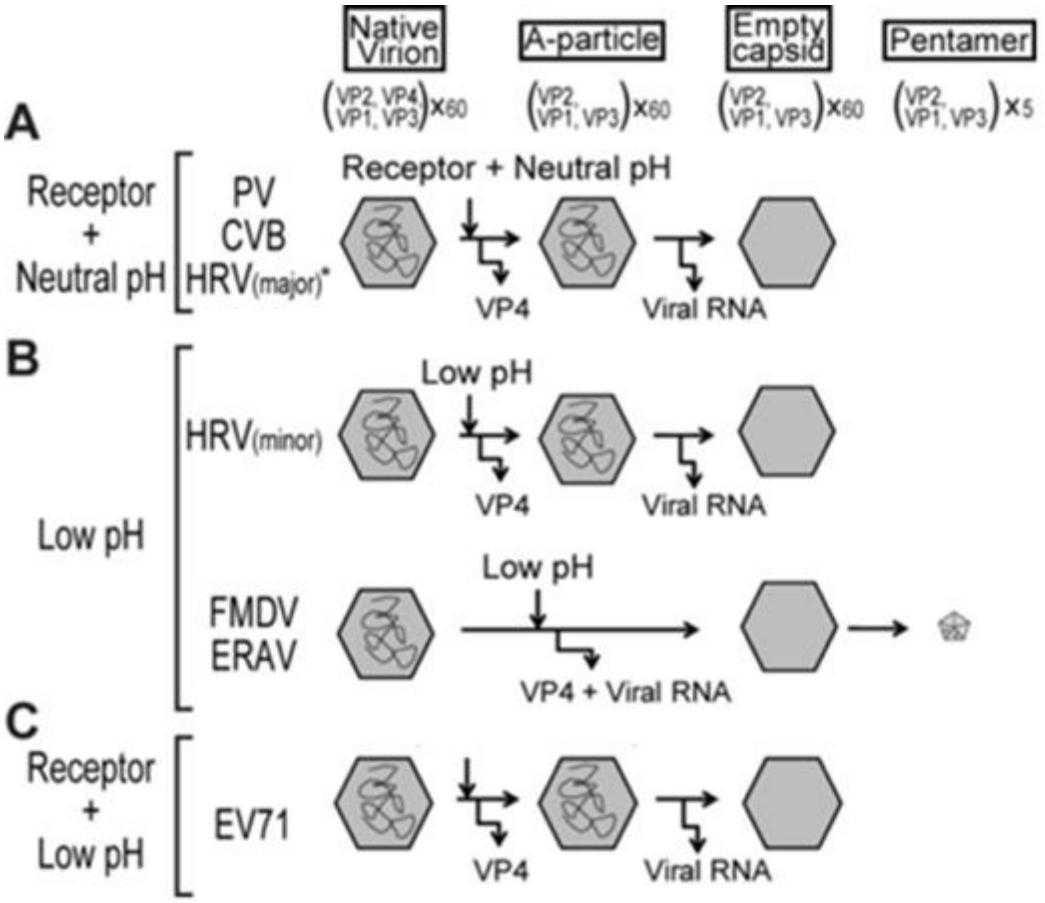

Fig. 1.5 Schematic diagram of picornavirus uncoating modes [49]. Reprinted from Seiya *et al.* Copyright (2013) Journal of Virology.

1.2.2 Uncoating intermediate particle

Although the trigger for genome release differs for different picornaviruses, from a structural point of view, the virus (capsid) must undergo dramatic conformational changes to open "holes" or to dissociate into pentamers to release the viral genome into the host cell cytosol. In depth studies into the process of genome release in

picornaviruses are relatively few, and are mainly in enteroviruses. Recent studies report that mature enteroviruses can ‘breathe’, leading transiently to the partial externalization of internal capsid proteins (the structures of enteroviruses are dynamic in their life cyle and the internal polypeptides VP4 and N terminus of VP1 (residues 1 to 53) externalize reversibly), and high resolution structural studies have visualized expanded capsids thought to correspond to viral uncoating intermediate particles [59-62]. For enteroviruses, the mature virus (160 S) contains 60 copies of a hydrophobic ‘pocket factor’ (a natural lipid) buried in a pocket lying at the base of the canyon in the capsid protein VP1 [7]. Receptor binding at the canyon site dislodges a pocket factor from the hydrophobic pocket leading to a cascade of structural changes, ultimately resulting in the release of the N terminus of VP1 and VP4 to form the expanded 135 S uncoating intermediate particle or A-particle [20, 63]. The high resolution structure of a CVA16 uncoating intermediate suggests a detailed hypothesis for the ordered egress of the internal proteins, using two distinct sets of channels through the capsid and suggests that the viral RNA genome might exit near the two-fold axes (Fig. 1.6) [21]. Since the expulsion of the pocket factor is required for infection, a tight replacement binder (compound) could be rationally designed to act as a useful antiviral drug candidate. Pleconaril and BTA798 (capsid binder compounds) are two cases of structure-based drug design against HRV infection, which have completed phase II clinical trials [64, 65]. On the basis of

EV71 structural information, a number of novel inhibitors were designed, synthesized and demonstrated to exhibit extreamly antiviral activities against EV71 infection, among of these, NLD (with IC50 of 25 pM) is an order of magnitude more potent than the best previously reported inhibitor [66].

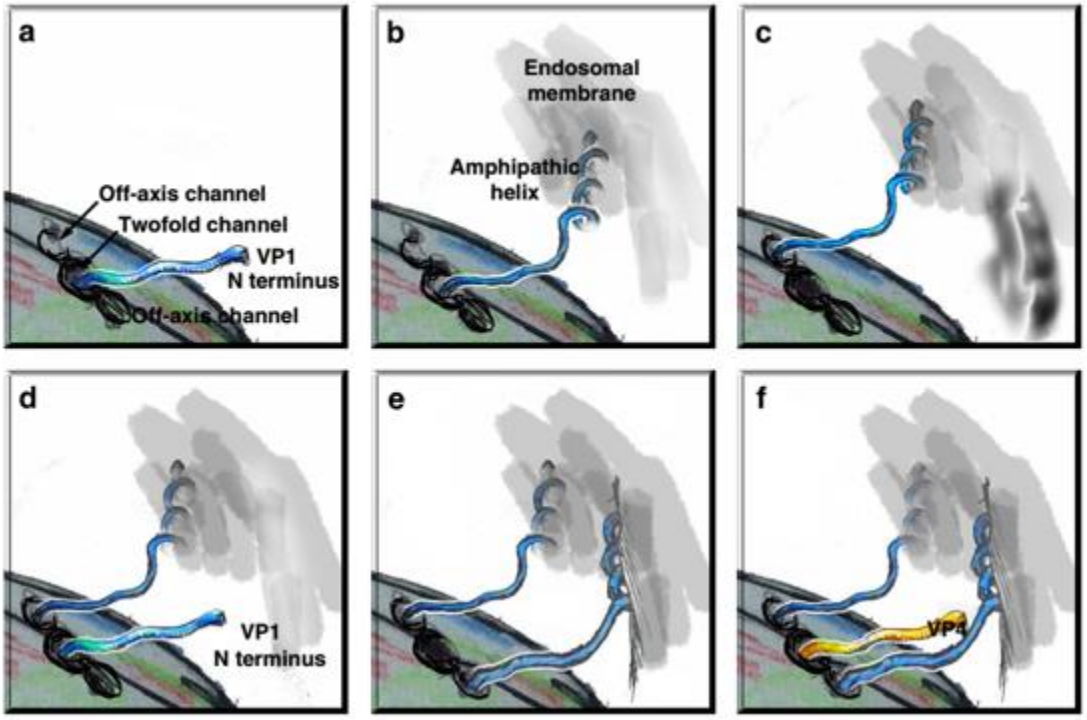

Fig. 1.6 Cartoon of the early stages of enterovirus cell entry [21]. Reprinted from Ren *et al.* Copyright (2013) Nature Communications.

1.2.3 Viral particle assembly

Encapsidation of the viral genome leading to the assembly of infectious progeny virions is an essential step in the virus life cycle. The two most commonly employed

strategies for packing viral genomes are (i) filling a preformed procapsid with progeny genome, termed sequential assembly (e.g. most bacteriophages and herpesviruses) and (ii) the nucleation of capsid assembly around viral nucleic acids, termed concerted assembly [67, 68]. Although we know clearly how bacteriophages package the viral genome into a preassembled procapsid using packaging motor proteins [69] and how plant viruses govern RNA packaging through protein-protein or protein-RNA interactions [70], picornavirus assembly remains unclear. The selective encapsidation of the viral genome, and not cellular RNA, requires the specific recognition of sequences or structures unique to viral nucleic acid or packaging signals, but attempts to identify packaging signals in picornavirus genomes have failed [29], except for in Aichi virus which contains a 5'–terminal RNA stem loop critical for viral RNA encapsidation [71]. A recent study demonstrated that the interactions between capsid proteins and the RNA replication complex facilitate PV encapsidation [72]. It is widely accepted that the capsid proteins assemble into pentamers which either, by interaction with viral RNA produce mature virions (genome-filled capsids) [29], or form empty particles [4]. However, it is still debatable whether the natural empty particles are on-pathway intermediates for RNA encapsidation or dead-end products [59].

1.3 Picornavirus viral like particles (VLPs) and potential vaccine development

1.3.1 Picornavirus VLPs production

VLPs are empty particles consisting of viral capsid proteins but devoid of viral genome, so they are non-infectious. It has been demonstrated that VLPs are generally able to induce broad and strong immune responses similar to inactivated viruses [73, 74], therefore VLPs have attracted more and more attention as potential vaccine candidates [75].

A few recombinant VLPs including PV, EV71, CVA16 and FMDV *et al*. have been produced using the baculovirus/insect cell, mammalian/vaccinia or yeast expression systems [30, 58]. However, the strategies for these VLP productions are similar, relying on co-expression of the P1 and 3CD proteins (Fig. 1.7), or separate expression of the P1 and 3C proteins, or co-expression of the individual VP0, VP1 and VP3 proteins [76]. A couple of approaches to improve the production of VLPs have been reported, including utilizing a secretion expression system, replacement of the promoter under the open reading frame of 3CD or 3C [77], and expression in plants [78]. In the former case, Shih-Yeh Lin *et al.* [79] found a recombinant baculovirus constructed using the flashback GOLDTM system to express P1 under the polh promoter and 3CD under the CMV promoter, dramatically improved the VLP yield such that the total and extracellular VLP yields were 268 and 171 mg/L

respectively. Excitingly, CVA16 VLPs are capable of potently eliciting neutralizing antibodies that protect mice against lethal challenge and considered as a promising vaccine candidate [80].

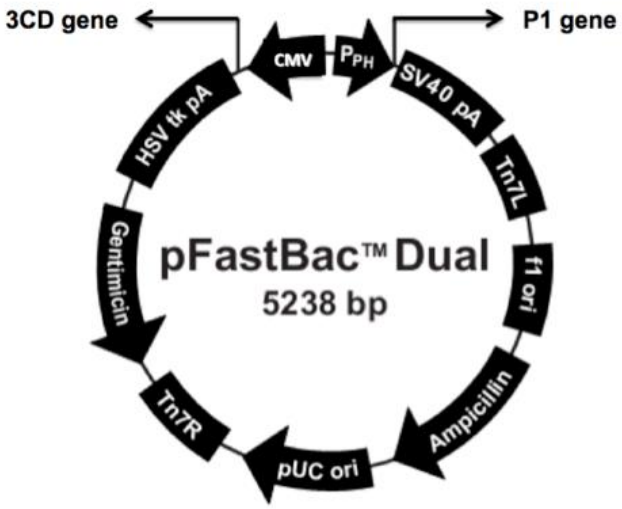

Fig. 1.7 Strategy for expression of picornavirus VLPs

1.3.2 Picornavirus vaccine development

A vaccine is a biological preparation that confers immunity to a particular disease and vaccination has greatly reduced the burden of infectious diseases. There are several types of vaccines: inactivated or attenuated disease-causing microorganisms or purified products derived from them including VLPs and DNA vaccines (where the cells produce the antigen and then produce a protective reponse to it) [81]. The first picornavirus vaccine was inactivated poliovirus vaccine (IPV) that was licensed in 1955 and was used extensively; in 1961, type 1 and 2 monovalent oral poliovirus vaccine (MOPV) was licensed [82]. Until 1991, the whole of continental Europe (except Denmark) routinely vaccinated against FMDV, however, at that time, one could not differentiate between animals being sero-positive due to vaccination, or, due to having previously been infected with virus. FMDV vaccination is currently reliant on the use of inactivated virus produced in large bioreactors in high containment facilities, which is unsatisfactory and also highlights the requirement of more options for FMDV vaccine production [83]. In 2013, Porta *et al.* developed novel methods to efficiently express recombinant FMDV empty capsids with enhanced capsid stability by incorporating a rationally designed mutation, which shows several potential advantages over current technologies by reducing production costs, eliminating the risk of infectivity and enhancing the temperature stability of the product [83]. Excitingly, Sinovac Biotech Ltd, a leading provider of

biopharmaceutical products in China, announced that the China Food and Drug Administration (CFDA) issued a new drug certificate and production license for its Enterovirus 71 (EV71) vaccine in 2016. The randomized, double-blind, placebo-controlled phase III trial enrolling over 10,000 healthy children aged 6-35 months who were randomly assigned to receive placebo or inactivated EV71 vaccine at day 0 and 28 in China showed 100% efficacy against EV71-associated hospitalization, 90.0% efficacy against EV71-associated HFMD and 80.4% against EV71-associated disease[84, 85]. Although there has been progress with vaccines for EV71, the development of a CVA16 (another major causative agent for HFMD) vaccine has proved more challenging and the EV71 vaccine does not give useful cross-protection, despite the capsid proteins of the two viruses sharing about 80% sequence identity. A CVA16 vaccine or bivalent EV71/CVA16 vaccine is therefore urgently needed. Structural and immunogenic studies of CVA16 and CVA16 VLPs in this thesis aim to facilitate structure-based drug design and vaccine development.

1.4 Aims

The main aim of the work presented in this thesis is to understand the mechanism(s) underpinning picornavirus assembly, uncoating, receptor recognition and VLP production at the structural level and to explore the potential roles of 2A proteins from *Parechovirus* genus based on structural studies. A combination of X-ray

crystallography, advanced cryo-EM, immunological, virological and biophysical techniques has been used in this study. I believe such studies will provide a better understanding of the molecular basis for key points in the life cycles of different picornaviruses, which may be useful in the design of further vaccines and effective drugs.

Chapter 2
Materials and methods

2.1 Molecular biology and virus production

Structural studies of 2A proteins from LV, SEBV and HPeV and recombinant VLPs of CVA16

2.1.1 Cloning

Ljungan virus 87-012 2A2 (NCBI Reference Sequence: NP_705878.1), human parechovirus type 3 2A (GenBank: BAC23086.1，2A aa 772-920) and Sebokele virus 1 2A (NCBI Reference Sequence: YP_008119838.1) were synthesized by the Genescript Company.

Constructs for LV 2A2 and HPeV 2A expression in *E. coli* were cloned in PET28a vector (Novagen) (Fig. 2.1) between the Nco1 and Xho1 restriction sites with a C-terminal His tag. The construct for SEBV 2A expression in *E. coli* was cloned in the pGEX-6P-1 (Novagen) vector (Fig. 2.2) between BamH1 and Xho1 restriction sites with a N-terminal GST fusion tag. Both vectors are commercially available vectors for the high level expression of proteins under the T7 promoter.

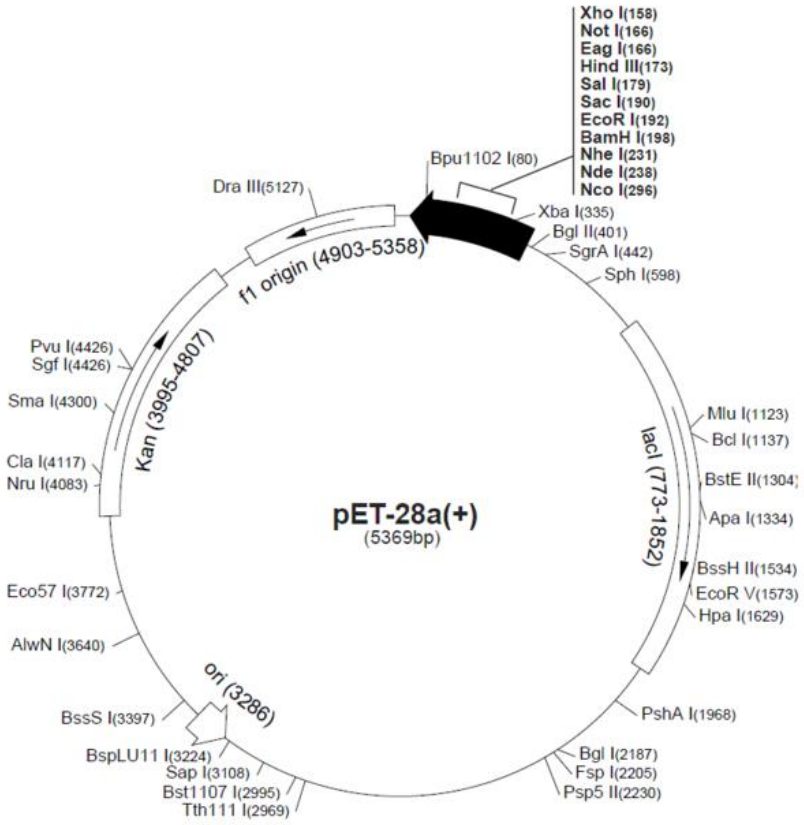

Fig. 2.1 Plasmid map of pET-28a vector

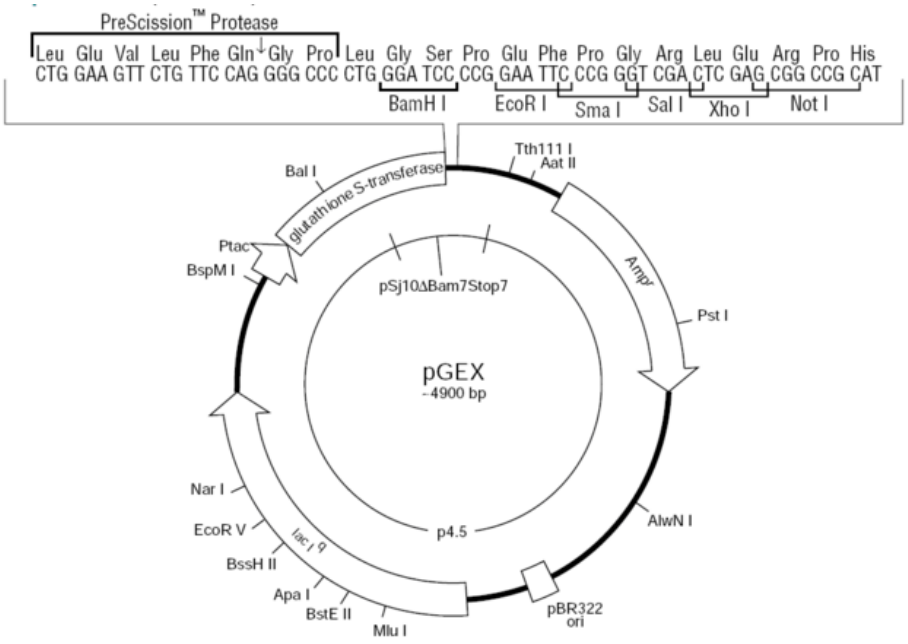

Fig. 2.2 Plasmid map of pGEX-6P-1 vector

All constructs for 2A studies are summarized in Table. 7.1.

For CVA16 VLPs, a modified pFastBac Dual vector (Fig. 1.7) (Invitrogen) containing P1 and 3CD genes under the control of the polyhedrin and CMV promoters respectively was kindly provided by Professor Zhu. Recombinant baculoviruses were generated using a Bac-to-Bac baculovirus expression system (Invitrogen) according to the instructions of the manufacturer.

2.1.2 Protein expression and purification

All recombinant plasmids for 2As were transformed into competent *E. Coli* BL21 (DE3) cells. The bacterial cultures were grown at 37 ℃ to an OD600 of ~0.6, isopropyl β-D-1-thiogalactopyranoside (IPTG) was then added to a final concentration of 0.5 mM and the culture continued at 16 ℃ for 18 h. Cells were harvested and sonicated in the lysis buffer (20 mM Hepes (pH 7.5), 150 mM NaCl). The lysate was centrifuged at 30,700 g to remove cell debris. For LV 2A2 and HPeV 2A, the His-tagged proteins were purified by immobilized metal affinity chromatography. The TALON beads (Clontech) were equilibrated in the lysis buffer containing 5 mM imidazole (Sigma). Imidazole (5 mM) was also added to the supernatant to prevent non-specific binding before the supernatant was pumped through the column. The column was washed with 30 ml lysis buffer containing 10 mM imidazole and 15 ml lysis buffer containing 20 mM imidazole, the target protein was eluted with 20 ml lysis buffer supplemented with 50 mM imidazole. The SEBV

2A was purified by binding to glutathione sepharose 4B (GE) and eluted with the lysis buffer containing 10mM reduced glutathione (GSH), after which PPase (~0.1 mg) was added for the cleavage of the N-terminal GST tag (4 ℃， 6 h). The solution was then loaded onto glutathione sepharose 4B (GE) again, and the flow-through with the SEBV 2A protein was collected. All the proteins were concentrated to 0.5 ml and further loaded onto a Superdex 200 10/300 GL column (GE, the bed dimensions for this column are 10 x 310 mm and the column bed volume is approximately 24 ml) equilibrated with the lysis buffer with a flow rate of 0.5 ml/min. Fractions containing the target proteins were collected, pooled and concentrated for crystallization.

CVA16 VLPs were produced by infecting Sf9 insect cells (2 x 10^6 cells/ml) at a multiplicity of infection (MOI) of 10. The supernatants were collected 3 days after infection, centrifuged to remove cell debris and filtered by 0.22 μm filter (Millipore). Then the supernatants were pelleted through a 30% sucrose cushion ultracentrifugation at 100,000g for 5 h, in an SW28 rotor at 4 ℃. Pellets were resuspended in phosphate-buffered saline (PBS) (pH 7.4), cleared by centrifugation at 10,000 g for 5 min, and loaded onto a 15-45% (w/v) sucrose density gradient (prepared with Biocomp's Gradient Master to form linear gradients using a patented process namely tilted tube rotation) and centrifuged at 103,614 g for 3.5 h, in an SW41 rotor at 4 ℃. Fractions containing VLPs were collected by pipetting, dialyzed

against PBS (pH 7.4) and concentrated for crystallization.

2.1.3 Virus propagation and purification

LV production and purification

An infectious cDNA clone, pLV87-012G, containing the full genome sequence of 87-012G was provided by Prof. Toby Tuthill (Pirbright Institute). The constructed cDNA clone was linearized using the NotI site encoded downstream of the poly-A tail and transcripted *in vitro* using a MEGAscript T7 Transcription Kit (Ambion). RNA was transfected into vero cells of approximately 90% confluence using Escort IV (Sigma). Cytopathic effect (CPE) was observed at a very low rate, so continual passage in vero cells was performed. An increased CPE was observed over five passages following which the cell lysates were used to infect GMK cells.

LV was grown in 500 ml of GMK cells at a multiplicity of infection (MOI) of 2 and the cells were cultured in Dulbecco's modified Eagle's medium (DMEM; Sigma) supplemented with 1% fetal bovine serum (FBS) (Gibco) until 90% of cells exhibited CPE. Both cells and virus containing supernatant were collected, frozen and thawed three times and then centrifuged to remove cell debris. The supernatants were centrifuged for 3 h at 95,000 g and the viral pellet was suspended in PBS buffer + 0.01% Triton X-100, then loaded onto a 15–45% (w/v) sucrose density gradient and centrifuged at 222,000 g for 1.5 h in an SW41 rotor at 4 ℃.

AiV production and purification

The AiV stock (strain A846/88, GenBank: BAA31356.1) was a kind gift from Dr. Teruo Yamashita in Aichi Prefectural Institute of Public Health, Japan. The virus was amplified using 40 x 175 cm^2 flasks of vero cells inoculated at a multiplicity of infection (MOI) of 1. Vero cells were cultured in Dulbecco's modified Eagle's medium (DMEM; Sigma-Aldrich) supplemented with 1% fetal bovine serum (FBS; Gibco) and grown at 37℃ in a humidified atmosphere containing 5% CO2. After 90% of cells showed CPE, the flasks were frozen and thawed three times and the cultures centrifuged to remove cell debris. The supernatants were centrifuged for 3 h at 95,000 g and virus pellets were resuspended in PBST buffer (phosphate-buffered saline containing 0.01% Triton X-100), then loaded onto 15-45% (w/v) sucrose density gradients and centrifuged at 222,000 g for 4 h in a SW41 rotor at 4 ℃. The lower band was pooled and subjected to 35-55% (w/w) discontinuous sucrose gradient centrifugation at 28,000 rpm for 20 h.

HAV production and purification

HAV virus genotype TZ84 was propagated in 2BS cells at a multiplicity of infection (MOI) of 0.2 at 33-34 ℃. Cells were collected 28 days post infection, lysed by treatment with 1% sodium deoxycholate in PBS buffer (pH 7.2), inactivated by incubation with formaldehyde (1:2000 dilution) at 4 ℃ for 7 days and centrifuged to remove cell debris. The supernatant was ultra-filtered using a 0.22 μm filter,

concentrated with a 100 kD cutoff concentrator, precipitated using polyethylene glycol 6000 and then subjected to gel filtration. Production of HAV was done by Dr. Wang from Institute of Biophysics, Chinese Academy of Sciences. Crude HAV concentrate (~0.6 mg in PBS buffer pH 7.4) was loaded onto a 15-45% (W/V) sucrose density gradient and centrifuged at 29,000 rpm for 4 h in an SW41 rotor at 4 ℃. Two sets of fractions were collected and dialyzed against PBS buffer, one comprised empty particles (containing no RNA) and the other virions.

2.2 Antibodies

2.2.1 Production of monoclonal antibodies

One group of 10 adult (4 weeks old) female BALB/c mice (purchased from the Beijing Laboratory Animal Research Center) were immunized intraperitoneally with 10 μg of inactivated HAV viruses or EV71 or CVA16 viruses (containing both empty and full particles), followed by two booster doses at 2-week intervals. Two weeks after the last immunization, blood samples were obtained from the tail and tested by enzyme-linked immunosorbent assay (ELISA) using purified HAV virus or EV71 or CVA16 viruses as antigens. Monoclonal antibodies were produced using conventional protocols (continuous cultures of fused cells secreting an antibody of predefined specificity). These antibodies were produced by the Sinovac Company (China).

2.2.2 Preparation of Fab fragments

Anti-HAV monoclonal antibody (mAb) R10 was produced from the specific hybridomas, from which RNAs were extracted, reverse-transcribed into cDNA, amplified by PCR and sequenced. The amino acid sequence of the R10 light chain V region is:

DIVLTQSPAIMSASPGEKVTMTCSASSSVSYIHWYQQKSGTSPKRWIYDTSRL AFGVPGRFSGSGSGTSYSLTISSMEAEDAATYYCQQWSSNYTFGGGTN.

The amino acid sequence of the R10 heavy chain V region is:

EVKLVESGGGSVKPGGSLKLSCAASGFSFSTYGMSWVRQTPEKRLEWVATIS GGGGYTYYPDSVKGRFTISRDNARNILYLQMSSLRSGDTAMYYCARRVTTV AEYYFDYWGQGTTLTVSSPKTTPP.

R10 was purified by protein A affinity chromatography from mice ascites. Fab fragments were prepared using a Pierce Fab preparation kit (Thermo Scientific) according to the manufacturer's instruction, dialyzed against 20 mM acetate (pH 5.0) at 4 ℃, loaded onto a Mono S column (GE Healthcare) and eluted using a 0–500 mM NaCl gradient. The main peak was collected and dialyzed into PBS buffer overnight using Slide-A-Lyzer™ dialysis cassettes (Thermo Fisher Scientific, molecular weight cutoff of 7 kDa). The antibody and the Fab concentrations were determined by absorbance at 280 nm, and the purity confirmed through SDS–PAGE

analysis.

2.2.3 Neutralizing assay

Purified monoclonal antibodies at a concentration of 0.2 mg/ml were initially diluted 8-fold as stocks, and were then serially diluted 2-fold with DMEM containing 2% FBS. 100 μl of two-fold antibody dilutions were mixed with 100 μl of EV71 or CVA16 virus containing 100 TCID50 for 1 h at 37 ℃, and then the mixture was added to monolayers of vero cells in a six-well plate, meanwhile, maintaining medium was provided as well. Each dilution was replicated 3 times along with one control that contained no serum dilution. Plates were incubated for 5 days at 37 ℃ and then stained with crystal violet, and the cytopathic effect (CPE) was evaluated by observing the color of cells (blue color means the death of cells). The titer of neutralizing antibodies was read as the highest dilution that gave complete protection.

2.2.4 ELISA (virus-mAb binding assay)

The interaction of the viruses with purified neutralizing mAbs was measured by ELISA. 96-well plates were coated with 100 μl/well of inactivated viruses or VLPs (5 μg/ml in PBS buffer) at 4˚C overnight. The wells were then incubated sequentially with 100 μl/well of PBST (phosphate buffered saline with 0.2% Triton X-100) plus 5% BSA at 37˚C for 1 h, and 100 μl/well of neutralizing mAbs at the indicated dilutions at 37 ℃ for 1 h. Horseradish peroxidase (HRP) conjugated goat anti-mouse IgG

(Abnova) diluted (1:5000) in PBST plus 1% BSA was used as secondary antibody at 37 ℃ for 1 h. Five washes with PBST were carried out between incubation steps. For color development, 100 μl/well of TMB mixture was added and incubated for 10 min, followed by addition of 50 μl/well of 1M H_3PO_4 to stop the reaction. Absorbance was measured at 450 nm in a 96-well plate reader (iEMS 96 well Microplate Reader).

2.3 Protein crystallization and crystal structure determination

2.3.1 Crystallization setup

Prior to crystallization, proteins were concentrated (LV 2A2, 75 mg/ml; HPeV 2A, 70 mg/ml; SEBV 2A, 40 mg/ml; R10 Fab, 8 mg/ml; CVA16 VLPs, 3.5 mg/ml). Crystallization trials were set up in Greiner 96-well plates using a Cartesian Technologies robot, adopting 100 nl protein solution plus 100 nl reservoir solution in a sitting-drop vapor-diffusion format [86]. Crystallization screens were supplied by Hampton Research. The plates were maintained at 20 ℃, crystals appeared within 3 weeks. The initial crystallization conditions were usually optimized to improve the quality of the crystals with changes of pH values or precipitant concentrations or protein concentrations or the initial protein: reservoir ratio. All crystals used for data collection grew at 20 ℃ and the crystallization conditions are summarized in Table. 2.1.

Table. 2.1 Crystallizaion conditions and cryoprotectant

Protein	Condition	Conc. (mg/ml)	Cryoprotectant
CVA16 VLP	1.8 M ammonium citrate dibasic, 0.1 M sodium acetate trihydrate (pH 5.0)	3.5	20% glycerol
R10 Fab	20% PEG3350, 0.2 M sodium thiocyanate	8	20% glycerol
LV 2A2	20% PEG3350, 0.2 M sodium formate	75	20% glycerol
HPeV3 2A	1.7 M ammonium sulphate, 0.05 M sodium cacodylate trihydrate pH 6.0	70	20% glycerol
SEBV 2A	30% polyethylene glycol 4000, 0.005 M magnesium acetate, 0.05 M sodium cacodylate pH 6.5	40	20% glycerol

2.3.2 X-ray diffraction data collection

Cryo-cooling was carried out by soaking a crystal in reservoir solution containing 20% (v/v) glycerol prior to flash-cooling with liquid nitrogen and kept at −173 °C during X-ray data collection. All the X-ray diffraction data sets were collected at beamlines at the Diamond Light Source (DLS). Diffraction images (exposure time 0.05-0.2 s with 10-60 % beam transmission) of 0.1 ° rotation were recorded on a PILATUS 6M detector at beamline IO3 (Diamond Light Source), at the following wavelengths: LV 2A2, 1.0000 Å; HPeV 2A, 0.97625 Å; SEBV 2A; 0.97957 Å; R10 Fab, 0.9765 Å; CVA16, 1.0000 Å. More details are listed in Table. 2.2.

Table. 2.2 X-ray diffraction data collection

Protein	Synchrotron	Beamline	Wavelength (Å)	Oscillation(°)	No.of images
CVA16 VLP	Spring 8	BL41	1.0000	0.1	1200
R10 Fab	Diamond Light Source	IO3	0.9765	0.1	1800
LV 2A2	Diamond Light Source	IO3	1.0000	0.1	3600
HPeV 2A	Diamond Light Source	IO3	0.97625	0.1	3600
SEBV 2A	Diamond Light Source	IO3	0.97957	0.1	3600

2.3.3 Data processing (indexing, integration and scaling)

For CVA16 VLP, the X-ray diffraction data were processed, integrated, and scaled using the HKL2000 package [87], the data sets for other projects were processed and analyzed with Xia2 [88], both programs determine the point group symmetry and the unit cell dimensions (unit cell length: a, b, c; unit cell angles:α, β , γ). Data collection statistics, including data completeness, signal-to-noise, error scale factor and Rmerge were used to assess the resolution limit and overall data quality [89].

2.3.4 Molecular replacement

One of the key problems in crystallography is the phase problem, hence the development and use of experimental phasing merthods such as isomorphous replacement and anomalous scattering [89]. Molecular replacement, an alternative approach, is becoming more and more popular [90]. In this case a similar molecule

of known structure is used as a seach model which is usually rotated and then translated and the molecular orientation and position within the unit cell found by maximizing the correlation between the actual data and the model in Patterson space. For each structure, the likely number of molecules in an asymmetric unit was estimated as the number that resulted in a solvent content of 30-70% (corresponding to a Matthews coefficient V_M [91] of 1.8-3.2 $Å^3$/Dalton [92]). The crystal structures of the R10 Fab and 2As were determined by the molecular replacement method [93], with the crystal structures of FMDV Fab (PDB entry: 1QGC [94]) and AiV 2A (coordinates provided by our collaborators, unpublished data) serving as the search model using Phaser [95]. A number of critical parameters, including Z-scores for rotation and translation function, log-likelihood (LLG), the electron density map and number of Ca clashes were used to evaluate the structure solutions. Generally, the correct solution will have a TFZ-score (Translation Function Z-score, the Z-score from the actual translation search, which depends on the accuracy of the orientation used for that search) over 5 and be well separated from the rest of the solutions [95]. The LLG (log likelihood gain) represents the difference between the likelihood of the search model compared to that of a random set of atoms and is related to the overall Z-score. Ideally, a unique solution with a strong signal will be found at the end of the search. If one is searching for multiple components, then ideally the search for each component will also give a strong signal.

2.3.5 Structure refinement and validation

For the R10 Fab and 2As, manual model building and refinement were performed with COOT [96] and PHENIX [97] following rigid body, TLS parameter and individual B-factor refinement. Solvent molecules were located from stereochemically reasonable peaks in the σA-weighted 2Fo-Fc difference electron density map when the resolution was better than 2.8 Å. R factors (R_{work} and R_{free}) were used to evaluate the structure refinement. The final refined models were quality checked using the program PROCHECK [98]. Final refinement statistics are summarized in Tables in the individual chapters.

2.3.6 Illustrations

Sequence alignments were performed with the program CLUSTALW2 [99] and the alignment results were graphically displayed with the program ESPript [100]. Secondary structure elements were indicated according to the structure of each protein, using the default criteria. Structural figures were drawn with the program PyMOL [101] and CHIMERA [102].

2.4 Electron microscopy

2.4.1 Transmission electron microscopy

Transmission electron microscopy (TEM) is one of the most versatile structure determination techniques in biological sciences. TEM is based on a beam of high

energy electrons that are used to illuminate an ultra-thin sample. The sample must be thin since the interaction between electrons and matter is generally much greater than between X-ray and matter). Imaging biological objects in an electron microscope is, in principle, analogous in some respects to light-microscopic imaging (Fig. 2.3) and every TEM is composed of an electron emission source, an electromagnetic lens system, objective and condenser apertures and image detection systems like a charge-coupled device (CCD) camera or direct electron detector (DDD). In TEM, a source housed under a high vacuum emits electrons, and then these electrons are accelerated down the microscope column at voltages of typically 120–300 kV. After passing through the specimen, scattered electrons are focused by the electromagnetic lenses of the microscope [103]. The magnification and focusing of electron beams is controlled by a series of magnetic lenses, comprising condenser, objective and projection lenses. These lenses are imperfect in shape and suffer from aberrations, including spherical aberration. The spherical aberration is constant for a particular microscope and can be corrected during image processing [104].

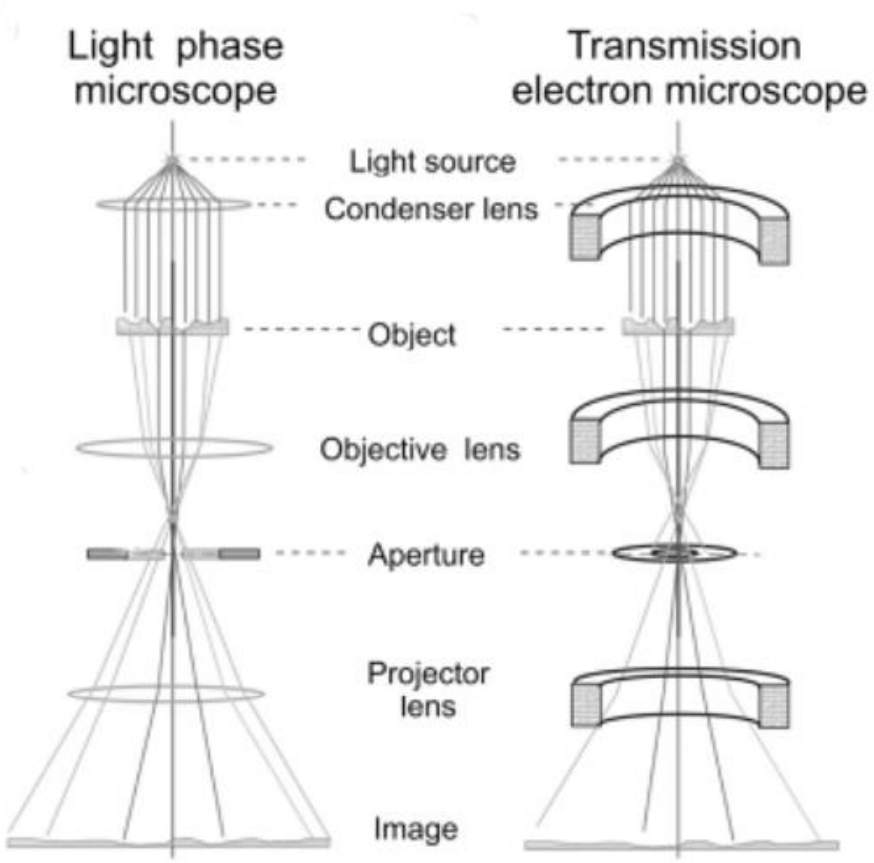

Fig. 2.3 Comparison of light and transmission electron microscopes. Reprinted from Chemical Reviews, Vol 12, Orlova E. *et al*. Structural analysis of macromolecular assemblies by electron microscopy and image reconstruction, P 91. Copyright (2011), with permission from Elsevier.

2.4.2 Direct electron detector

The most exciting technological breakthroughs in cryo-electron microscopy (cryo-EM) in recent years has been the development and application of DDD cameras. The detective quantum efficiency (DQE) of these cameras is significantly higher, at both low and high spatial frequency, than those of CCD cameras [105] (Fig.

2.4). The high DQE at high spatial frequency is good enough to retain high-resolution information, whilst, the image contrast that is needed for particle detection and alignment can be relaxed by the high DQE at low spatial frequency [105]. In addition to the dramatically improved DQE, the very high frame rate of the cameras allows images to be recorded as a movie series, so that moving objects can be aligned between the frames to produce sharper images [106]. The application of DDD cameras and the associated dose-fractionation movie technology has led to many high-resolution single-particle cryo-EM reconstructions at near-atomic resolution [29, 106, 107].

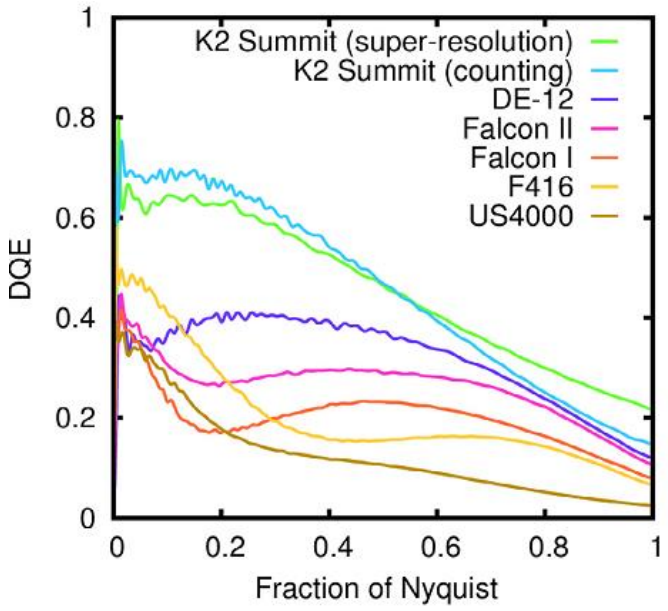

Fig. 2.4 DQE of detectors at 200 kV. The DEDs outperform scintillator-based detectors. The dose rates used were: K2 Summit in super-resolution mode – 4 electrons/pixel/s; K2 Summit in simple counting mode – 3 electrons/pixel/s; DE-12–

13 electrons/pixel/s with a frame rate of 25 frames/s; Falcon I (Brandeis) – 6 electrons/pixel/s; Falcon II (Brandeis) – 10 electrons/pixel/s; F416 – 50 electrons/pixel/s; US4000 – 40 electrons/pixel/s. Reprinted from Journal of Structural Biology, Vol 184, Rachel S *et al*, Quantitative characterization of electron detectors for transmission electron microscopy, P 385-393. Copyright (2013) [108], with permission from Elsevier.

2.4.3 Negative stain

Aliquots (~3 μl) of purified samples (LV, AiV, CVA16 VLPs and HAV complexed with R10) were diluted to ~0.5 mg/ml and deposited onto glow-discharged (this will make a carbon film surface negatively charged (hydrophilic) which allows aqueous solutions to spread easily) formvar carbon coated copper grids (Electron Microscopy Sciences, P.O. Box 550, 1560 Industry Road, Hatfield, US). After 30 seconds incubation, the excess sample was blotted away and the grids washed twice with deionized water. Samples were stained with 1% (w/v) uranyl acetate for 45 seconds and excess stain was removed by blotting. Grids were examined on a Tecnai T12 transmission electron microscope operated at 80 kV. Images were acquired on a 4k x 4k High-sensitivity FEI Eagle camera at 67000 x magnification which corresponded to 1.68 Å/pix sampling of the specimen.

2.4.4 Cryo-EM grids preparation and data collection

A 3 μl aliquot of purified virions (LV, AiV and HAV complexed with Fab (ratio of

~240 Fabs per virion)) at concentration of 1-2 mg/ml was applied to a freshly glow-discharged 200-mesh holey, carbon-coated copper grids (C-flat, CF-2/1-2C, hole diameter of 2.0 μm, edge to edge spacing of 1.0 μm ; Protochips Inc.) and blotted from both sides for 3 s, in 85% relative humidity for plunge-freezing (Vitrobot; FEI, Hilsboro, OR) in liquid nitrogen. Two-dimensional cryo-EM data were collected using an FEI Tecnai G2 Polara microscope (FEI, Hillsboro, OR) operated at 300 kV, equipped with an energy filter (GIF Quantum; Gatan, Pleasanton, CA) operating in zero-loss mode (0–20 eV energy selecting slit) and a direct electron detector (K2 Summit; Gatan, Pleasanton, CA). Micrographs were collected as movies (25~35 frames, each 0.2 s, total dose 25~35 e- Å-2) with a defocus between 1.5 and 3 μm in single electron counting mode using SerialEM at a calibrated magnification of 37,027 x, resulting in a pixel size of 1.35 Å.

2.4.5 Cryo-EM data processing and 3D reconstruction

2.4.5.1 Motion correction

With the advent of direct-electron detectors in 2012, the possibility arose to collect movies during the exposure of the sample to the electron beam. This allowed for two significant improvements that were previously inaccessible: beam-induced motion correction and radiation-damage weighting [109]. This beam-induced motion causes a blurring in the images that can be corrected by movie-processing, since each of the movie frames contains a sharper snapshot of the moving objects [109]. The

micrographs in this thesis were corrected for beam-induced drift by aligning and averaging the individual frames of each movie using MOTIONCORR [106]. Normally, the first 2 frames in each movie set have a relatively big drift and the last 3-8 frames bear serious radiation damage, therefore an optimized set of frames 3-20 were selected, corrected and averaged for the following structural analysis.

2.4.5.2 CTF correction

In contrast to a simple projection of a 3-dimensional object, the cryo-EM image of vitrified specimens is modulated by the contrast transfer function (CTF), which is directly related to the most important aberrations of the microscope, and is defined in Fourier space. The defocus and aberration of the lenses is the major factor that affects the CTF of cryo-EM image formation, modulating both the amplitudes and phases of the image [110]. Therefore original information of the images must be corrected with accurate CTF parameters to obtain a reliable 3D reconstruction (Fig. 2.5). Software used to estimate the CTF, includes CTFFIND [111] and Gctf [110]. In this thesis, CTF parameters for drift corrected micrographs were estimated using a GPU accelerated program Gctf [110]. Micrographs showing signs of astigmatism or significant drift were discarded and not used for further analysis.

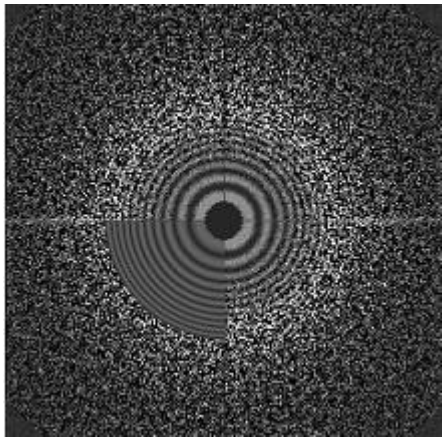

Fig. 2.5 One typical CTF estimation picture, output by CTFFIND4 [112]. Reprinted from Journal of Structural Biology, Vol 192, Alexis Rohou *et al*, CTFFIND4: Fast and accurate defocus estimation from electron micrographs, P 216-221. Copyright (2015) [108], with permission from Elsevier.

2.4.5.3 Particle picking and extraction

Particles were selected automatically by the ETHAN method [113] and then by manually screening with the boxer program in EMAN [114]. After picking the particles were extracted into small square images, called boxes, where the size of the box was typically set to around three times the radius of the viral particle of interest in Relion [115]. Upon particle extraction, the individual particle images were normalized to have zero-mean and unity-variance in the background noise area, which was defined as the area outside a circular mask.

2.4.5.4 2D classification

After extraction, the particles were subjected to the first round of reference-free 2D

class averaging (2D classification) in Relion version 1.3. Essentially this tries to align the various images and group them into common projections of the structure – 2D classes. This task was performed using the regularised likelihood optimisation algorithm and led to the calculation of reference-free 2D class averages [109], which typically provided useful insights into the quality of the data. Manual inspection of the resulting 2D class averages was used to select "good particles" for the following 3D reconstruction.

2.4.5.5 3D classification and 3D reconstruction

Cryo-EM structures of LV and AiV in this thesis were determined with Relion version 1.3 [115] by following recommended gold-standard refinement procedures [116] and applying icosahedral symmetry restraint. In brief the gold-standard procedure allows reliable validation of reconstructions by splitting the data into two and performing independent analysis of the two halves. Comparison of the two independent results then allows unbiased estimation of resolution. Reference-free 2D classification was used to select "good particles". The crystal structure of the HAV full particle, low-pass-filtered to 40 Å, or the initial model created by a program e2initialmodel.py intergrated in EMAN2 (a set of good 2D-class-averages were used to generate a set of 3D models with an icosahedral symmetry restrain) [117], was used as an initial model for 3D classification and 3D refinement using Relion. Both gave similar results. In 3D Auto-Refine, the estimated angular accuracies were used

to automatically increase angular sampling rates during the refinement up to the point where the noise in the data prevented one from distinguishing smaller angular differences, which led to the calculation of high-resolution reconstructions [109]. In addition, the post-processing approach in Relion with the application of a negative B-factor (automatically calculated by Relion) led to sharpening of the reconstruction map. For some relatively small particles (molecular weight less than 1 M Dalton), following beam-induced movements by aligning particles in running averages of a few movie frames may become very noisy. The particle-polishing procedure within Relion makes this procedure more robust [115] and further improves the resolution. However, the viral particles studied in this thesis are quite large (> 30 nm in diameter), no detectable improvements on the viral particle reconstructions were observed, therefore we gave up using the particle-polishing procedure. The final resolution was evaluated using the "gold" standard Fourier shell correction (threshold = 0.143 criterion) [116] of the two truly independent reconstructions. Due to the limit that FSC produces a single resolution for the entire density map, we also evaluated the local resolution for cryo-EM maps (calculated by Resmap[118]) in this thesis. The dataset and refinement statistics are summarized in Tables in the individual chapters.

2.4.6 Model building and refinement of EM models

The atomic models of LV or AiV VP0, VP1 and VP3 were built de novo into the

electron potential map with the structures of HAV capsid proteins as a guide, using COOT [96]. REFMAC [119] was used to calculate difference map which highlighted the areas where the model was incorrect. Models were further improved by iterative positional and B-factor refinement in real space using Phenix (using phenix.real_space_refine) [120] and COOT [119] iteratively. Only coordinates were refined, the maps were kept constant. Each round of model optimization was guided by cross-correlation between the map and the model. The crystal structures of HAV full particle and R10 Fab were used to fit the HAV-R10 Fab complex map. Initial fitting was done manually using the program CHIMERA [102], then optimized using the "Fit in Map" function in CHIMERA [102]. The fit was further improved with real-space refinement with COOT [119] and further refined in a similar fashion to that employed for LV and AiV.

2.5 Biophysical and biochemical assays

2.5.1 Thermal stability assay

Thermal stability assays, also called Pastry [121] experiments, were performed with an MX3005p RT-PCR instrument (Agilent). Both dyes SYTO9 and SYPRO-Red (Invitrogen) were used to detect the presence of RNA and the exposed hydrophobic regions of proteins respectively [29]. 50-µl reactions were set up in a thin-walled PCR plate (Agilent), containing 1 µg of the LV or AiV or HAV or CVA16 virus, 5

mM SYTO9 and 3 x SYPRO-Red in PBS (pH 7.4), and the temperature ramped from 25 to 99 ˚C, with fluorescence recorded in triplicate at 1 ˚C intervals. The melting temperature, Tm, was taken as the minimum of the negative first derivative of the denaturation curve.

2.5.2 Inhibition of AiV infection in vero cells by peptides [107]

For pre-attachment assays, peptides at different concentrations ranging from 5 nM to 50 μM were incubated with AiV at a multiplicity of infection (MOI) of 0.5 or with vero cells at 37 ℃ for 1h, then the virus-peptide mixtures were added into vero cells or the cells incubated with peptides were inoculated with AiV at MOI of 0.5 and with AiV without peptides as a control. For the post-attachment assay, vero cells were infected with AiV at MOI of 0.5 at 37 ℃ for 1h and peptides at different concentrations were subsequently added. Cells exposed to concentrations of peptides ranging from 5 nM to 50 μM alone were used to evaluate the cytotoxicity. Cells were cultured in DMEM supplemented with 1% FBS and grown at 37 ˚C with 5% CO_2. At 48 h post infection (p.i.), we observed the cells to evaluate the appearance of CPE.

2.5.3 Phospholipase assays

We examined the phospholipase activity of LV 2A2 by the EnzChek® phospholipase A2 assay Kit (Invitrogen) according to the instructions of the manufacturer.

2.5.4 Circular dichroism analysis

The secondary structure content of LV 2A2 at different pHs was detected using

circular dichroism. The LV 2A2 protein was diluted to 200 μl with a final concentration of 0.2 mg/ml at the indicated pHs. This experiment was carried out in a Chirascan Plus circular dichroism spectrometer (Applied Photophysics, UK). The circular dichroism was monitored at 37 ℃ from 250 nm to 320 nm, with a step size of 1nm. The content of secondary structure was calculated by using the CDNN CD Spectra Deconvolution Software.

Chapter 3
Structural study of Ljungan virus and potential mechanism for genome encapsidation

3.1 Introduction to parechoviruses

The genus *Parechovirus* is comprised of three species, human parechovirus (proposed new species name "*Parechovirus A*"), Ljungan virus (proposed new species name "*Parechovirus B*") and a new virus, Sebokele virus from rodents [122]. Human parechoviruses (HPeV) can cause mild, gastrointestinal or respiratory illness, but have been implicated in cases of myocarditis and encephalitis. More than 95% of humans are infected by human parechoviruses early in life, within two to five years of age [123]. Up to now, 16 different types of HPeV have been identified. Ljungan virus (LV), isolated recently from bank voles in Sweden, has been proposed as a zoonotic virus, potentially associated with diabetes and intrauterine fetal death in humans [124, 125]. Five LV genotypes have been characterized, three of which were isolated in Sweden and another 2 strains were identified in the USA. Sebokele virus 1 (SEBV-1), most closely related to LV, was isolated from rodents in 1972. The P1 region is the genomic region of SEBV1 most divergent from the most closely related picornaviruses, with identities of 56% with LV and 36% with HPeV whilst the non-structural P2 region of SEBV1 shows 70% amino acid sequence identity with LV and nearly 48% with HPeV [126].

Parechoviruses exhibit several distinctive features, including the lack of the final, assumed RNA catalyzed, maturation cleavage of the capsid protein precursor VP0 to VP2 and VP4 [8, 127], the existence of an approximately 20 amino acid extension

enriched with basic residues at the N terminus of VP3 [127, 128] and a different type of 2A protein [129]. Compared to HPeV, the N-terminus of LV VP0 is shortened by some 30 residues and does not contain the myristylation signal GXXX(S/T) [130] typical of the majority of picornaviruses. A major difference between HPeV and LV is located at the C terminus of VP1 – LV does not possess the arginine-glycine-aspartic acid (RGD) motif found in HPeV1 important for cell surface interaction with integrin receptors [131], but instead contains a unique 42 amino acid extension. To date no receptors have been identified for LV.

3.2 LV production, purification and characterization

Virus generated from cDNA infectious clones showed a clear cytopathic effect (CPE) at 3 days post-infection (see Chapter 2.1.3). LV was grown in GMK cells and purified by centrifugation, ultrafiltration, discontinuous sucrose density ultracentrifugation and sucrose density gradient ultracentrifugation (see Chapter 2.1.3). Unlike EV71, CVA16 and HAV, only one type of LV particles was observed by ultracentrifugation (Fig. 3.1). SDS-PAGE for viral protein composition analysis showed the three capsid proteins, VP0, VP1 and VP3 (Fig. 3.1). The λ260/λ280 absorbance ratios (1.64) and negative stain transmission electron microscope indicated that these particles were mature virions, containing RNA (Fig. 3.1).

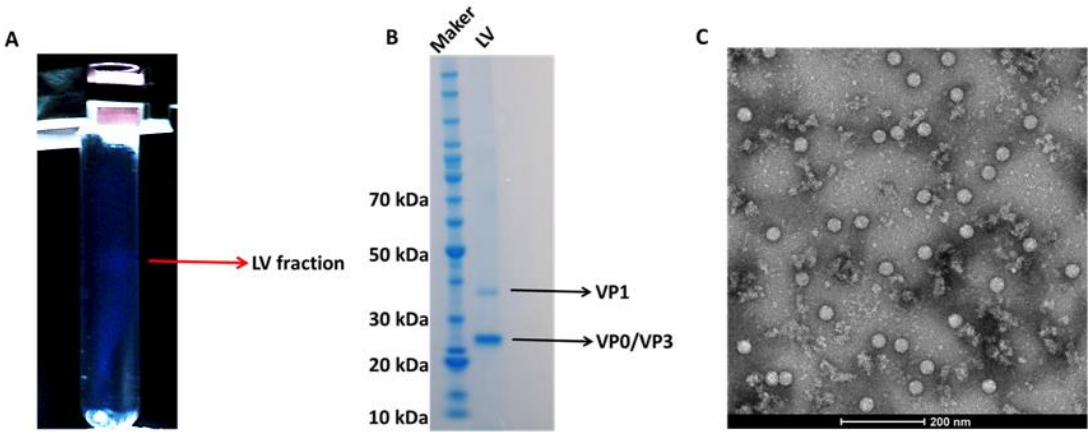

Fig. 3.1 LV purification and characterization. (A) Zonal ultracentrifugation of a 15 to 40% sucrose density gradient for purification of LV. (B) SDS-PAGE for viral protein composition analysis using a NuPAGE 4-12% Bis-Tris Gel (Invitrogen). The calculated molecular weights of VP0, VP1 and VP3 were 28.2 kDa, 33.1 kDa and 27.7 kDa respectively. (C) Negative stain electron microscopy of LV particles.

3.3 LV cryo-EM data collection and structure determination

Cryo-EM micrographs of purified LV virions were recorded using an FEI Polara electron microscope equipped with a Gatan K2 Summit detector (Table. 3.1) (see Chapter 2.4.2). A total of 5588 particles were selected from 328 cryo-EM aligned image stacks (Fig. 3.2) and subjected to 2D alignment and 3D reconstruction by single particle techniques using Relion [115]. Details for 3D reconstruction are included in Chapter 2.4.5. The particle-polishing procedure within Relion can improve resolution of the reconstruction dramatically for some cases, in particular for some small particles (sub-MegaDalton). Regarding the much larger viral particles studied in this thesis, we gave up the application of particle-polishing during our reconstruction due to no detectable improvement in the reconstructions. The final overall resolution was 3.78 Å (Fig. 3.2) using the 'gold standard' Fourier shell correction (threshold = 0.143 criterion) [116]. Local resolution calculated by Resmap [118] indicated that the core capsid had a resolution of ~3.2 Å whilst the resolution of the interior parts of the map (corresponding to RNA density) was ~7-8 Å (Fig. 3.2).

Table. 3.1 Cryo-EM imaging and data processing statistics.

Statistics	LV
Micrographs (total)	292
Micrographs (used)	288
Particles selected	5867
Particles included in final reconstruction	5558
Sampling, Å per pixel	1.35
Defocus range, μm	1.5-3.0
Resolution, Å	3.78
(gold standard FSC = 0.143 criterion)	

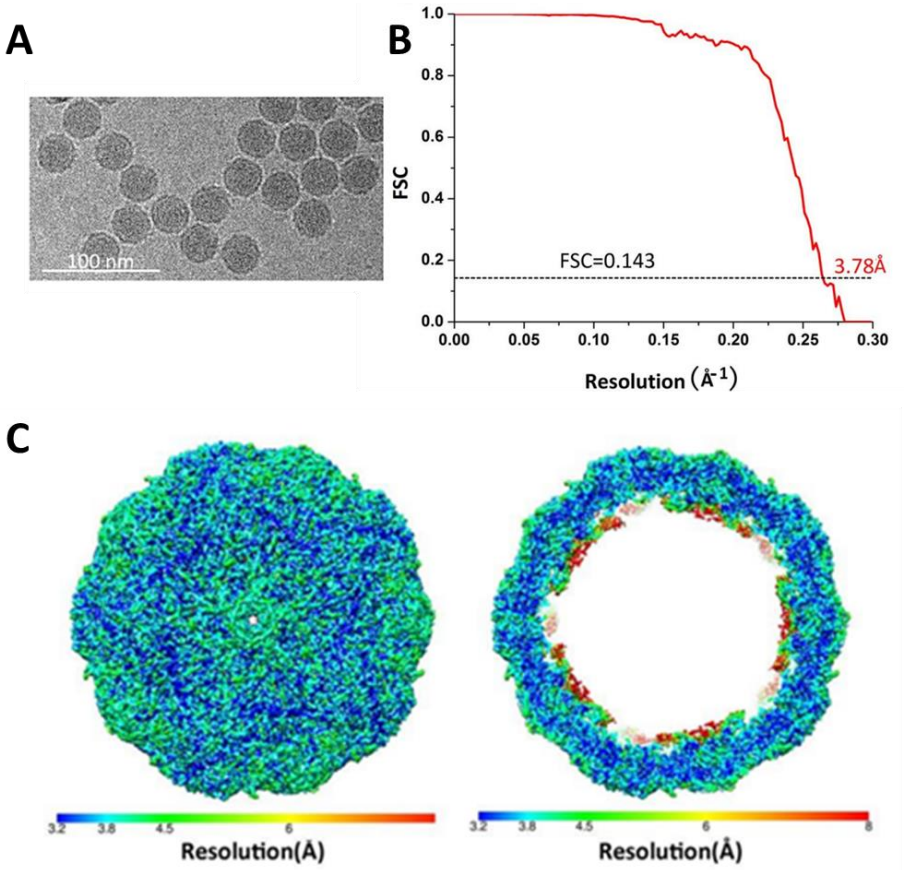

Fig. 3.2 Single particle 3D reconstructions of LV. (A) Cryo-EM image of LV. (B) The gold-standard FSC curves of the final maps. The resolution at FSC=0.143 is 3.78 Å. (C) The local resolution analysis for the LV map evaluated by ResMap [118] showing a resolution distribution from 3.2 to 8Å. Core parts of the map have resolution of ~3.2Å, the resolution of the interior parts of the map (corresponding to RNA density) is ~7-8 Å.

At the resolution of 3.78 Å, the polypeptide main-chain and side-chains were well resolved for the majority of the capsid (Fig. 3.4), allowing manual tracing of almost the entire capsid structure, assignment of the sequence to the density, building an atomic model of the three capsid proteins and refinement of the model (see Chapter 2.4.6 for a description of the methods). We used standard X-ray crystallographic metrics, including R-factor, real-space correlation and Ramachandran plot, to validate the refined structure (Table. 3.2). The ramachandran plot for the refined LV protomer model is show in Fig. 3.3.

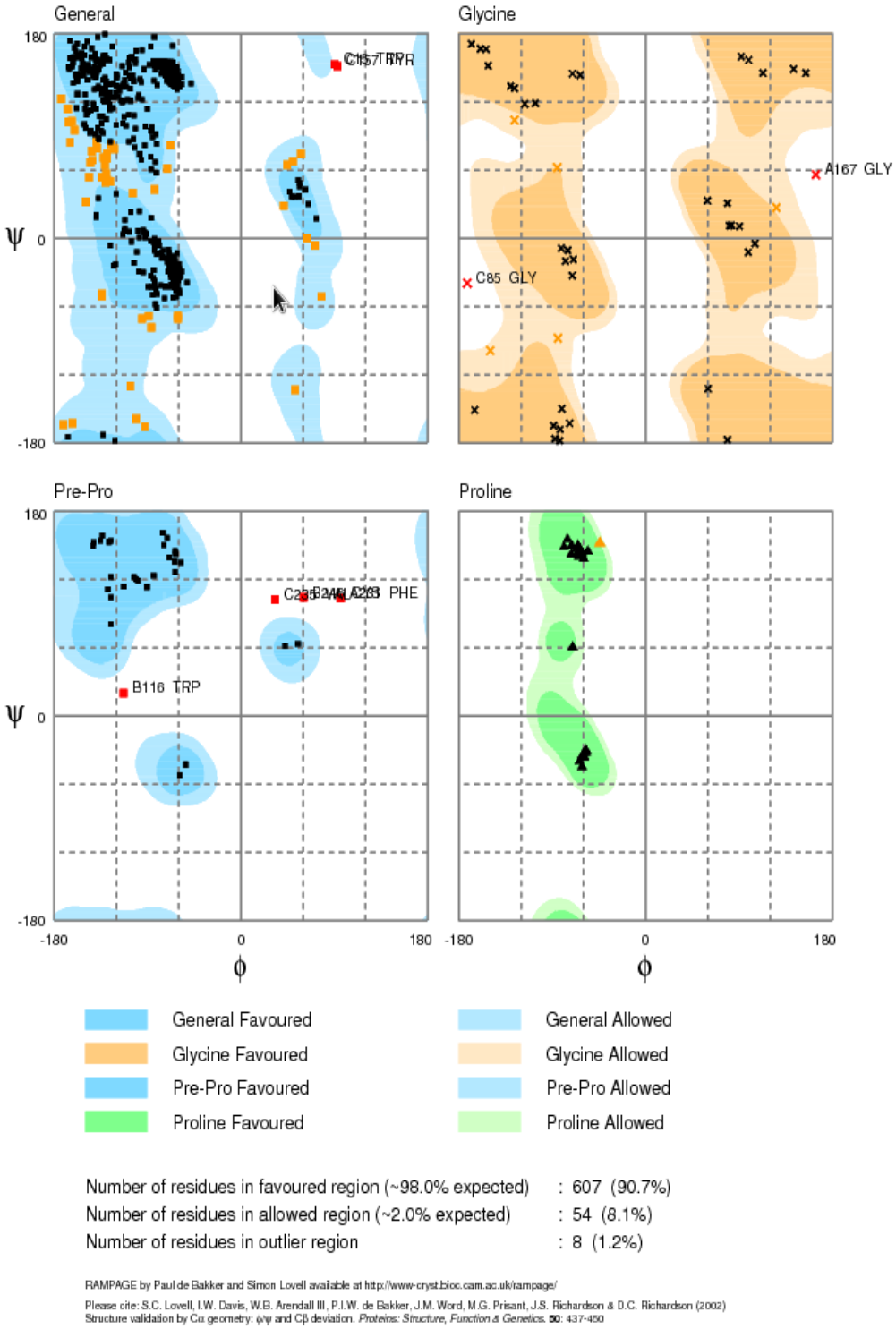

Fig. 3.3 Ramachandran plot for the refined LV model (a protomer)

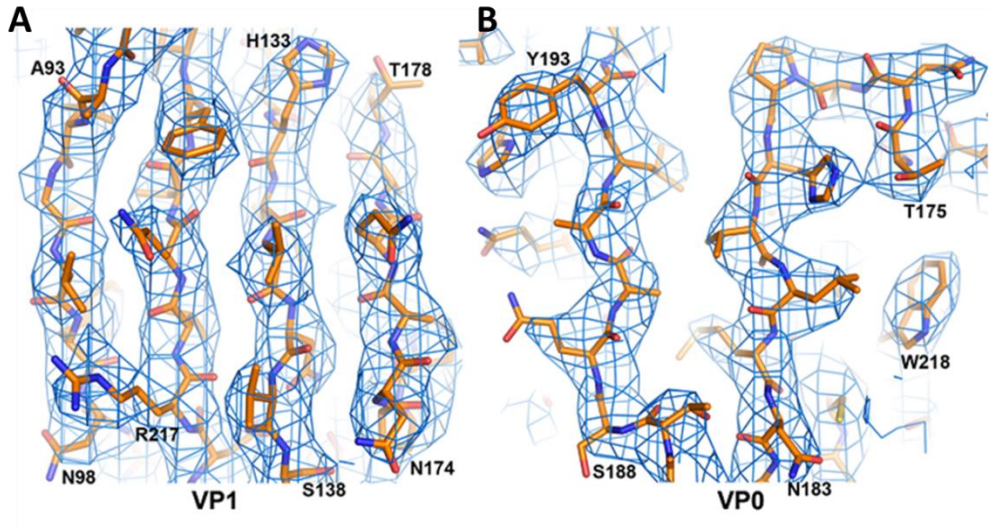

Fig. 3.4 Electron density maps. (A) From a section of VP1. (B) From a section of VP0.

Table. 3.2 Model refinement statistics.

Statistics	LV
Rmsd (bond angles, °)	1.573
Rmsd (bond lengths, Å)	0.010
Ramachandran statistics	
Most favored (%)	90.7
Allowed	8.7
Outliers	1.2
Rwork/Rfree (%)	29.7/31.3

3.4 LV overall structure

There are very remarkable (20 Å high) protrusions displaced some 45 Å from the icosahedral 5-fold axes. This “spike-like” structure is unprecedented in picornaviruses. The external surface is otherwise broadly similar to other picornaviruses, although relatively smoother than most, being most similar to HAV [25], whilst less angular. There is no trace of the enterovirus canyon, often the site of receptor binding [20], since relatively short BC, DE, GH loops of VP1, and EF loops of VP0 ablate the north and south walls of the canyon (Fig. 3.5). The transverse central sections of the LV 3D maps emphasize the internal differences, drawing attention to the prominent density corresponding to the genomic RNA involved in visible contacts with the protein shell at the fivefold axes (Fig. 3.5).

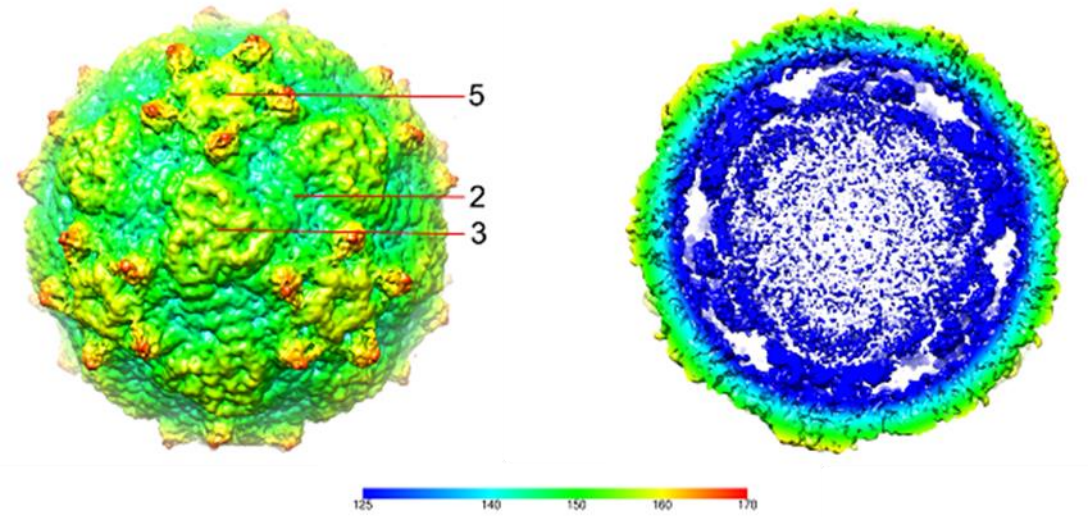

Fig. 3.5 Overall structure of LV (Left) and the central section of the LV particle viewed down the three-fold axis (Right). (Left) The surface is colored by radius blue through green to red from the lowest to the highest radius. The icosahedral 5-fold, 3-fold and 2-fold axes are labelled as 5, 3, and 2 respectively. (Right) A thin slice of the central section of the LV particle viewed down the 3-fold axis.

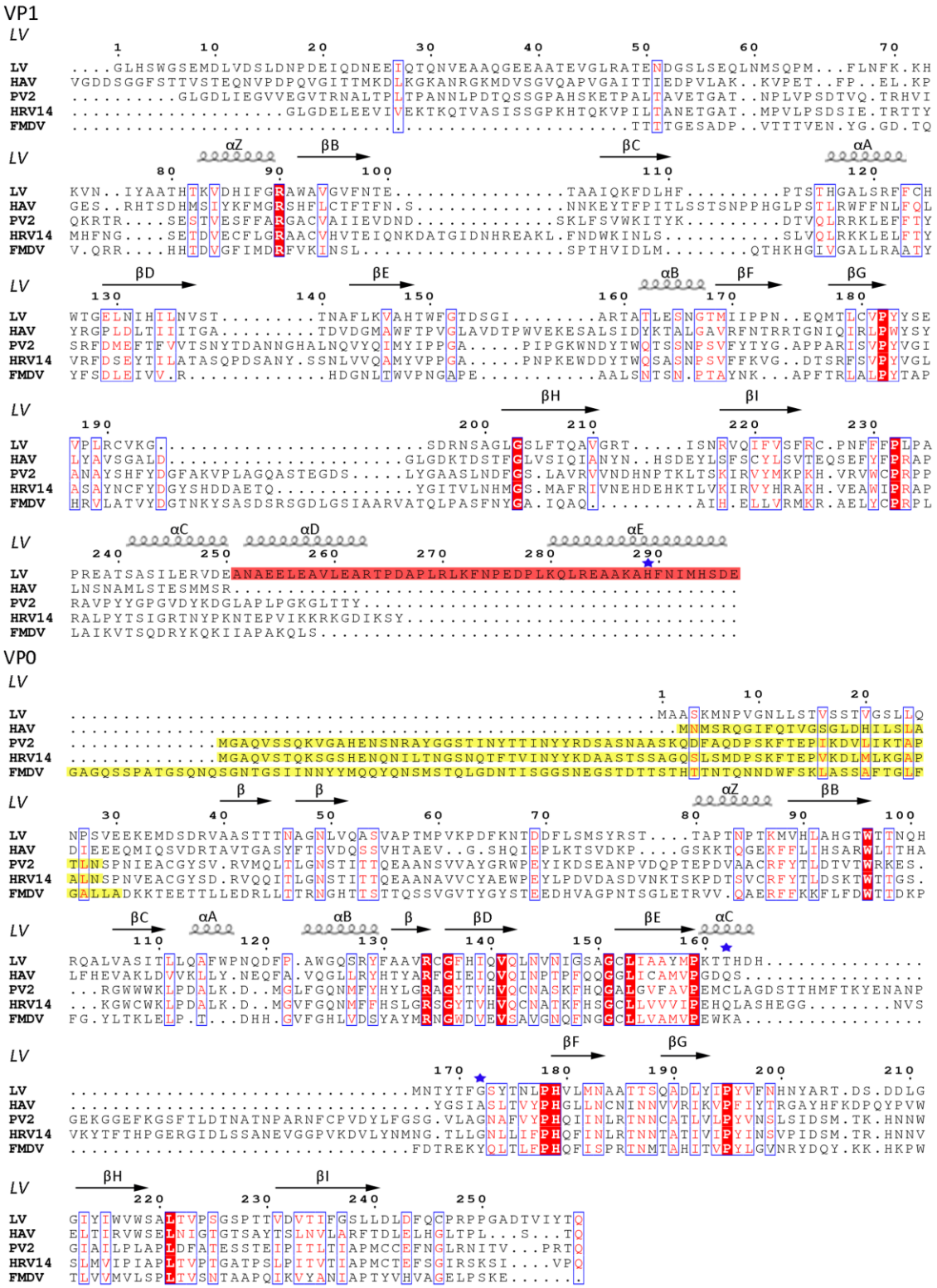
VP1
LV
HAV
PV2
HRV14
FMDV
VP0

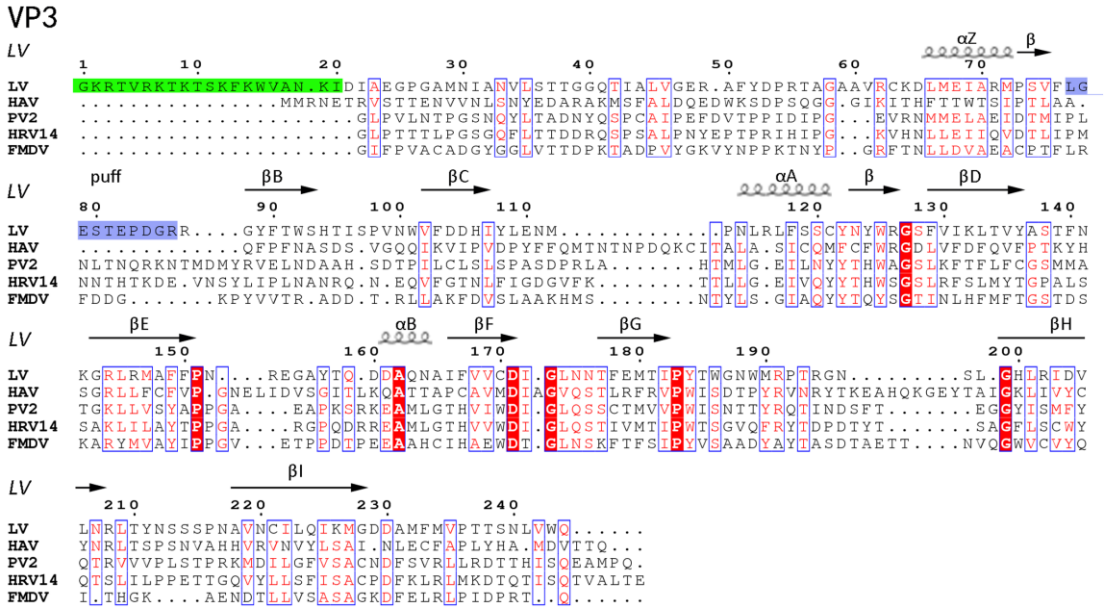

Fig. 3.6 Multi-sequences alignment of LV with other picornaviruses. Espript [100] representation of a structure-based sequence alignment of VP1, VP0 and VP3 of the LV particle with representative piconaviruses, including hepatitis A virus (HAV), poliovirus type 2 (PV2), human rhinovirus 14 (HRV14) and foot-and-mouth disease virus (FMDV). The secondary structural elements for LV are shown, also above the sequences are symbols which show features described in the text. The unique extension of the VP1 C-terminus in LV is highlighted in purple. An approximately 20 amino acids extension enriched with basic residues to the N terminus of VP3 in parechoviruses is marked in green. VP4 sequences of HAV, PV2, HRV14 and FMDV are shown in yellow. A puff configuration in VP3 of LV is represented in blue. The residue numbers are for LV.

3.5 Structural analysis of LV capsid proteins

The LV capsid is mostly well ordered, apart from residues 1-30 of VP1, 1-36 of VP0 and 1-3 of VP3. The capsid proteins (VP0, VP1 and VP3) adopt the expected eight-strand anti-parallel barrel configurations and are arranged with pseudo T = 3 (where T is the triangularation number) such that VP1 surrounds the five-fold axes, and VP0 and VP3 alternate about the two- and three-fold axes. The structures of the three proteins are shown in Fig. 3.7. Perhaps correlated with the absence of a canyon, LV does not harbour a continuous hydrophobic pocket in VP1. A lengthened H strand and alternative conformation of the GH loop block what would be the entrance of the pocket, whilst the C, E, F and H strands shift to compress the hydrophobic pocket volume, and these conformation changes decrease dramatically the volume to ~ 490 $Å^3$ (calculated by CAVER[132]) in compared with the volume of ~ 1000 $Å^3$ of the pocket in EV71 mature virion. So that it can no longer accommodate lipidic pocket factors (Fig. 3.8).

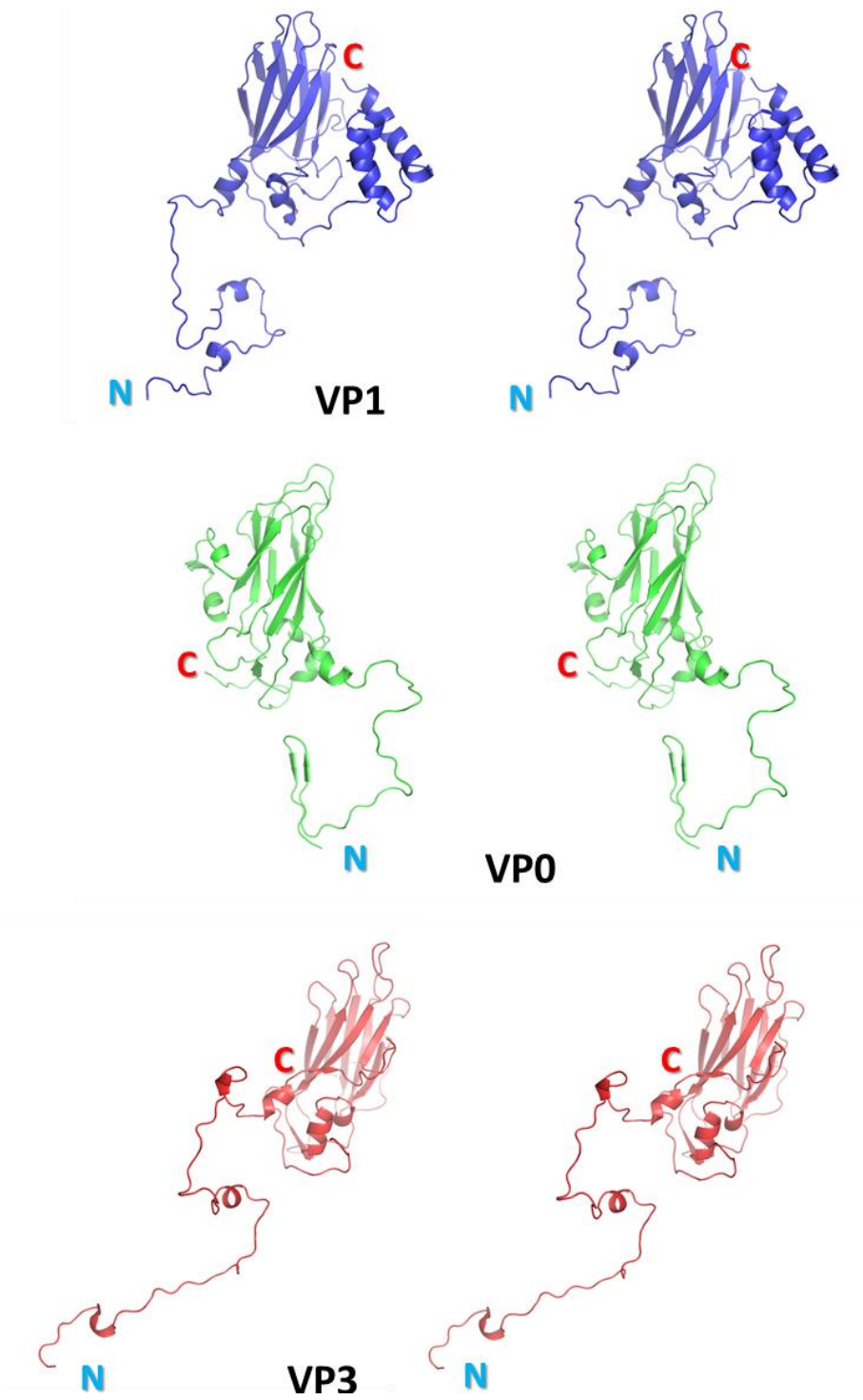

Fig. 3.7 Stereo views of the LV capsid proteins. VP1, VP0 and VP3 are colored in

blue, green and red respectively with N-terminus and C-terminus labeled.

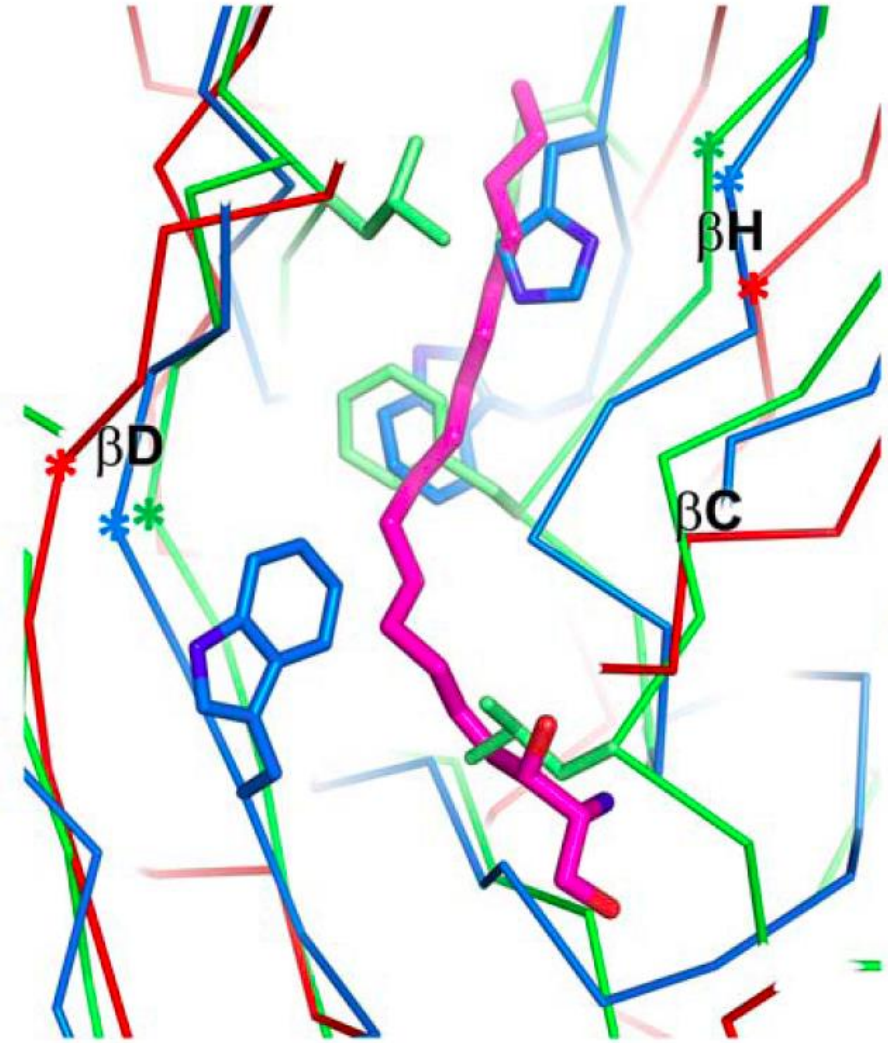

Fig. 3.8 Pocket analysis. Close-up view of LV (blue) and HAV (green) compared with VP1 pocket factor binding region of EV71 (red; pocket factor, magenta), note the shift of strand C and strand H and occlusion of pocket entrance. Bulky side chains occlude the HAV and LV pockets.

LV VP1 most closely resembles HAV, which also does not bear a pocket factor (RMSD in Cα is 2.5 Å). LV VP0 is strongly similar to HAV VP2 (RMSD in Cα is 1.8 Å, sequence similarity reaches up to ~40%). Sequence alignment analysis (Fig. 3.6) indicates that a short counterpart (~27 residues) of HAV VP4 exists in LV VP0, although both structures of HAV VP4 and LV VP0 N-terminus (1-36) are disordered. LV also uses a VP2 N-terminal switch, which prior to HAV had been observed only in the insect picorna-like viruses (Fig. 3.7 and Fig. 3.14). Unexpectedly, the overall fold of VP3 is most closely similar to HRV 2 with an RMSD of 1.5 Å, although LV harbors an N-terminal extension, internal to the capsid, responsible for interacting with RNA (Fig. 3.7).

3.6 Stability analysis

Like HAV, LV capsid proteins can withstand a remarkably high temperature and low pH (remaining stable up to 90 °C and at pH's down to about 2), even more robust than HAV capsid proteins [25], however genomic RNA becomes exposed at a significantly lower temperature (~60 ℃) with little variation in stability with pH, this being ~10 ℃ lower than the capsid dissociation temperature of HAV (Fig. 3.9). In enteroviruses capsid protein melting occurs in two distinct steps indicative of a two-stage transition in protein conformation, in contrast LV only underwent the higher temperature conformational transition (Fig. 3.9) which is consistent with the observation that alternative particles of parechoviruses cannot be produced by heat-treatment [127]. These results indicate that LV probably uncoats via a novel mechanism, which is different from those utilized by most other picornaviruses, although possibly similar to HAV [25].

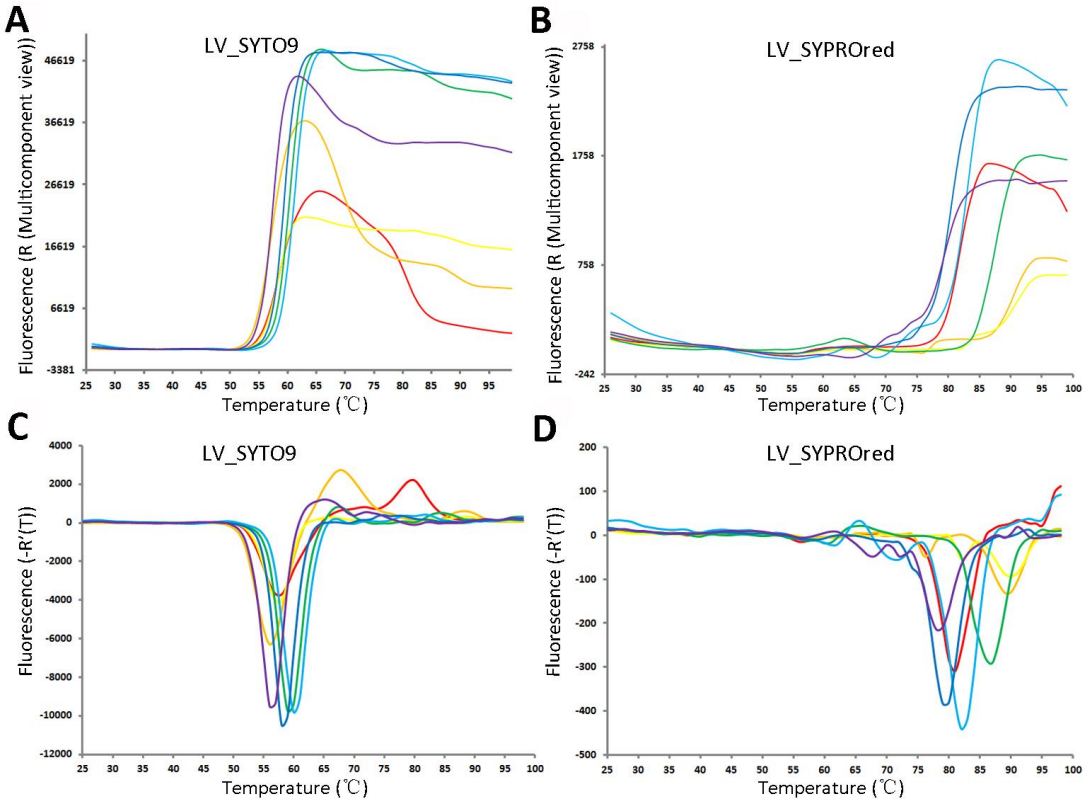

Fig. 3.9 Thermal stability of LV particles. To characterize the stability of the LV particles across the pH range from 4.0 to 10.0, differential scanning fluorimetry assays were performed with dyes SYTO9 (to test for RNA exposure) and SYPRO-Red (to test for protein melting). (A) and (B) The raw fluorescence traces of LV particles incubated with SYTO9 and SYPRO-Red respectively. (C) and (D) The first derivatives of the fluorescence curves of LV particles incubated with SYTO9 and SYPRO-Red respectively. The color scheme is red (pH 4.0), orange (pH 5.0), yellow (pH 6.0), green (pH 7.0), sky blue (pH 8.0), blue (pH 9.0) and purple (pH 10.0).

3.7 Pronounced projections at the external surface surrounding the 5-fold axes

In comparison with other picornaviruses, one of the most striking differences of LV is the presence of pronounced protrusions at the external surface of the particle surrounding the fivefold axes (Fig. 3.10). Although these structures are not well ordered and are best seen in lower resolution reconstructions, it is unambiguous that the protrusions are formed from the C-teminus of VP1. The disorder precludes tracing the protein backbone for this domain (residues 242 to 297) but the predicted protein secondary structure would suggest the presence of three helices. Such a protrusion formed from a C-terminal extension is unique in picornaviruses, however, in Seneca valley virus there is a similarly sized and placed projection formed by loops from VP1 and VP2 and in the insect picorna-like virus triatoma virus (TrV [133]) there are such projections formed from insertions within the loops and sheets of VP1 and VP3 although displaced by ~13 Å (Fig. 3.10). For some picornaviruses, including HPeV1 and CVA9, an arginine-glycine-aspartic acid (RGD) motif present at the C-terminal of VP1 is responsible for the viral attachment to cellular integrins, however this motif is not present in LV, and indeed the LV extension contains no distinctive sequence motifs (Fig. 3.6).

To explore the potential roles of the VP1 C-terminus, we used the predicted three helices to search the structural similarity with the DALI server [134]. The most

structurally conserved match was a DNA binding protein O27018 from Methanobacterium thermoautotrophicum (DALI Z-score=4.2, RMSD=2.2 Å, over 87 Cα residues). Together with highly enriched charged residues (13 negatively charged and 8 positively charged residues), these suggest that the VP1 C-terminus could possibly play a role in binding cellular DNA to regulate host genes expression, like some universal stress proteins (USPs), for example USPs play a significant role in Salmonella growth arrest, stress and virulence [135]. Given that LV is most similar to HPeV, it is also possible that the VP1 C-terminus functions as a cell-attachment module that is swapped with the HPeV integrin-binding motif. Furthermore, cell adaptation mutants such as the Y289H replacement in the VP1 C-terminus, together with the A162T and S172G substitutions of VP0 (Fig. 3.11), greatly enhanced infectivity and induced a distinct cytopathic effect [136], interestingly the three residues are clustered together at the surface, suggesting that this region may be implicated in host cell recognition.

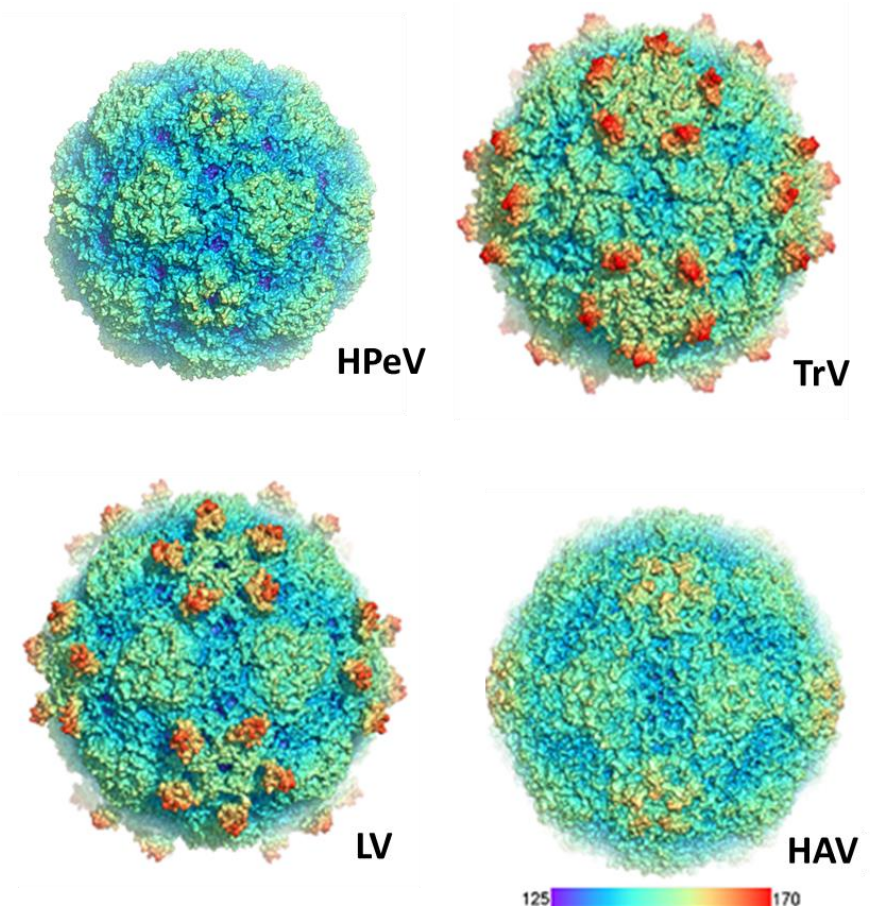

Fig. 3.10 Comparison of capsids from LV with HPeV, HAV and TrV. The capsids are colored by radius from blue to red according to the scale bar shown.

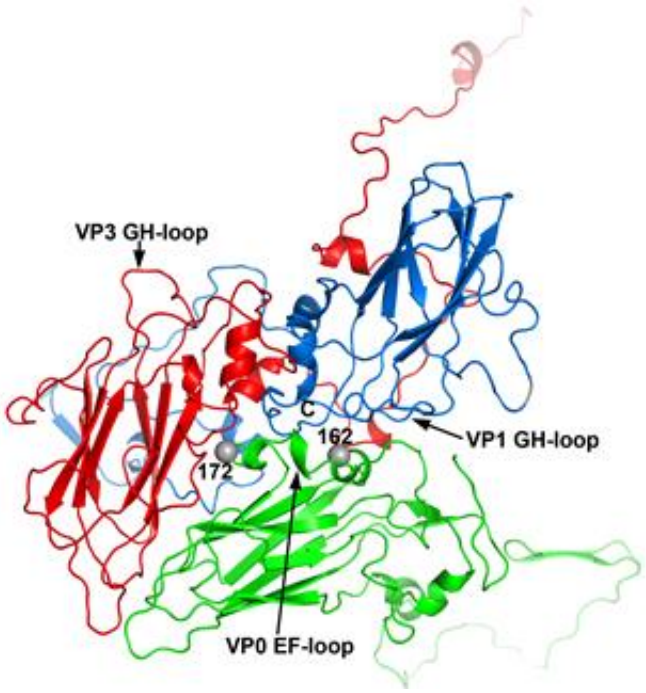

Fig. 3.11 Ribbon diagram of LV protomer with cell adapted mutations (residues 162 and 172) in VP0 EF loop shown as grey spheres. The third mutation Y289H at VP1 C-terminal region is not built in the model due to the lower resolution electron density map. VP1, VP0 and VP3 are colored in blue, green and red, respectively.

3.8 The N-terminal region of VP3 interacts with RNA genome

The extended N-terminal polypeptide of VP3 was well defined in the electron density map and we built the model from residue 4. Unexpectedly, the N-terminal polypeptide (from residue 64 to residue 4) of VP3 passes across the bottom of the five-fold vertex and inserts into the VP3 from another asymmetric unit at the inner surface of the protein shell (Fig. 3.12). Interestingly five prominent, ~5nm-long tornado-like regions of high density extending radically from the inner surface of the capsid and into the genome beneath each vertex are observed (Fig. 3.12). In addition to the density corresponding to the residues of the VP3 extension there is a considerable amount of additional density, which we identify as RNA, in part based on the shape of the electron density (Fig. 3.12). This feature was also observed in human parechovirus, although at lower resolution, so that it was not possible to identify the nature of the protein-RNA interactions [128].

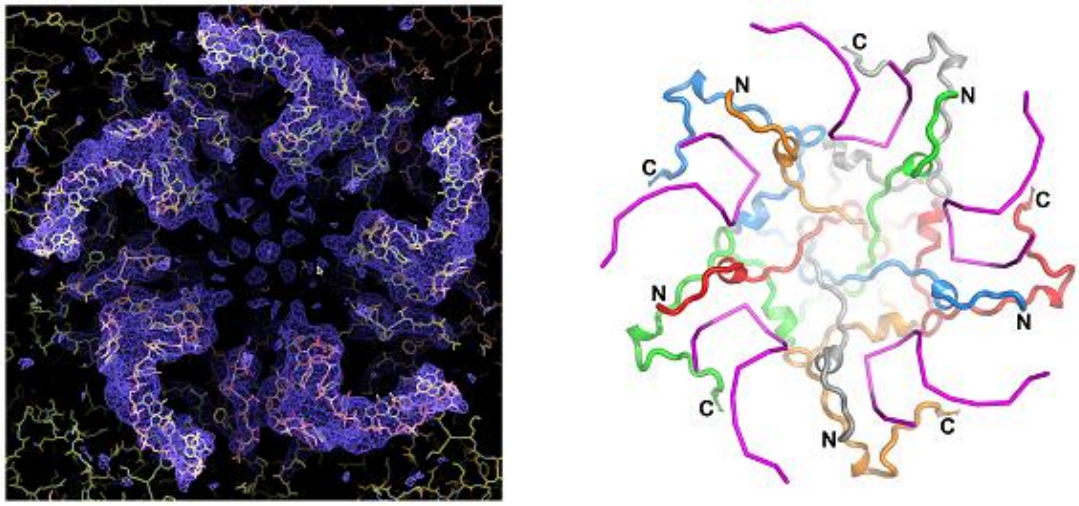

Fig. 3.12 The partial structure of the LV genome and overall structures of RNA and VP3 N-termini. (Left) Electron density for the N termini of VP3 and the ordered RNA around the five-fold axis; (Right) The structure of VP3 N termini around the five-fold axis (individual copies distinguished as blue, green, red, orange and grey ribbons, from residue 4 labeled N to residue 64 labeled C) and their proximity to the RNA (magenta).

Electrostatic interactions dominate the contact between the VP3 N-terminus and the RNA hairpin (Fig. 3.13). The N-terminal polypeptide (residue 1-64) bears 13 basic resides, most of which are clustered within the first 20 resides. A total of 65 basic residues from the N-terminal segments of VP3 from five icosahedral asymmetric units line up at the inner surface of the five-fold axes to produce a positively charged environment that partly attracts the abundant negative charge of the RNA phosphate groups. Residues including Arg 6, Lys 7, Lys 9, Lys 12, Lys 14, Arg 49, Arg 62, Lys 64 of VP3 and Arg 225 of VP1 are engaged in direct interaction with the ordered RNA (Fig. 3.13). In association with RNA, the N-terminal polypeptide, in particular the first 20 residues of VP3 functions as an assembly messenger to maintain the flat inter-protomer interactions that are critical for dimensioning the pseudo T = 3 particle [137], which is consistent with the lack of empty parechovirus particles in the viral life cycle.

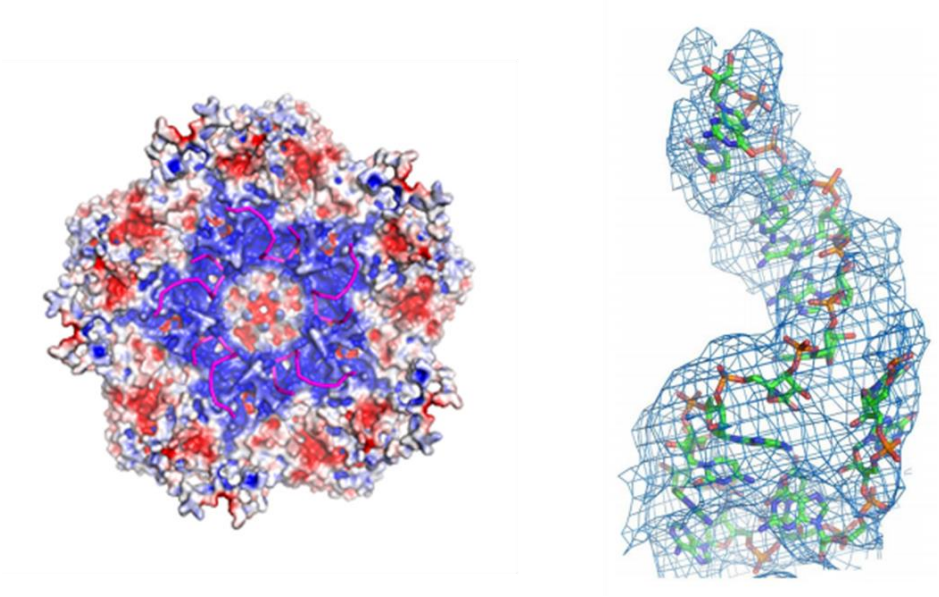

Fig. 3.13 Charge interactions between RNA and VP3 N-termini (Left) and close-up view of electron density for the ordered RNA (Right). (Left) Inner electrostatic surface of the LV pentamer showing the predominance of positive charge that interacts with the backbone of the genomic RNA (magenta sticks). (Right) The map is contoured at 3σ and the resolution is 7-8 Å. The nucleotide sequence is arbitary.

Our interpretation of the RNA electron potential map places 15 bases of RNA in close association with the N-terminus of VP3, with most of these base-stacked and involved in secondary structure. Density comparable to that of well-ordered protein was visible for the phosphate, sugar and bases of the ribonucleotides, which lie beneath the icosahedral fivefold axes. Since the structure is averaged by icosahedral symmetry, the 15 RNA bases are an average of the true sequence that they represent in each of the 60 unique segments (Fig. 3.13). The good quality of the density suggests that the VP3 RNA binding sites are essentially fully occupied, implying that the structural motif seen occurs some 60 times in the viral genome. Overall the ordered RNA comprises some 900 bases, 12% of the viral genome. Such well ordered genome RNA has only been observed in parechoviruses, not other genera of the *Picornaviridae*, however, packaged genome with double-stranded helices or stem-loops has been reported in insect and plant viruses [138, 139], which indicates that the genome encapsidation mechanism of the parechovirus genus differs significantly from other picornaviruses.

3.9 Evolutionary analysis for LV

Overall, LV shares some common characteristics of HAV, but also exhibits distinguishing structural features compared to previously characterized picornaviruses. In addition, LV possesses more structural similarities to insect

viruses, including a VP2 N-terminal domain swap, the presence of basic regions at the N terminus of VP3, pronounced projections at the external surface surrounding the fivefold axes and the observed well ordered genome RNA and numerous protein/RNA interactions (Fig. 3.10 and Fig. 3.12). A structure-based phylogeny suggests that LV lies evolutionarily closer to the insect picorna-like viruses in comparison with HAV (Fig. 3.14). Together with the other evidence presented here, this suggests that LV retains a number of structural and functional features characteristic of primordial picornaviruses, which had their origins in insect viruses, and that the subsequent acquisition of efficient mechanisms of cell entry allowed the explosion in diversity that characterizes present day picornaviruses.

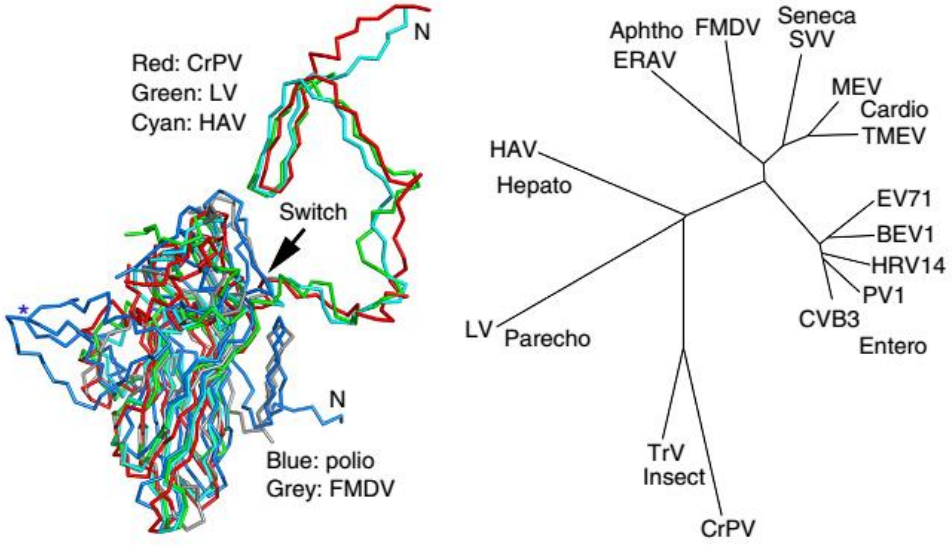

Fig. 3.14 Evolutionary analysis. (Left) Superposition of LV VP0 with VP2 of poliovirus, FMDV, HAV and CrPV. The N terminus of LV VP0 folds similarly to that of HAV and CrPV but differently to other picornaviruses. The star marks the EF loop that forms part of the south wall of the canyon in poliovirus. (Right) A Structure-based phylogenetic tree of representative picornaviruses and cripaviruses, respectively: CVB3, coxsackievirus B3; PV1, poliovirus type 1; HRV14, human rhinovirus 14; BEV1, bovine enterovirus type 1; EV71, EV-A71; TMEV, Theilers virus; MEV, Mengo virus; SVV, Seneca valley virus; FMDV, foot-and-mouth disease virus; ERAV, equine rhinitis A virus; HAV, hepatitis A virus; TrV, triatoma virus;

CrPV, cricket paralysis virus.

3.10 Implications for assembly for LV

Studies of the structures and assembly of some insect viruses (nodaviruses and pariacoto virus) have demonstrated that viral RNA acts as part of a molecular switch that determines the exact assembly of T=3 particle symmetry [140, 141]. In general, basic regions, often located at the N- or C- termini of the coat proteins are found in some icosahedral viruses and thought to be involved in RNA-protein interactions for encapsidating viral genome [67, 142]. Similar to some insect viruses, LV bears such a basic A/LRM motif at the VP3 N-terminus which has been verified to bind viral RNA [143]. Consistent with the LV structure, the viral RNA is highly condensed and shows an exceptional degree of secondary structure when packaged inside the virion. It is poorly understood how the viral RNA transits from an extended molecule to a highly compacted structure. Probably, the RNA spontaneously forms a series of local secondary structures, hairpin or duplex or stem-loop elements, dependent upon the nucleotide sequence. Then capsid proteins (mainly VP3 in parechoviruses) might act an RNA chaperone, folding the genome into a structure compatible with the icosahedral symmetry of the particle through numerous electrostatic interactions (Fig. 3.15). LV and HPeV might use this encapsidation mechanism, which differs from those of other picornaviruses.

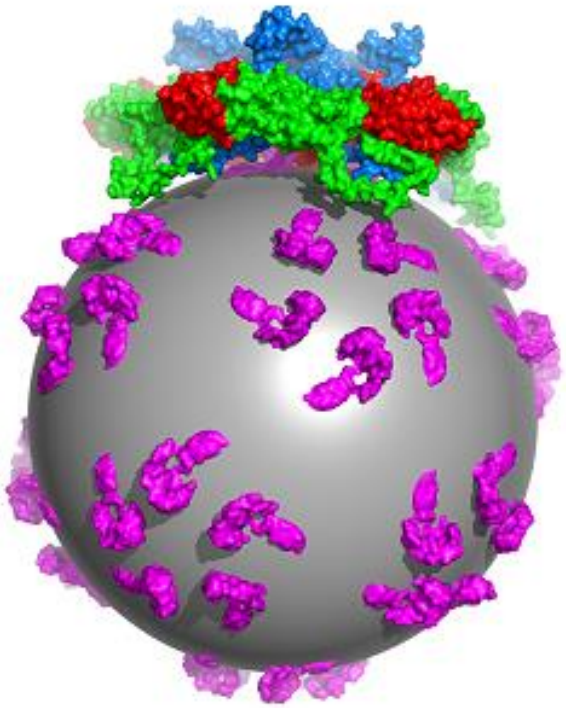

Fig. 3.15 Putative mechanism for LV encapsidation. Cartoon diagram representing the LV genomic RNA as a sphere with ordered fragments forming pentameric protrusions (magenta); the pentamers of capsid protein associate with the genome RNA through electrostatic interaction.

3.11 Conclusion

This chapter reports the determination of the atomic structure of LV at a resolution of 3.78 Å by cryo-EM. Detailed analysis of the structure in comparison to other picornaviruses and insect picorna-like viruses, shows that LV differs substantially in features on both the inner and outer surfaces, and remarkably reveals some 12% in the RNA genome forming icosahedrally ordered interactions with the capsid, with implications for encapsidation. These features presumably reflect functional adaptations providing different solutions to the problems of cell attachment and genome encapsidation which were explored early in the evolution of picornaviruses.

Chapter 4
Structure of human Aichi virus and implications for receptor binding

4.1 Introduction to Aichi virus

Acute gastroenteritis, caused mainly by viruses, is a leading cause of morbidity worldwide and an important cause of death in children below five years old especially in developing countries. Aichi virus (AiV), a member of the *Kobuvirus* genus, infects humans, usually subclinically, but can lead to acute gastroenteritis [144-146]. Seroprevalence of AiV is ~ 60% in children < 10 years old and reaches 90% later in life [147]. Although AiV is considered as a potential global public health threat, there is no available vaccine or effective antiviral treatment.

AiV has limited sequence similarity with other picornaviruses (15%-34% amino acid sequence identity), and exhibits several distinctive features. Like parechoviruses, AiV lacks the final, assumed RNA catalyzed, maturation cleavage of the capsid protein precursor VP0 to VP2 and VP4, but bears an extremely long (370 residues) VP0 with a myristoylation motif (GXXXT) at the N termini [148]. The AiV genome contains unusually high C content and a very high degree of genome-order RNA secondary structure [149]. Unlike most picornaviruses proteins L and 2A of AiV have neither a protease nor NPGP motif, but both are involved in viral RNA replication and encapsidation [150]. Furthermore, AiV is the sole picornavirus identified to contain an RNA encapsidation signal at the 5′ terminal RNA stem loop [148].

4.2 AiV production and purification

The aichi virus stock (strain A846/88, GenBank: BAA31356.1) was a kind gift from Dr. Teruo Yamashita in Aichi Prefectural Institute of Public Health, Japan. The virus was amplified using 40 x 175 cm^2 flasks of Vero cells inoculated at a multiplicity of infection (MOI) of 1. Detailed purification procedures for AiV are given in chapter 2.1.3. Sucrose density gradient purification produced two bands, one at a low density (1.02–1.15 g cm^{-3}) was identified as a pyruvate dehydrogenase complex from mycoplasma, by MALDI-TOF spectrometry; the other band, at the density expected for picornaviruses (1.25–1.30 g cm^{-3}) (the λ260/λ280 absorbance = 1.56), comprised mature viruses containing packaged RNA (Fig. 4.1). SDS-PAGE for viral protein composition analysis using a NuPAGE 4-12% Bis-Tris Gel (Invitrogen) suggests that AiV mature viruses consist of 3 capsid proteins, VP0, VP1 and VP3 (Fig. 4.1), which is consistent with previous reports. The calculated molecular weights of VP0, VP1 and VP3 were 39.1 kDa, 24.2 kDa and 29.9 kDa respectively. Electron microscopy showed mature viruses with morphology indistinguishable from other picornaviruses (Fig. 4.1).

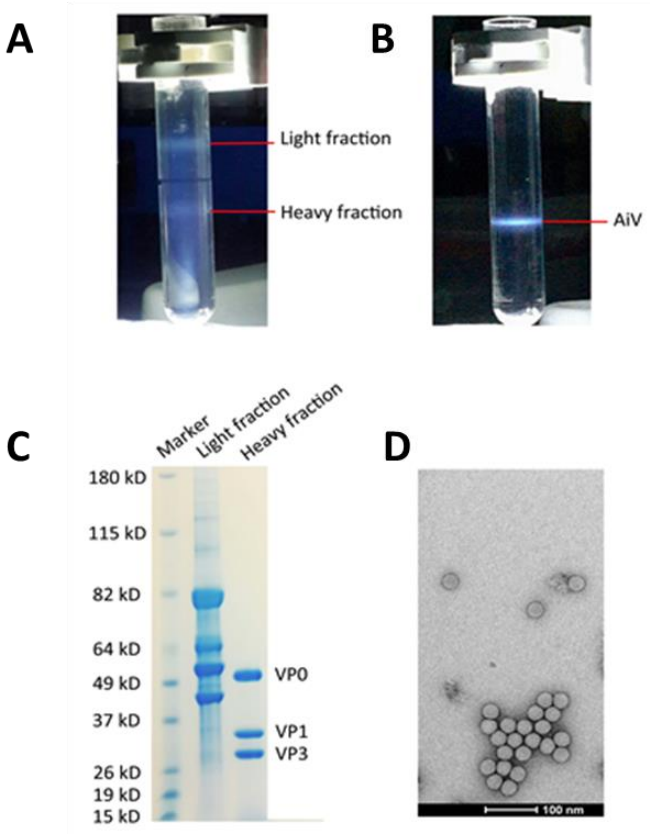

Fig. 4.1 AiV purification and characterization. (A) Zonal ultracentrifugation of a 15% to 45% (w/v) sucrose density gradient for the purification of AiV. (B) The heavy fractions were purified further with zonal ultracentrifugation of 35% to 55% (w/w) sucrose density gradient. (C) SDS-PAGE for viral protein composition analysis. (D) Negative stain electron microscopy of AiV particles.

4.3 Cryo-EM data collection of AiV and structure determination

In the same way as for LV, we imaged purified AiV using cryo-EM with a Polara microscope equipped with a Gatan K2 Summit detector (see Chapter 2.4). Micrographs were collected at defocuses between 1.6 and 3 μm as movies (25 frames, each 0.2 s, giving a total dose of 25 e^{-} $Å^{-2}$) in single electron counting mode using SerialEM at a calibrated magnification of 37,027×, resulting in a pixel size of 1.35 Å. Frames 3-22 were used and corrected for beam-induced drift by aligning and averaging the individual frames of each movie (see Chapter 2.4). A total of 25,279 particles from 776 micrographs were picked for the 2D alignment and 3D reconstruction using recommended gold-standard refinement procedures and applying icosahedral symmetry. Details for 3D reconstruction are included in chapter 2.4.5. The final overall resolution for AiV was 3.68 Å, which was evaluated using the "gold standard" Fourier shell correction (threshold = 0.143 criterion) (Fig. 4.2). The capsid parts of the map have a resolution of better than 3.0 Å, while, the resolution of the interior parts of the map (corresponding to the RNA genome) is ~8-30 Å (Fig. 4.2). The dataset is summarized in Table. 4.1. At an overall resolution of 3.68 Å the map was of sufficient quality to allow the atomic modeling of most capsid proteins (Fig. 4.3). The model was refined and validated using standard X-ray crystallographic methods. The refinement statistics are summarized in Table. 4.2. The Ramachandran plot for the refined AiV protomer model is shown in Fig. 4.4.

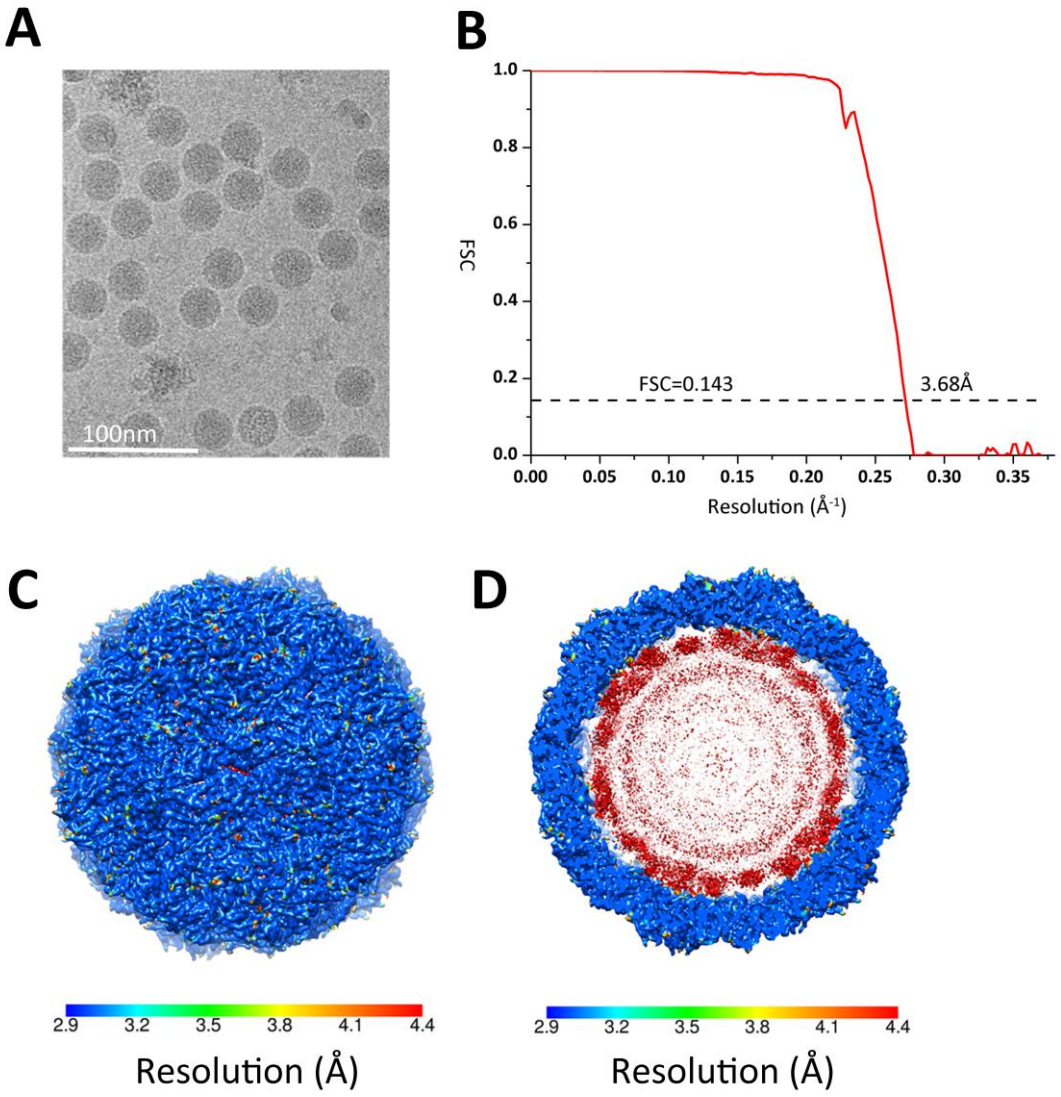

Fig. 4.2 Cryo-EM image and resolution evaluation of cryo-EM map of AiV. (A) Cryo-EM image of AiV. (B) The gold-standard FSC curves of the final maps with a resolution of 3.78 Å at FSC=0.143. (C) and (D) The final AiV map was analyzed by ResMap [118] showing a resolution distribution from 2.9 to 4.4 Å with displayed color scheme.

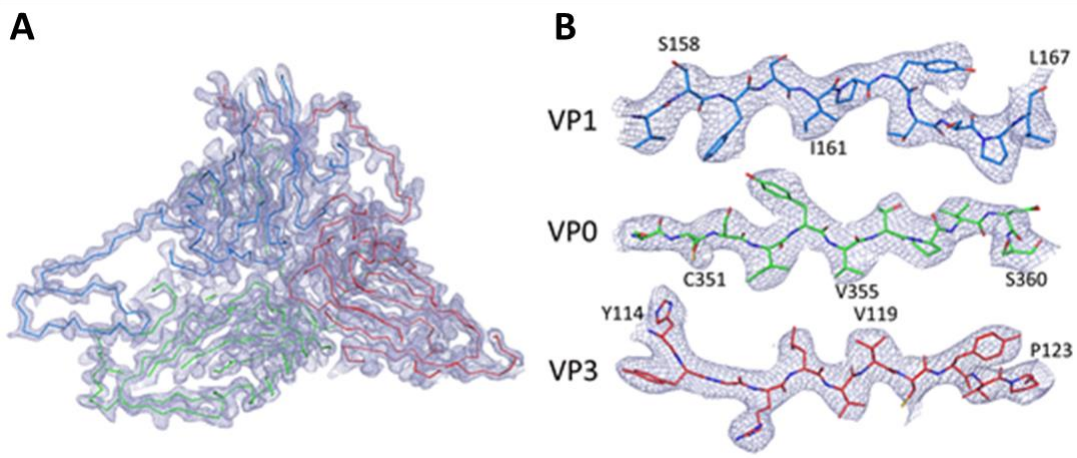

Fig. 4.3 Electron density maps. (A) A protomeric unit of AiV capsids, VP1, VP0 and VP3 is colored in blue, green and red respectively. (B) From the sections of VP1, VP0 and VP3.

Table. 4.1 Cryo-EM imaging and data processing statistics.

Statistics	AiV
Micrographs (total)	776
Micrographs (used)	668
Particles selected	25,279
Particles included in final reconstruction	18,566
Sampling, Å per pixel	1.35
Defocus range, μm	1.5-3.0
Resolution, Å	3.68
(gold standard FSC = 0.143 criterion)	

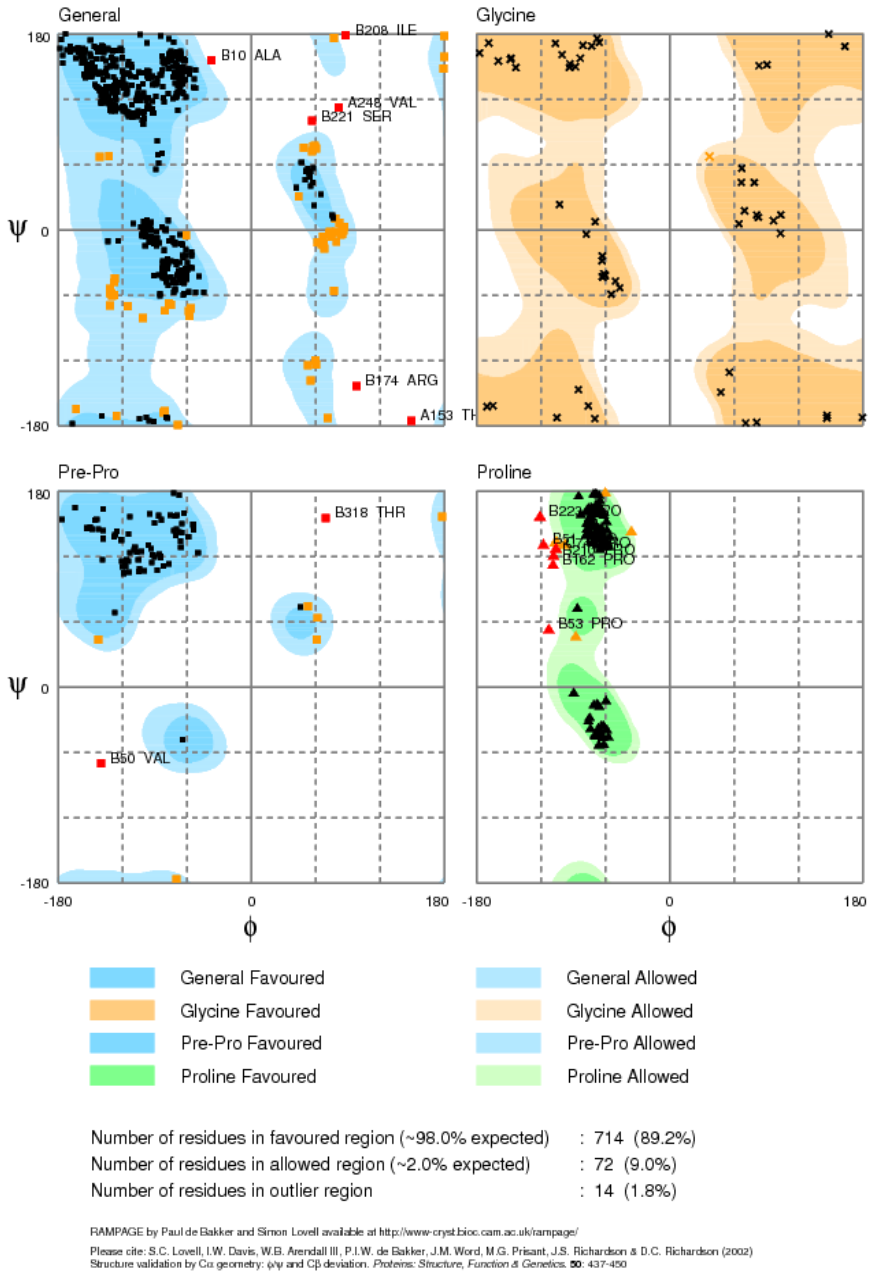

Fig. 4.4 Ramachandran plot for the refined AiV model (a protomer)

Table. 4.2 Model refinement statistics.

Statistics	AiV
Rmsd (bond angles, °)	1.522
Rmsd (bond lengths, Å)	0.010
Ramachandran statistics	
Most favored (%)	89.2
Allowed	9.0
Outliers	1.8
R_{work}/R_{free} (%)	32.6/32.9

4.4 Overall structure of AiV

The AiV capsid is well ordered, apart from a few disordered residues in VP0 (80-114) and VP1 (254-278). The capsid proteins (VP0, VP1 and VP3) adopt the classical eight-stranded anti-parallel barrel configuration and follow the expected pseudo T = 3 symmetry (where T is the triangulation number), such that VP1 surrounds the 5-fold axes and VP0 and VP3 alternate about the 2- and 3-fold axes (Fig. 4.5).

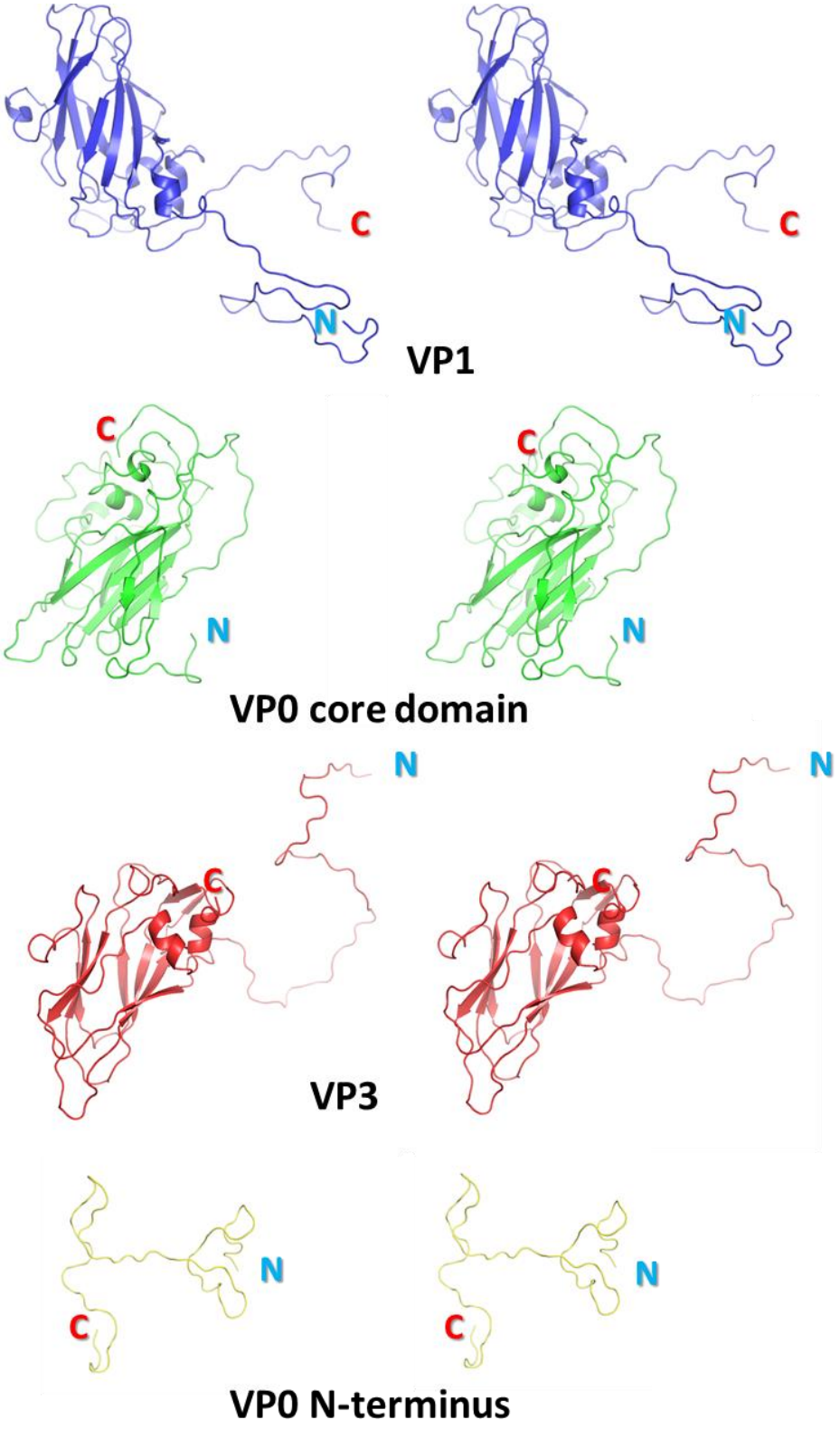

Fig. 4.5 Stereo views of AiV capsid protein structures (VP1, VP0 and VP3). VP1,

VP0 core domain, VP3 and VP0 N-terminal region are drawn in blue, green, red and yellow respectively with N and C terminal labeled.

The AiV structure posseses pores in the capsid, at the 2-fold axes, similar to those seen in FMDV which are penetrable by ions such as Cs+ [151]. A structure-based phylogenetic tree constructed from the biological protomers of picornaviruses and picorna-like insect viruses indicates that AiV lies almost equidistant from the *Entero, Cardio, Aphtho,* and *Hepato* genera, being slightly closer to the *Entero* and *Cardio* (Fig. 4.6). The external surface of AiV lacks the marked protrusion from the icosahedral 5-fold axes of Ljungan virus (LV), and is less angular than that of hepatitis A Virus (HAV) (Fig. 4.6). Foot-and-mouth-disease virus (FMDV) has short surface loops, producing a rather smooth surface. In contrast, the loops at the 5-fold and 3-fold axes in AiV are slightly longer and raised, giving the virus "cooling tower" structures around the 5-fold axes (Fig. 4.6). AiV possesses some surface depressions in the region of the "canyon" and "pit", which form the site of receptor binding in many picornaviruses [20] (Fig. 4.6). Compared to HAV, the VP1 BC loop of Aichi is extended to build the north wall of the canyon while the movement of the VP1 GH loop (part of the south wall) narrows down the front part of the depression. In spite of the reduction in the VP2 EF loop, a long insertion in VP2 CD loop forms the back part of the depression, but is broader and flatter (Fig. 4.6 and Fig. 4.7). AiV does not contain the hydrophobic pocket seen in the VP1 protein of eneroviruses where

expulsion of a lipidic pocket factor is a pre-requisite for uncoating [20, 21, 44]. In AiV, the VP1 β-barrel is compressed, the shift of the C strand and the reorganization of the CD loop directly block the entrance to the pocket and the remaining space is filled by large side chains (Fig. 4.6). In addition, the long VP4 counterpart (VP0 N terminus) in AiV folds back again and again, in a “bow and arrow” like shape and has a greater number of interactions with other protomers in a pentamer than within its own protomer (Fig. 4.6).

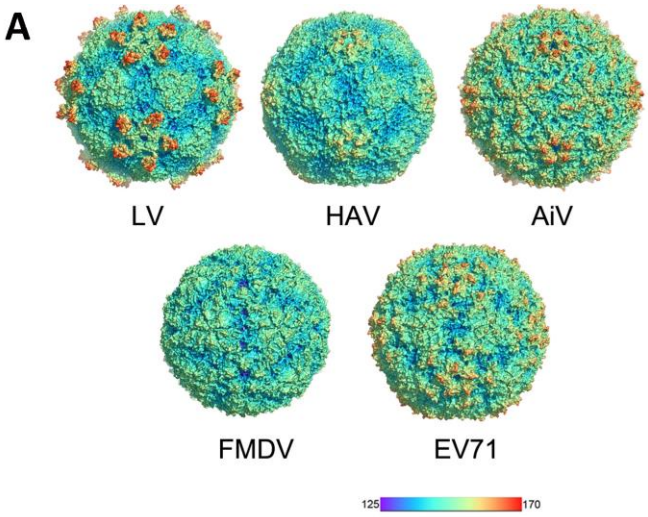
A
LV
HAV
AiV
FMDV
EV71
125
170

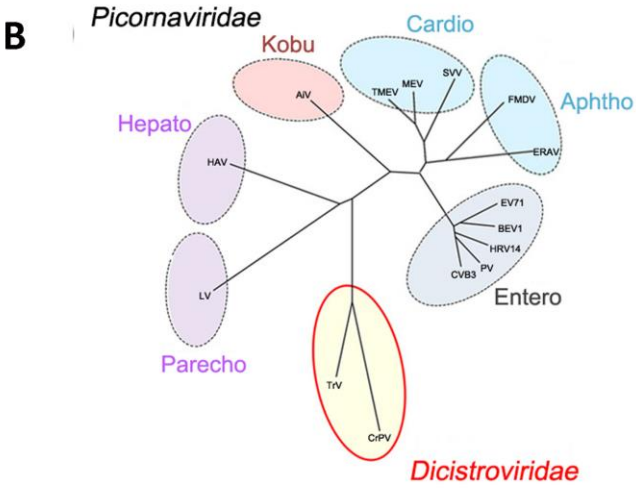
B
Picornaviridae
Kobu
Cardio
Aphtho
Hepato
Parecho
Entero
Dicistroviridae
AiV
TMEV
MEV
SVV
FMDV
ERAV
HAV
EV71
BEV1
HRV14
CVB3
PV
LV
TrV
CrPV

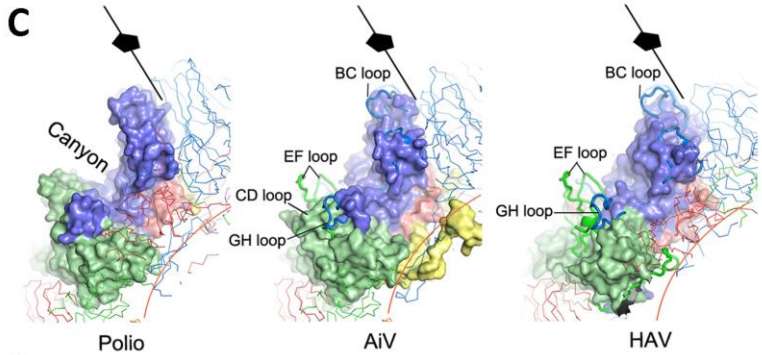
C
Canyon
BC loop
EF loop
CD loop
GH loop
Polio
AiV
HAV

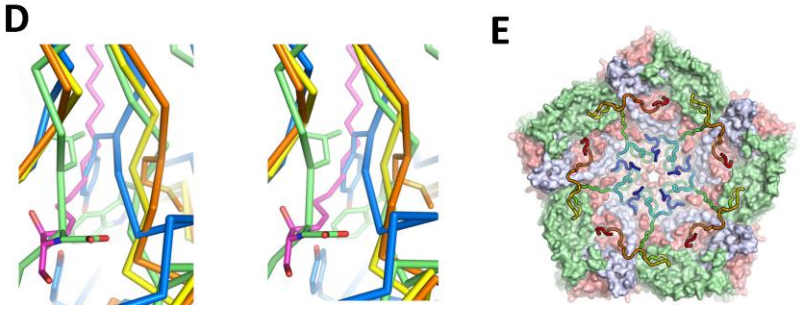
D
E

Fig. 4.6 Overall structures, phylogeny and structural features. (A) Comparison of capsids from AiV with LV, HAV, FMDV and EV71. The capsids are colored by radius from blue to red according to the scale bar shown. (B) Structure-based evolutionary relationship among viruses from *Picornaviridae* (circled by dashed lines) and *Dicistroviridae* (circled by solid line). (C) Surface of the biological protomer of AiV, poliovirus and HAV. The five-fold axes are indicated by regular pentagons. Loops forming the canyon walls in poliovirus are drawn thicker, the CD loop constituting the “pit” in AiV is also labeled. (D) Close up view of pocket. C strand (left) and H strand for EV71 (orange, pocket factor magenta), HRV14 (yellow), FMDV (blue) and AiV (green) are presented in ribbon format. Bulky side chains shown as sticks occlude the AiV and FMDV pockets. (E) The unique structure of the VP0 N-terminus (VP4 counterpart) in AiV is shown in cartoon representation with N-terminal and C-terminal regions colored in blue and red respectively, whilst the remaining structure is rendered as a surface.

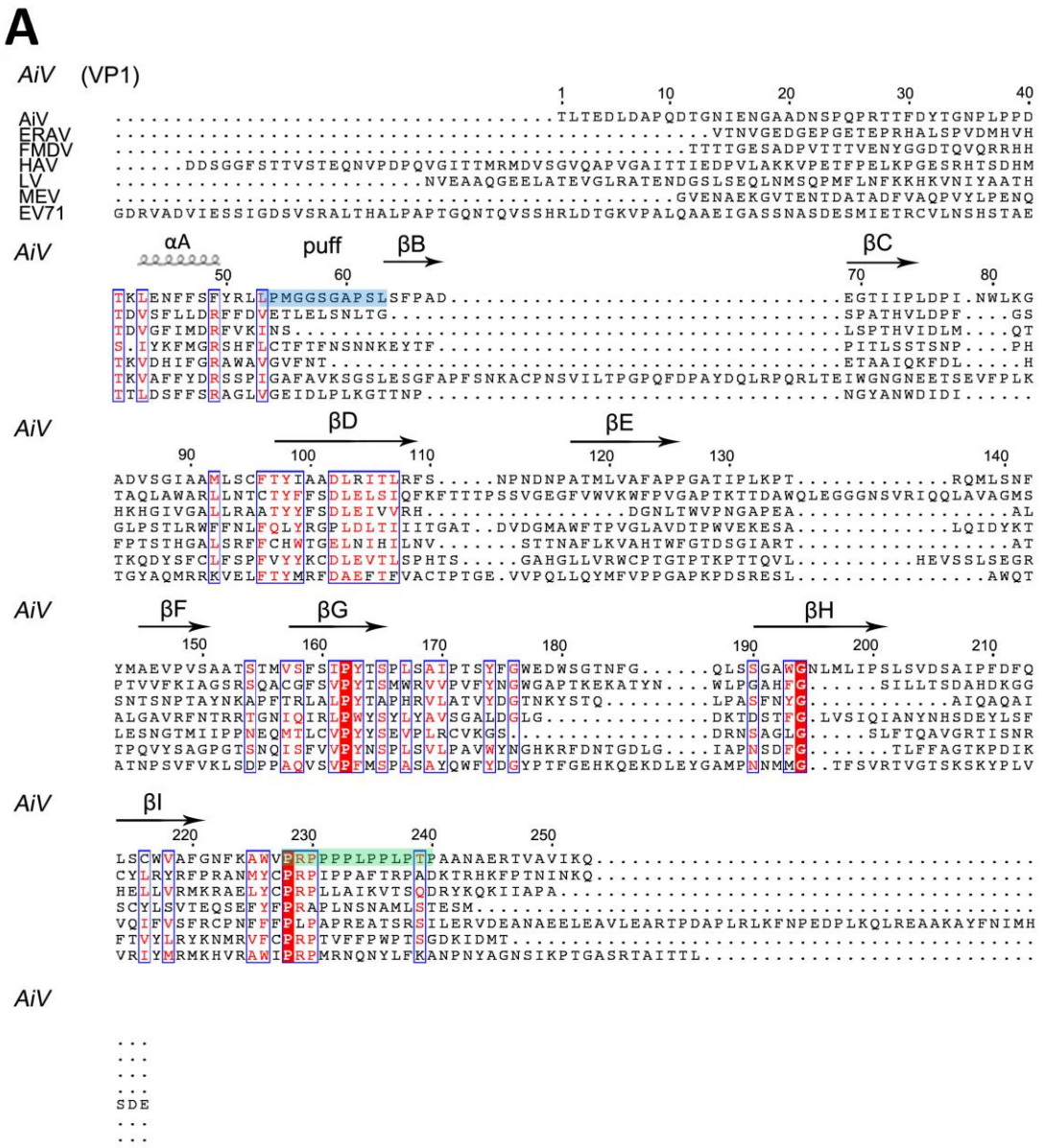
A
AiV (VP1)
AiV
ERAV
FMDV
HAV
LV
MEV
EV71
αA
puff
βB
βC
βD
βE
βF
βG
βH
βI

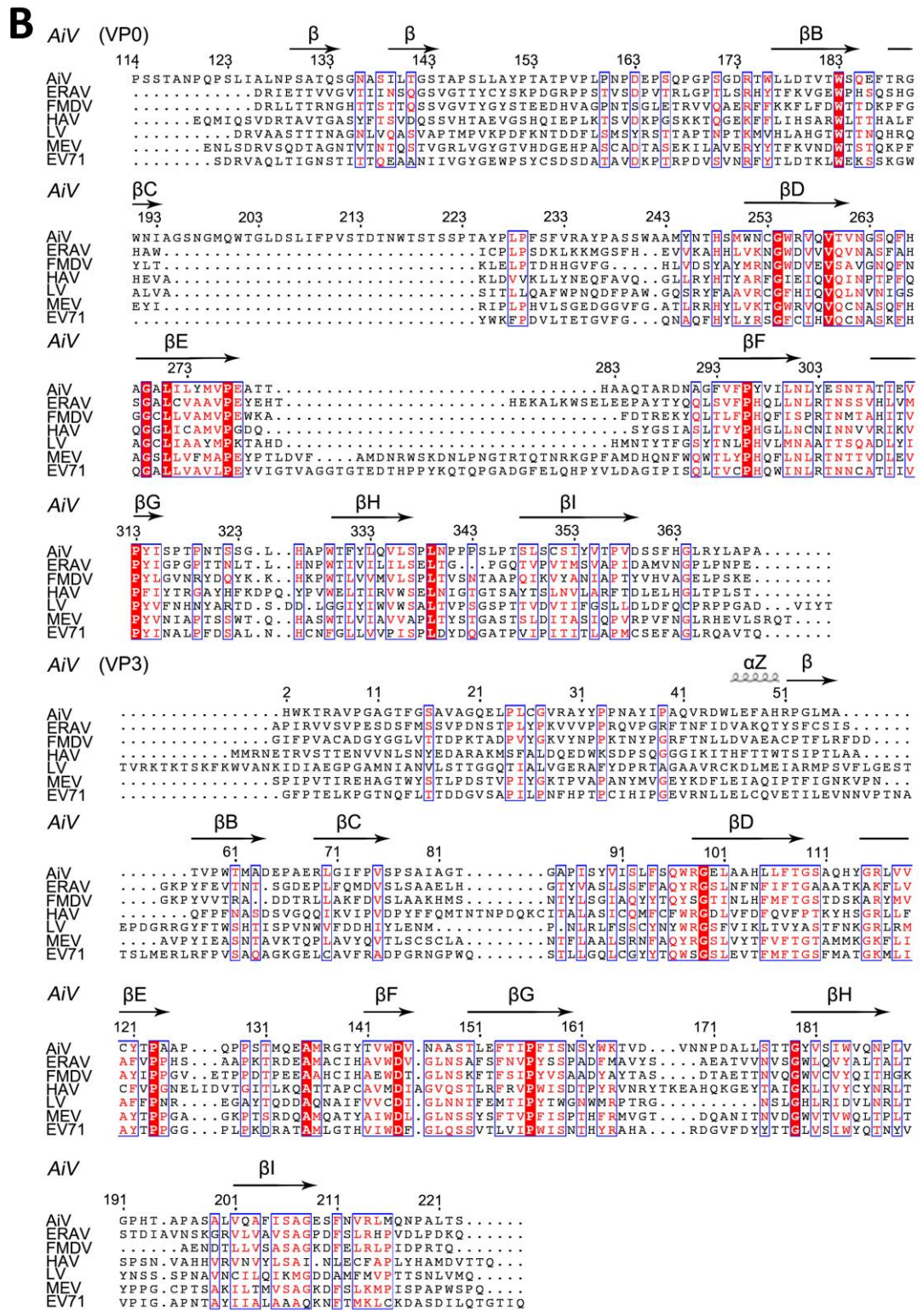

Fig. 4.7 Multi-sequences alignment of AiV with other picornaviruses. Espript [100] representation of a structure-based sequence alignment of VP1, VP0 and VP3

of the Aichi particle with representative piconaviruses, including equine rhinitis A virus (ERAV), foot-and-mouth disease virus (FMDV O serotype), hepatitis A virus (HAV), Ljungan virus (LV), Mengo virus (MEV) and human enterovirus 71 (EV71) (PDB codes: 2WFF [19], 1ZBA [151], 4QPI [25], 3JB4 [29], 2MEV [152] and 3VBH [20] respectively). The secondary structural elements for AiV are shown, also above the sequences are symbols which show features described in the text.

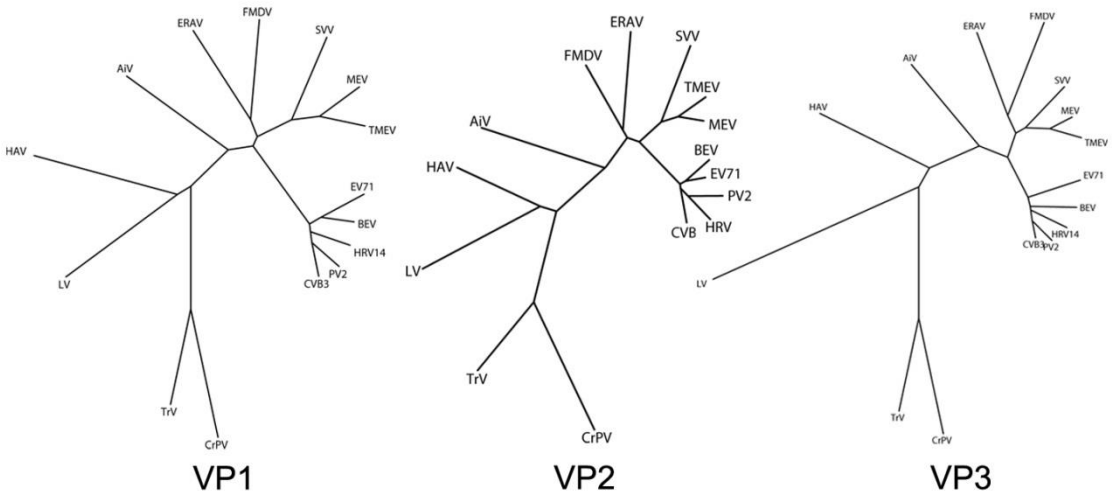

Fig. 4.8 Structure-based evolutionary trees calculated from individual capsid protein. Structure-based evolutionary relationship among viruses from *Picornaviridae* and *Dicistroviridae*: CVB3, coxsackievirus B3; PV1, poliovirus type 1; HRV14, human rhinovirus 14; BEV1, bovine enterovirus type 1; EV71, EV-A71; TMEV, Theilers virus; MEV, Mengo virus; SVV, Seneca valley virus; FMDV, foot-and-mouth disease virus; ERAV, equine rhinitis A virus; HAV, hepatitis A virus; AiV, Aichi virus; TrV, triatoma virus; CrPV, cricket paralysis virus.

4.5 Structural comparisons with the AiV capsids and the capsids of other picornaviruses

Overall AiV VP1 most closely resembles that from aphthoviruses and cardioviruses than from other picornaviruses with an r.m.s. deviation of ~2.8-3.0 Å for ~80-85% matched Cαs for these five viruses based on a comparison of 15 known structures (Fig. 4.8). AiV VP1 has a unique 'puff" structure connecting the αA helix and βB strand, which is absent in other picornaviruses (Fig. 4.7 and Fig. 4.9). The overall fold of AiV VP3 is similar to other picornaviruses, but it does not bear the N-terminal A/LRM (arginine/lysine-rich motif), which mediates RNA attachment in parechoviruses [29] (see Chapter 3.8 for a description of this structure in LV). This might reflect a different mechanism of genome encapsidation for AiV.

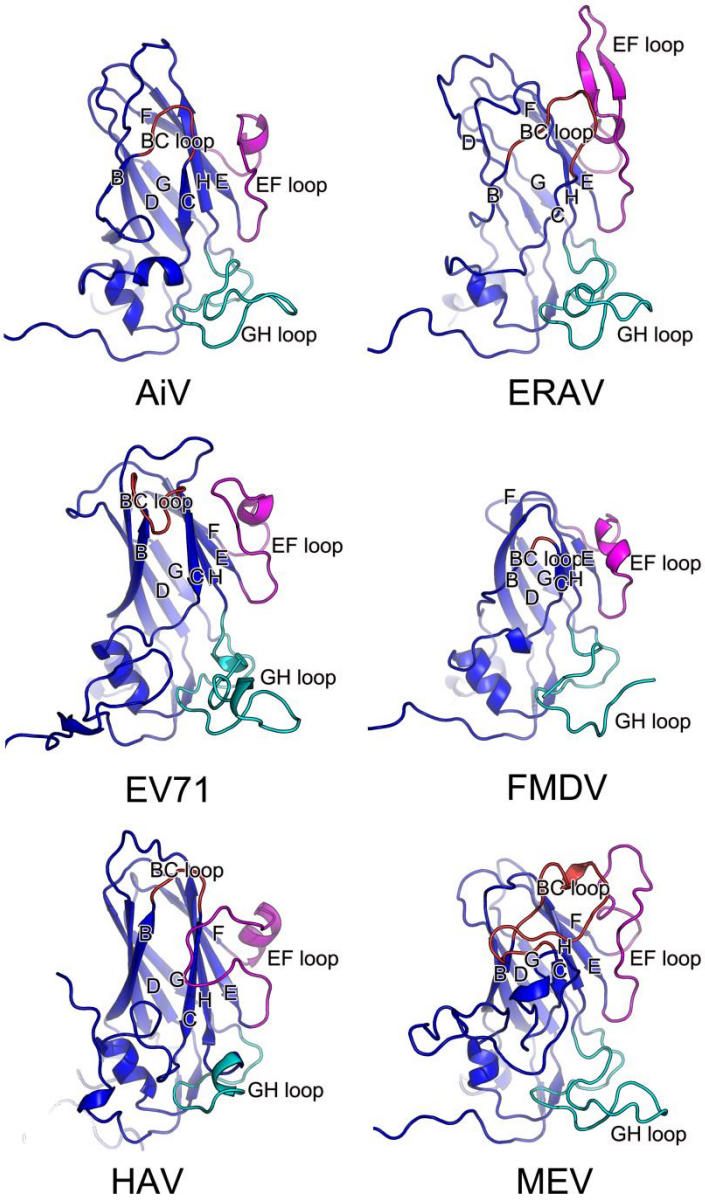

Fig. 4.9 Structural comparisons of the VP1s from AiV, ERAV, EV71, FMDV, HAV and MEV. The BC, EF and GH loops are highlighted in red, magenta and cyan respectively.

At 370 residues AiV VP0 is the longest of known picornaviruses, and there is no reported cleavage of VP0 into VP2 and VP4 in the genus *kobuvirus*. Sequence and structural comparisons show that the VP0 core domain (VP2 counterpart) is most similar to VP2 in Mengovirus (RMSD for 83% of Cαs is 1.9 Å) (Fig. 4.8), however the VP0 N-terminal domain (VP4 counterpart) exhibits little similarity to other VP4s (Fig. 4.10). AiV does not possess the VP2 N-terminal domain swap configuration observed in HAV, LV and insect picorna-like viruses across the 2-fold axis, where it enhances interactions with the neighboring pentamers [25, 29]. An approximately 30 residue insertion in the CD loop of the AiV VP0 core domain, is strikingly exposed on the external surface, forming the south wall of the depression, leaving an extremely short βC strand (Fig. 4.6), this CD loop might play a role in receptor binding and is predicted to be a major antigenic epitope. The VP0 N-terminal domain (predicted 113 residues in length based on the structural alignment of VP0 in AiV against VP2 in other picornaviruses) is 30-50 residues longer than other VP4s.

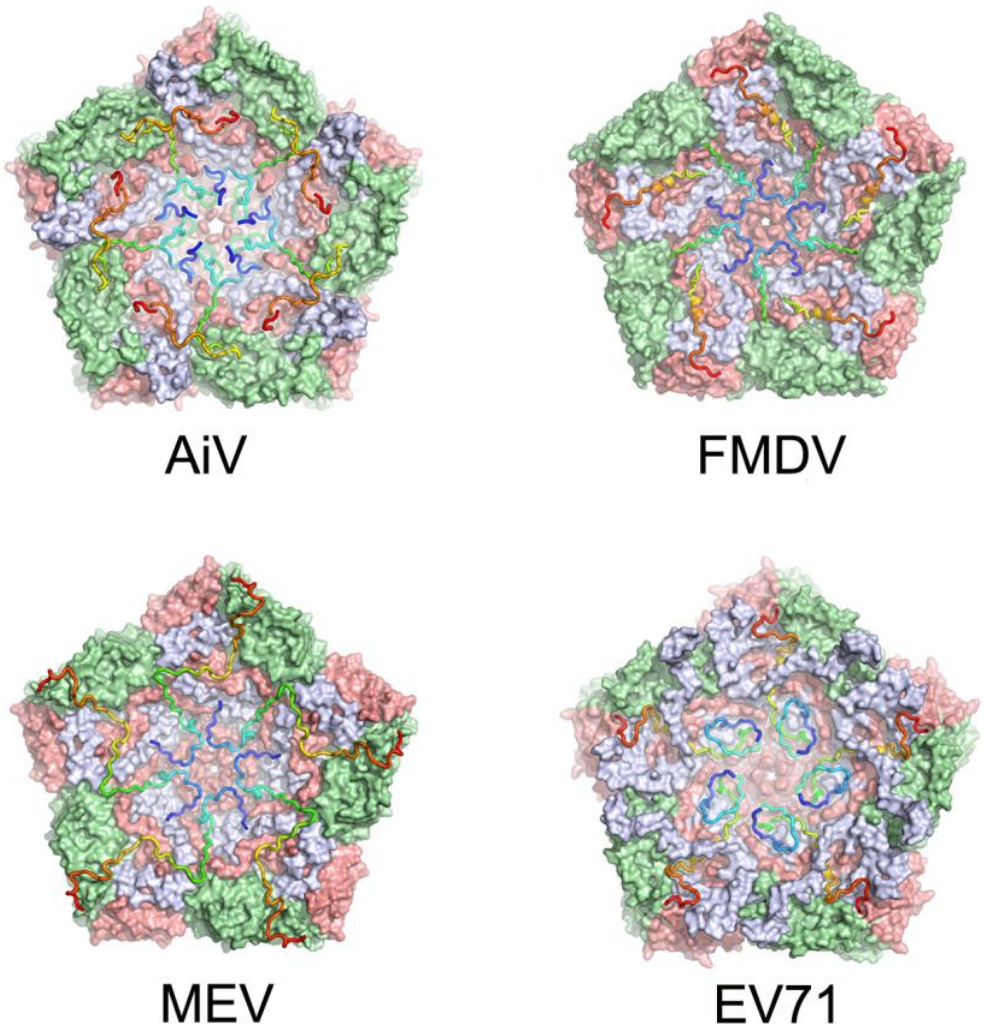

Fig. 4.10 Structural comparisons of VP4 or VP4 counterpart from VP0 for 4 genera of the *Picornaviridae* family. Residues of VP4 or the VP4 counterpart are shown in rainbow colored cartoon representations with N-terminal region and C-terminal colored in blue and red respectively, whilst the remaining structure is

rendered as a surface. A pentamer of icosahedral protomeric units is shown.

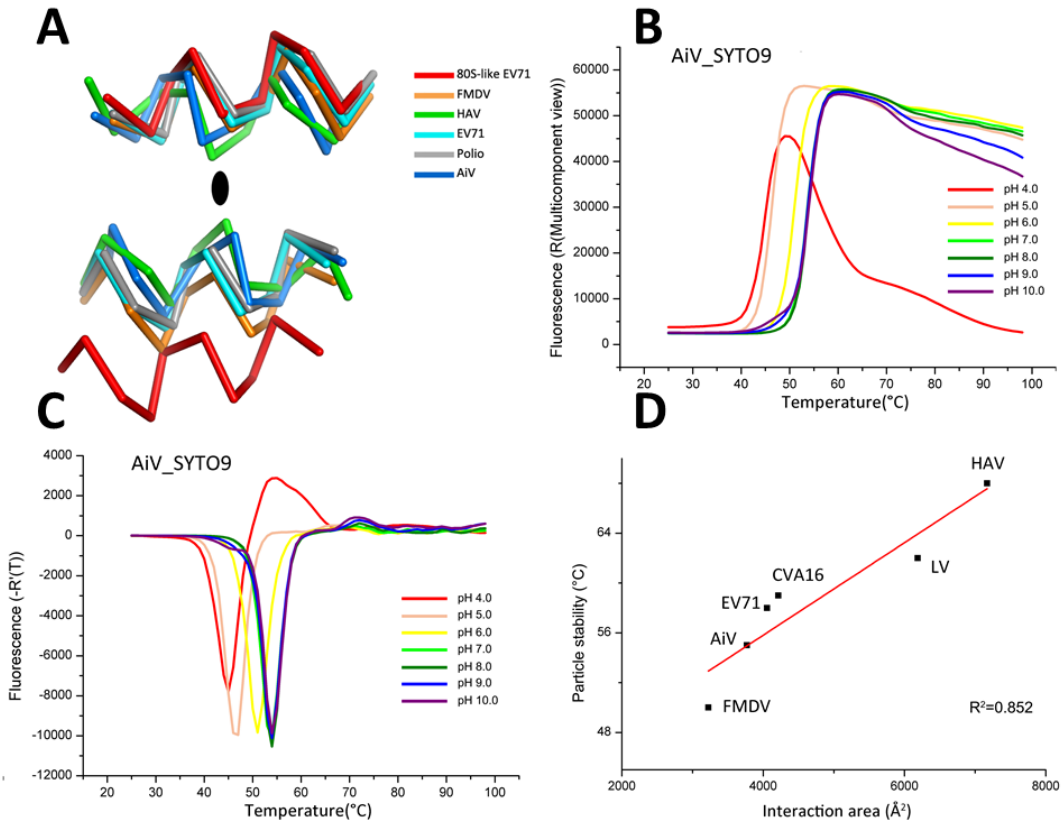

Fig. 4.11 Particle stability and the correlation between particle stability and interaction areas. (A) The separation of VP2 α-helices at the icosahedral two fold of HAV, AiV, EV71, Polio, FMDV and 80S-like EV71. (B, C) The thermal stability of AiV. (B) The raw fluorescence traces of AiV incubated with SYTO9; their first derivatives are shown in (C). The color scheme is red (pH 4.0), orange (pH 5.0), yellow (pH 6.0), green (pH 7.0), sky blue (pH 8.0), blue (pH 9.0) and purple (pH 9.5). (D) Correlation plot of interaction areas between pentamers versus experimental

particle stability. Particle stability for representative viruses was characterized experimentally at pH 7.0.

4.6 Structural elements determining particle stability

Determination of the stability of virus particles is critical to kill viruses properly and to guide vaccine design. The interaction region (VP2 αA helix) adjacent to the icosahedral 2-fold axes, which separates during the initial stages of enterovirus uncoating [21], plays a key role in the stability of particles [58]. The separation of the VP2 αA helix at the icosahedral 2-fold of AiV is 5.3 Å, shorter than average (HAV-3.8 Å, EV71-7.3 Å, polio-7.6 Å and FMDV-8.2 Å) (Fig. 4.11), presenting a relatively tight packing. However, the stability of AiV across the pH range from 4.0 to 9.5 was determined by scanning fluorimetry assay PaSTRy [121] using the dye SYTO9 to detect RNA exposure [153]. This revealed that AiV displayed the stability of a typical enterovirus and became unstable at lower pH (Fig. 4.10). But unlike FMDV, even under pH 4, AiV does not dissociate into pentamers at room temperature, revealing a different uncoating mode. To correlate the particle stability with the structure, we systematically analyzed the interactions between any one subunit and its environment within the protomer, within the pentamer and between pentamers by PISA [154] (Table. 4.3). We found the interactions between pentamers determine the particle stability with a compelling correlation R^2 of 0.852 (Fig. 4.11).

Table. 4.3 Extent of interactions between any one subunit and its environment within the promoter, within the pentamer and between pentamers (AiV, HAV, FMDV, EV71, LV and CVA16)

Within a protomer

Interface(Å^2)	AiV	HAV	FMDV	EV71	LV	CVA16
VP1	3,581	5,158	3,198	7,781	4,404	7,560
VP2(c)	3,319	2,771	2,406	5,150	2,116	4,283
VP3	2,701	5,175	2,048	6,461	4,608	6,364
VP4(c)	1,791	-----	1,044	2,961	-----	3,013
Total	5,696	6,552	4,348	11,176	5,564	10,610

Between protomers within the pentamer

Interface(Å^2)	AiV	HAV	FMDV	EV71	LV	CVA16
VP1	5,200	4,138	5,173	3,820	3,739	3,682
VP2(c)	1,474	1,395	1,404	1,185	1,675	1,296
VP3	7,424	4,803	7,823	4,261	4,885	4,486
VP4(c)	1,989	-----	877	580	-----	476
Total	16,087	10,336	15,277	9,846	10,299	9,940

Between pentamers

Interface(Å^2)	AiV	HAV	FMDV	EV71	LV	CVA16
VP1	0	1,006	0	777	286	802
VP2(c)	2,355	5,738	2,059	3,158	5,411	3,186
VP3	1,413	424	1,165	43	488	80
VP4(c)	0	-----	0	77	-----	96
Total	3,768	7,168	3,224	4,055	6,185	4,164

Note: The coordinates of the above six viruses were used to calculate the extent of interactions.

VP2(c)*: VP2 or VP2 counterpart

VP4(c)*: VP4 or VP4 counterpart

"-----" : Can't calculate the interactions due to the disorder of VP4 or VP4 counterpart

4.7 Functional studies on putative receptor-binding sites

Although there are receptors known for many picornaviruses [33, 131], the receptor for AiV remains unknown. Certain picornaviruses possess an arginine-glycine-aspartic acid (RGD) or KGD motif at the C-terminus of VP1 which is involved in integrin recognition [128]. Whilst this is not present in AiV there is instead, a proline-rich fragment with the sequence of P228RPPPPLPPLPTP240 at the same position, presenting an extended poly-L-proline type II (PPII) helix, on the external surface of AiV (Fig. 4.12). As noted AiV has an unusually high proline content and there are two PPII helices in the capsid (residue 50-63 in VP0 and residue 228-240 in VP1). Likely due to their peculiar propensity to be solvent-exposed, PPII helices are frequently involved in protein-protein interactions for signal transduction, antigen recognition, cell-to-cell communication and viral pathogenesis [155, 156]. This PPII helix might serve as a recognition signal for cellular receptor(s) or virulence factors to manipulate the host's cellular machinery. Such a PPII helix is unprecedented in picornaviruses, although they are observed in other viruses. A prototypical example is represented by the HIV-1 Nef, which necessarily functions through protein-protein interaction by its polyproline segment (P69VRPQVPLRP78) for full pathogenicity of the virus [157]. To understand if there might be a role for this structure in cell attachment we investigated if a peptide version of the helix might inhibit infection.

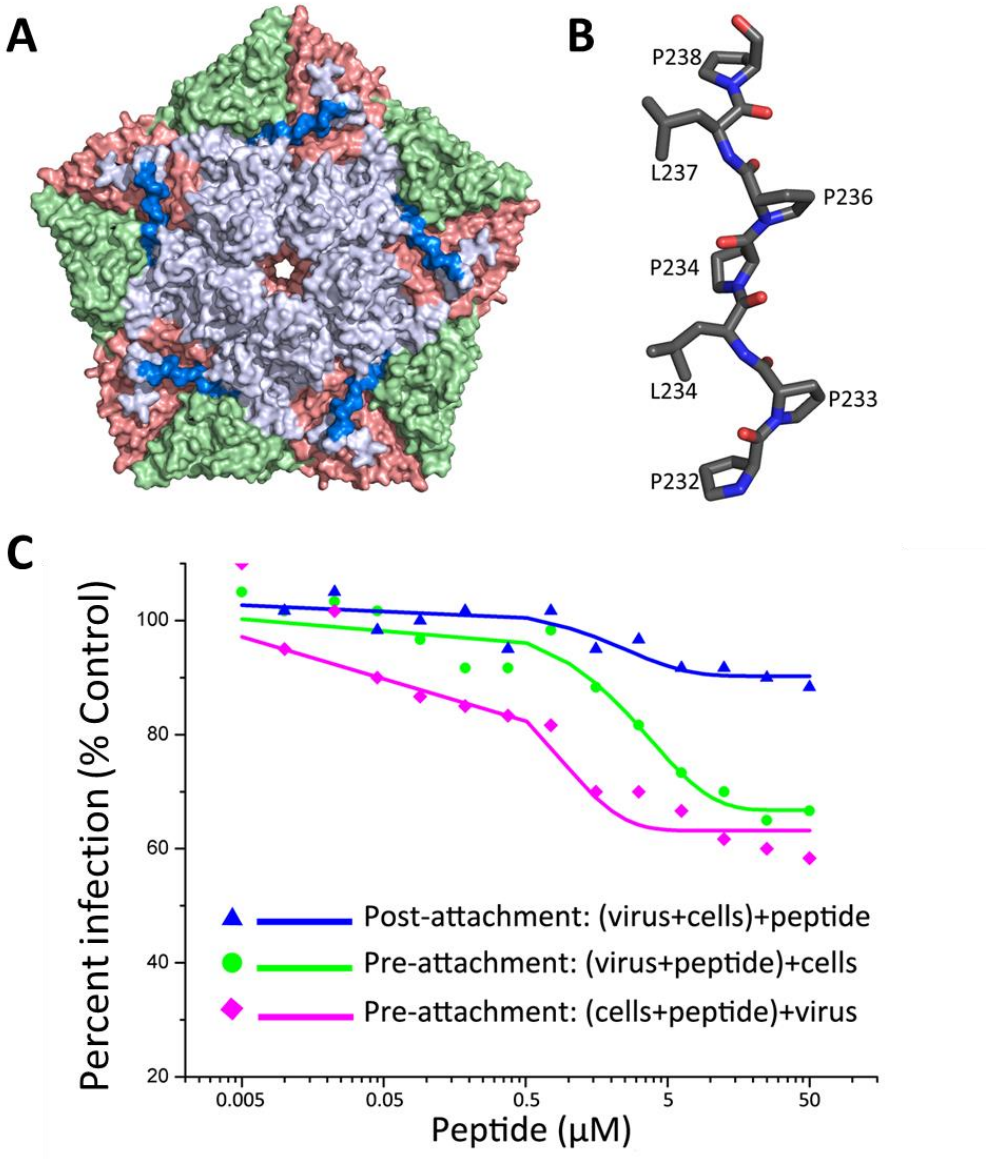

Fig. 4.12 A proline-rich motif, a potential receptor binding site in AiV. (A) Location of proline-rich motifs on the external surface of the AiV pentamer. The proline-rich motifs are highlighted in blue. (B) Side view of a proline-rich motif at the C-terminus of VP1. (C) Peptides of the proline-rich motif in VP1 decrease AiV infection in vero cells at 48 h.

For pre-attachment assays, peptide (P228RPPPPLPPLPTP240) at concentrations ranging from 5 nM to 50 μM was incubated with AiV at a multiplicity of infection (MOI) of 0.5 or with vero cells at 37 ℃ for 1h, then the virus-peptide mixtures were added into vero cells or the cells incubated with peptides were inoculated with AiV at an MOI of 0.5, using AiV without peptides as a control. For the post-attachment assay, vero cells were infected with AiV at MOI of 0.5 at 37 ℃ for 1h and peptide at varying concentrations was subsequently added. Cells exposed to concentrations of peptide ranging from 5 nM to 50 μM alone were used to evaluate the cytotoxicity. Cells were cultured in DMEM supplemented with 1% FBS and grown at 37 ˚C with 5% CO2. At 48 h post infection, cells were observed to evaluate the appearance of CPE. The results (Fig. 4.12) do indeed show a partial inhibition, in particular, pre-attachment of peptides to cells was able to inhibit by nearly 50% infection of Aichi virus, suggesting that this structure is capable of partially competing with the virus.

4.8 Conclusion

In summary, AiV exhibits a number of distinctive features and seems to occupy an evolutionary position between the enteroviruses and other picornaviruses, using an uncoating mechanism yet to be determined but different to that of enteroviruses. Furthermore we suggest that a highly exposed polyproline helix at the C-terminus of

VP1 is a recognition motif for binding to the enteric receptor. This would imply a mode of engagement with the host cell unlike others described for picornaviruses.

Chapter 5
Structural study of coxsackievirus A16 virus like particles

5.1 Introduction to VLPs

VLPs are empty particles consisting of viral capsid proteins but devoid of viral genome, so they are non-infectious. As an alternative choice for potential vaccine candidates VLP vaccines have many advantages being highly immunogenic, noninfectious, and accessible to quality control as well as to scaling-up during production. Hand-foot-and-mouth disease is a serious public health threat to children in Asian-Pacific countries, resulting in millions of cases [158]. EV71 and CVA16 are the two dominant causative agents of this disease that, while usually mild, can cause severe neurological complications, leading to hundreds of deaths [159]. Although inactivated EV71 vaccine has been on the market in China [84], EV71 vaccines do not provide protection against CVA16. A CVA16 vaccine or bivalent EV71/CVA16 vaccine is therefore urgently needed [160].

Both EV71 and CVA16 consist of 60 copies for each of the capsid proteins VP1, 2 and 3 arranged with pseudo T=3 symmetry, whilst their N-terminal extensions and 60 copies of VP4 line the interior. Natural empty particles (without RNA) are often also formed, in which the final RNA mediated coat protein cleavage (between VP4 and VP2) does not happen [76]. The Bac-to-Bac expression system has proved to be useful for the production of VLP vaccines. Co-expression of the P1 (coding for the viral capsid proteins) and the 3CD (coding the viral protease and polymerase) genes in insect cells can generate certain VLPs with good yield [79]. Previous studies

showed that both EV71 and CVA16 VLPs can elicit potent immune responses and are able to protect immunized mice against lethal challenges with EV71 or CVA16 virus [161-163]. How VLP vaccines mimic their viral counterparts structurally and how the neutralizing epitopes are preserved on the surface of VLPs are issues of considerable interest for the development of effective vaccines. Structural comparisons and immunogenic analysis between the authentic virions and the recombinant VLPs need to be explored to consider VLPs as good vaccine candidates.

5.2 Molecular design and CVA16 VLP preparation

A modified pFastBac Dual vector (Invitrogen) containing P1 and 3CD genes of CAV16 (09-7 strain) under the control of the polyhedrin and CMV promoters respectively was used to generate recombinant baculovirus using a Bac-to-Bac baculovirus expression system (Invitrogen) (Fig. 5.1). A suspension culture of Sf9 insect cells was infected with recombinant baculovirus at MOI of 10 and the VLPs were purified by centrifuging to remove cell debris, ultra-filtration, sucrose cushion ultracentrifugation and sucrose density gradient ultracentrifugation (see Chapter 2.1.2 for detailed methods). Fractions containing VLPs were collected, dialyzed against PBS (pH 7.4) and concentrated for crystallization and negative stain electron microscopy (Fig. 5.1).

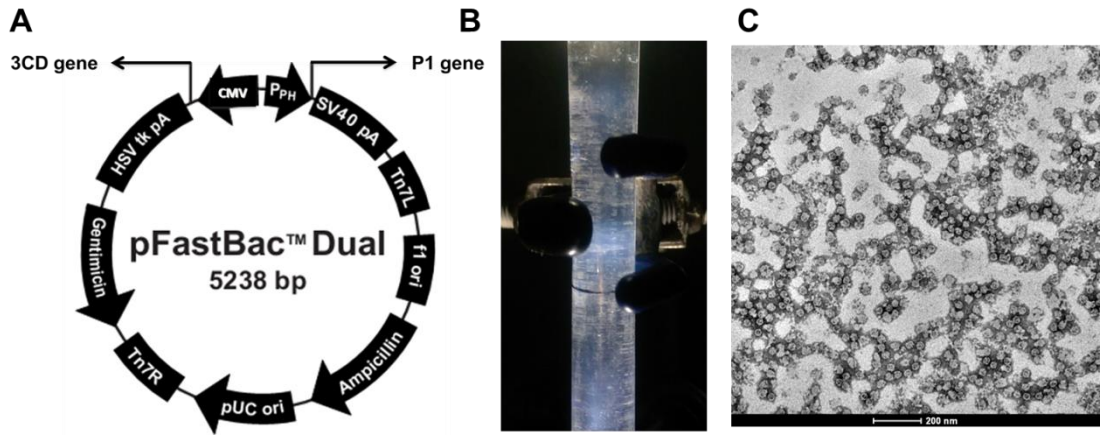

Fig. 5.1 Strategy for expression of CVA16 VLPs (A), purification of CVA16 VLPs with 15%-45% sucrose gradient centrifugation (B) and negative stain EM of purified CVA16 VLPs (C).

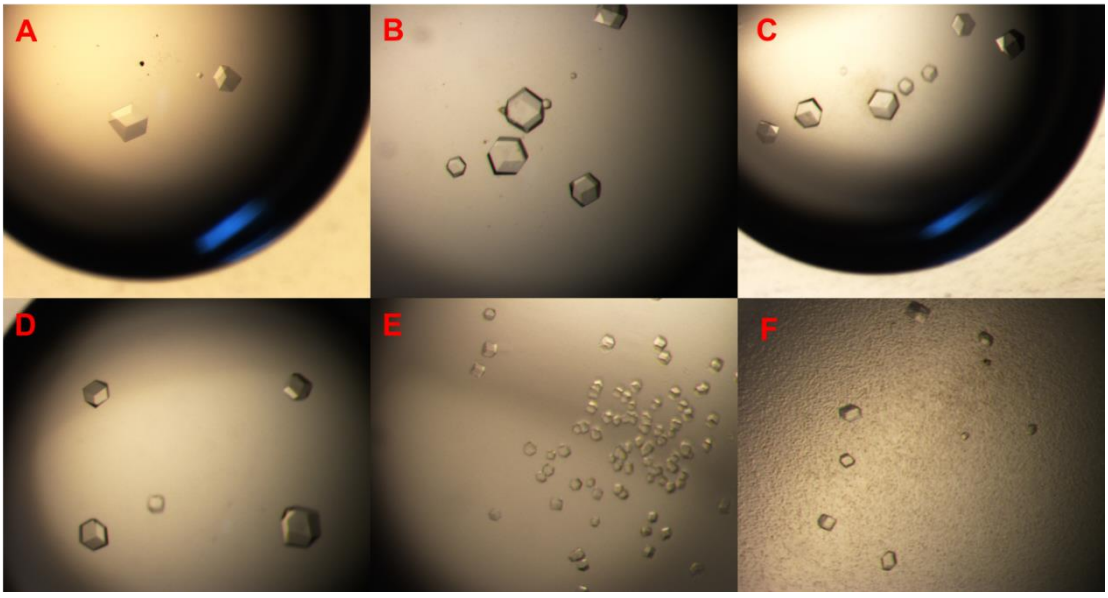

Fig. 5.2 Gallery of crystals of CVA16 VLPs under different conditions. (A) 1.8 M ammonium citrate dibasic, 0.1 M sodium acetate trihydrate (pH 4.8), (B) 1.0 M ammonium citrate dibasic, 0.1 M sodium acetate trihydrate (pH 4.7), (C) 3.2 M sodium chloride, 0.1 M Tris (pH 8.0), (D) 3.2 M sodium chloride, 0.1M sodium

acetate trihydrate (pH 4.4), (E) 0.7 M sodium citrate tribasic dehydrate, 0.1 M BIS-TRIS propane (pH 7.6), (F) 2.0 M sodium formate, 0.1 M BIS-TRIS propane (pH 7.3).

5.3 Crystallization, X-ray data collection and structure determination

Highly purified CVA16 VLPs were concentrated to ~3.5 mg/ml for crystallization. A number of cubic crystals emerged in many conditions with the SaltRx screen kit (Hampton Research) using the hanging-drop vapour diffusion method (Fig.5.2). Crystals used for data collection were grown at 16 ℃ under conditions of 1.8 M ammonium citrate dibasic, 0.1 M sodium acetate trihydrate (pH 5.0). Diffraction data for CVA16 VLPs were collected at 100 K at beam line BL41 of the Spring 8 synchrotron in Japan. Diffraction images of 0.1° oscillation were recorded on a Pilatus6M detector using a beam-size of 0.05×0.05 mm2. Crystals were soaked in a solution containing 80% (v/v) reservoir solution and 20% (v/v) glycerol prior to flash-cooling with liquid nitrogen. Crystals of CVA16 VLPs diffracted to 2.5 Å (Fig. 5.3), belonging to the space group $P4_232$ with unit cell dimensions of a=b=c=347 Å. Data were analysed using HKL2000 [87]. The particle is centred at the origin and there is a pentamer in the crystallographic asymmetric unit (5-fold NCS). The structure was determined using the molecular replacement method with the coordinates for mature EV71 (PDB code: 3VBH [20]) as a search model. Rigid-body

refinement followed by cyclic positional, simulated annealing and B-factor refinement used strict NCS constraints with CNS [164]. The model was rebuilt with COOT [96]. Data collection and refinement statistics are shown in Table. 5.1. Ramachandran plot for the refined CVA16 VLP model is shown in Fig. 5.4.

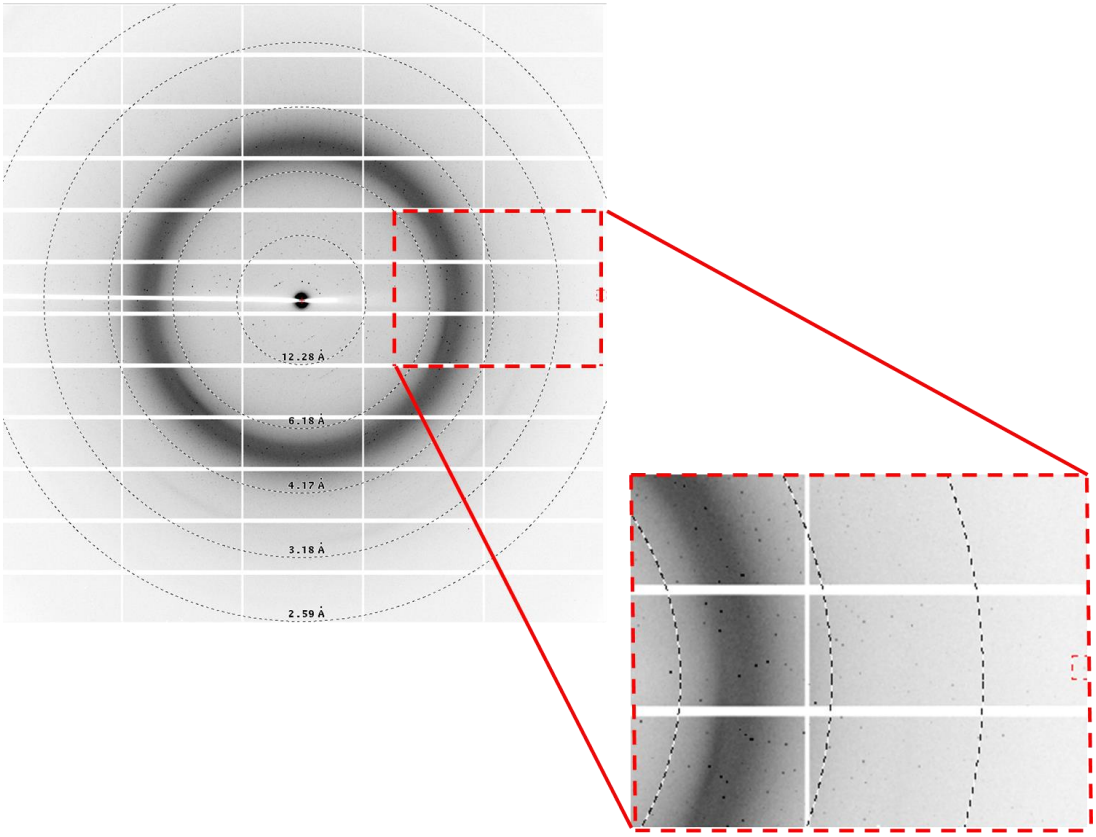

Fig. 5.3 Diffraction pattern from CVA16 VLP crystals

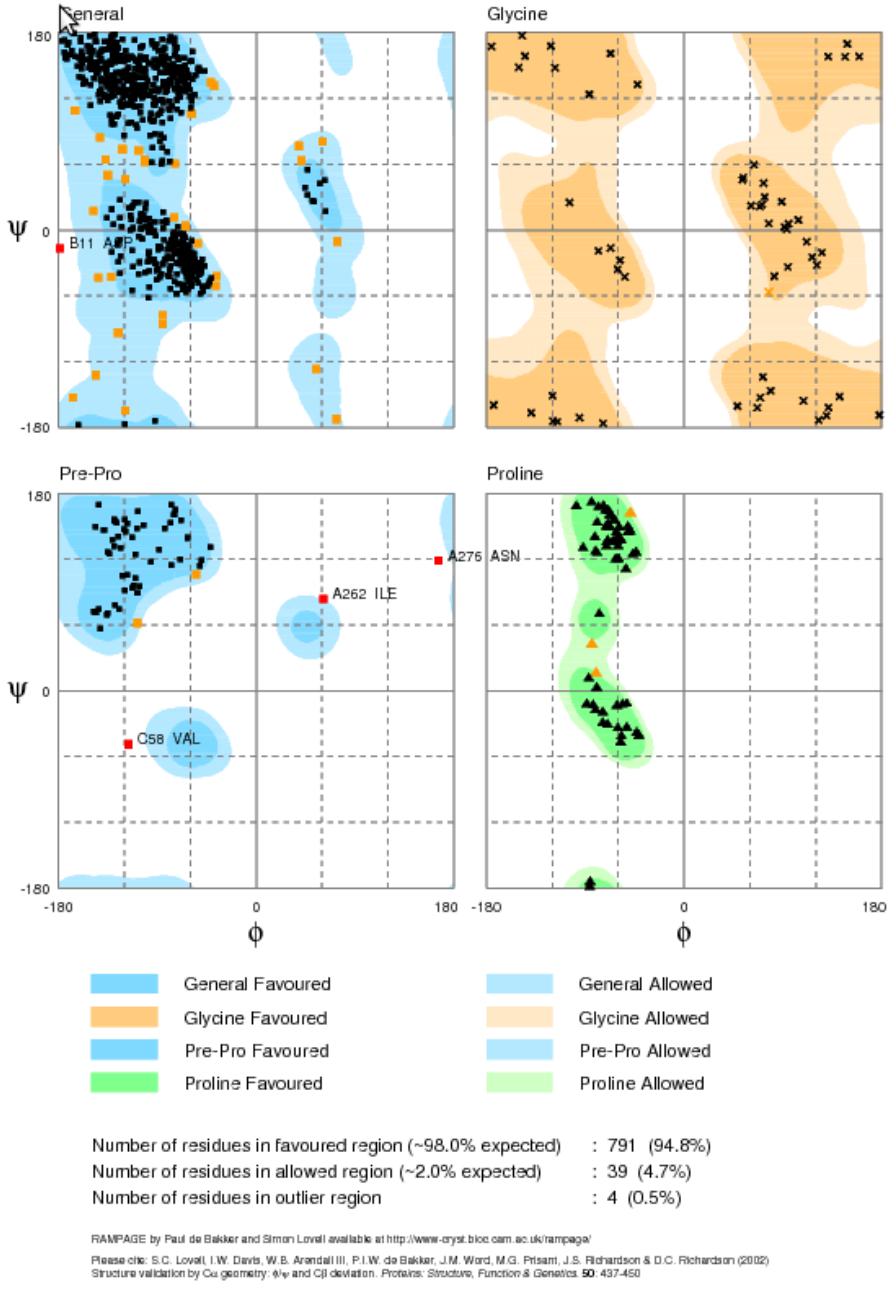

Fig. 5.4 Ramachandran plot for the refined CVA16 VLP model (a protomer)

Table. 5.1 Data collection and refinement statistics

Data collection	
Data set	VLP
No. of crystals (positions)	1
Space group	$P4_232$
Cell dimensions (Å)	a=b=c=347.9
Resolution (Å)	50.0–2.50 (2.59–2.50)
Unique reflections	244135(24125)
Rmerge	0.217
I / σI	11.3(4.1)
Completeness (%)	100 (100)
Redundancy	12.7(10.2)
Refinement	
Resolution (Å)	50.0 – 2.50
No. reflections	244027
Rwork /Rfree*	0.176/0.184
No. atoms	6492
Average B-factors ($Å^2$)	37
R.m.s. deviations	
Bond lengths (Å)	0.013
Bond angles (℃)	1.7

Values in parentheses are for the highest-resolution shell.

* Note that the Rfree is of limited significance owing to the considerable non-crystallographic symmetry.

5.4 Structural comparisons of CVA16 VLPs with native CVA16 virions

The CVA16 VLP is self-assembled from VP0, VP1 and VP3. This particle is unexpanded and in the native antigenic state, thus the external surface of the VLP is structurally indistinguishable to the mature and empty particles (the rmsd in Cα atoms being 0.4 Å and 0.3 Å respectively) (Fig. 5.5). As expected, the residues lining the inner surface of the particle show more disorder, indeed they seem a little more disordered that in the natural empty particle (Fig. 5.5). Disordered residues include 8-23 and 36-61 of VP1, and 1-13, 22-24, 44-50 and 59-82 of VP0. There is a single residue change between the VLP and the natural particles, Thr240, located in the VP1 HI-loop of the VLPs, (Ile240 in the natural particle), but this does not introduce any significant structural change. The pocket-factor binding site located inside the β barrel of VP1 is fully occupied by a fatty acid acquired from the SF9 insect cells, which differs somewhat from that derived from mammalian cells and is modelled as stearic acid (Fig. 5.5 and Fig. 5.6). Compared to CVA16 mature and empty particles, the smaller head (carboxyl group) of the stearic acid is positioned about 3 Å lower than the hydroxyl oxygen of the sphingosine (Fig. 5.5).

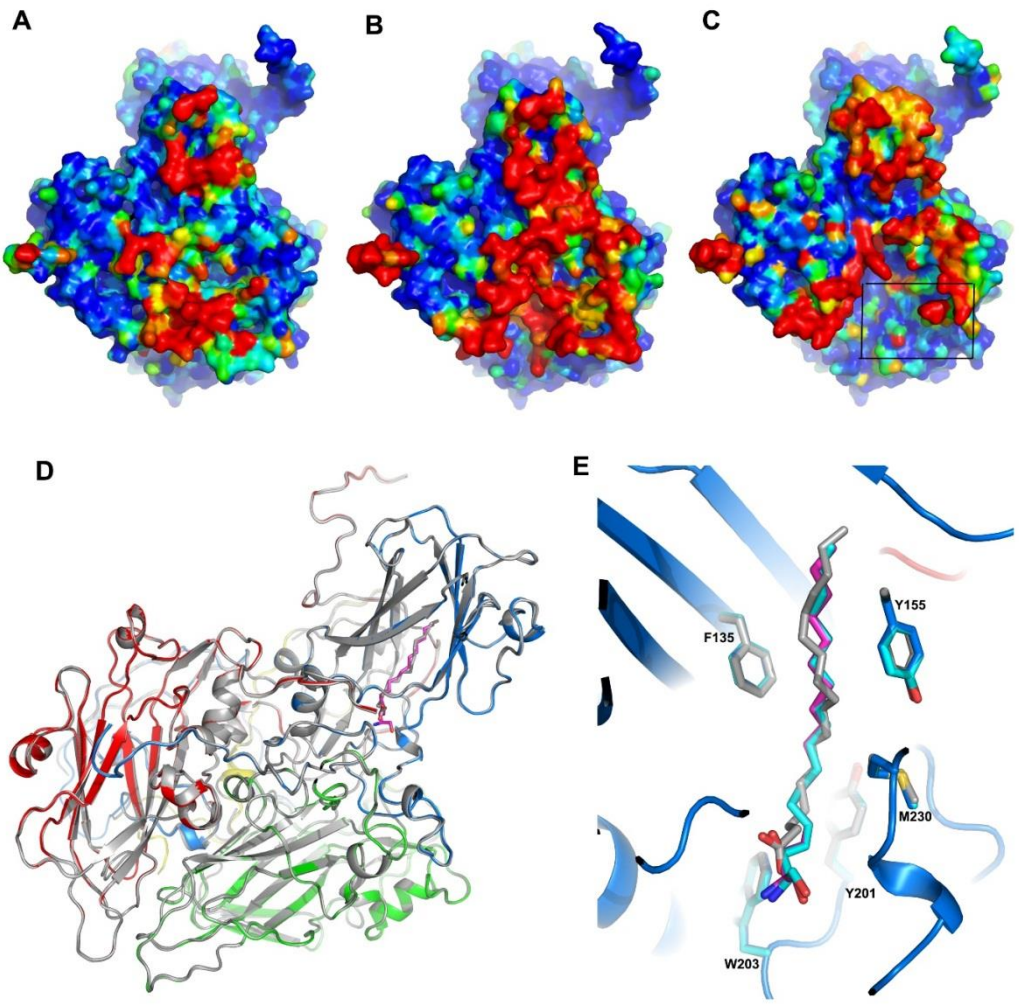

Fig. 5.5 Comparing 3 CVA16 particle structures. (A)-(C) Protomer inner surfaces of full, natural empty and VLP particles, respectively, colored by B-factors showing that the internal structure of the VLP is more flexible and more residues in the VP1 N-terminus and VP4 are disordered (boxed area in C). (D) Ribbon diagram showing superimposed protomers of CVA16 full particle and VLP (gray). (E) Close-up view of the overlaid pocket factor binding sites in the full, natural empty, and VLP particles. For clarity, only the main chains of the full particle are shown as ribbons; the side

chains are colored in blue, cyan, and gray and pocket factors in magenta, cyan, and gray for the full, empty, and VLP particles, respectively.

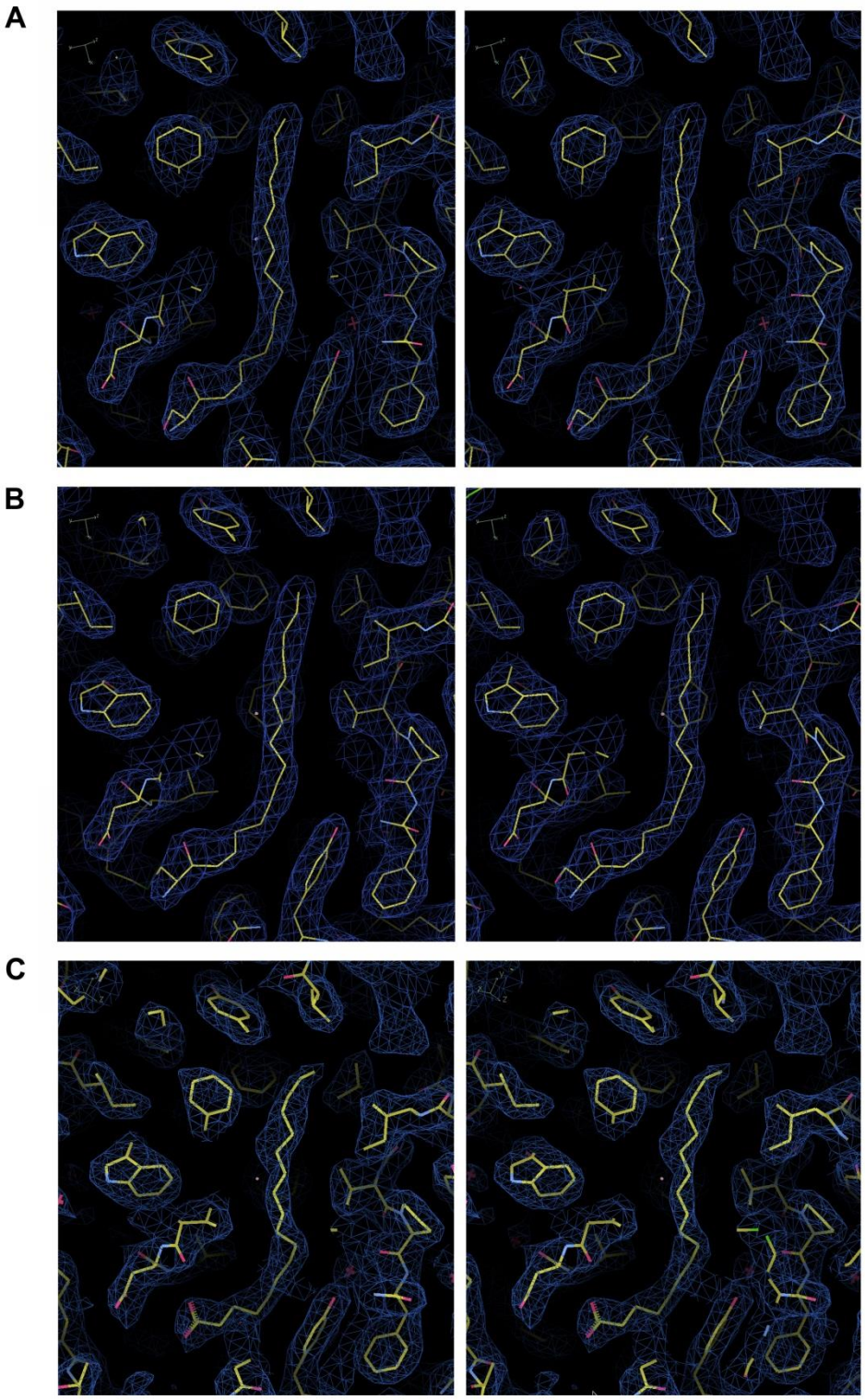

Fig. 5.6 Electron density maps. Stereo diagrams showing electron density in the pocket factor binding region of VP1 in the full (A), natural empty (B) after 60-fold

NCS real space averaging and recombinant virus-like (C) particles after 5-fold NCS real space averaging.

5.5 Antigenic variation analysis between CVA16 and EV71

EV71 vaccination does not induce cross protection against CVA16 [84, 165], *i.e.* the neutralising antibodies either do not bind or are incapable of neutralising CVA16. This presumably arises from structural differences on the outer surface of the two viruses (shape differences are mapped on CVA16 and shown in Fig. 5.7). The surfaces of the two viruses show similar electrostatic features: a positively charged patch around the 5-fold axis and a large negatively charged patch between the pocket entrance and the 2-fold axis (Fig. 5.7). However, the positively charged area around the 5-fold axis in EV71 is smaller and more intense. We have mapped all known epitopes of the two viruses on to their pentamers (Fig. 5.7) [166-171]. These epitopes are concentrated on the walls of the canyon surrounding the proposed SCARB2 binding site (Fig. 5.8) suggesting that neutralisation may arise by steric occlusion of the receptor binding site. However it is also possible that some antibodies might mimic receptor to trigger conformational changes and initiate premature uncoating, indeed the GH-loop of VP1, the sensor-adaptor region implicated in triggering uncoating, together with the EF-loop residues136-150 of VP2 form one antigenic site in EV71 [20] and binding of mAb E18 to this epitope

induces virus expansion and genome release [172]. The VP3 GH-loop in CVA16, which has not been reported to be an epitope in EV71, is close to the VP1 GH-loop of an adjacent protomer and likely to from a single antigenic site (Fig. 5.8). Thus the VP1 GH-loop epitope employs a different structural component to form a distinct antigenic site in the two viruses. Clearly the GH-loop is not the only neutralizing epitope in EV71, a chimeric EV71 VLP in which the VP1 GH-loop is replaced by that of CVA16 can generate protection against both EV71 and CVA16 in mice [80]. It would be interesting to know if a chimeric EV71 VLP containing both VP1 and VP3 GH-loops of CVA16 induces stronger immunogenicity against CVA16.

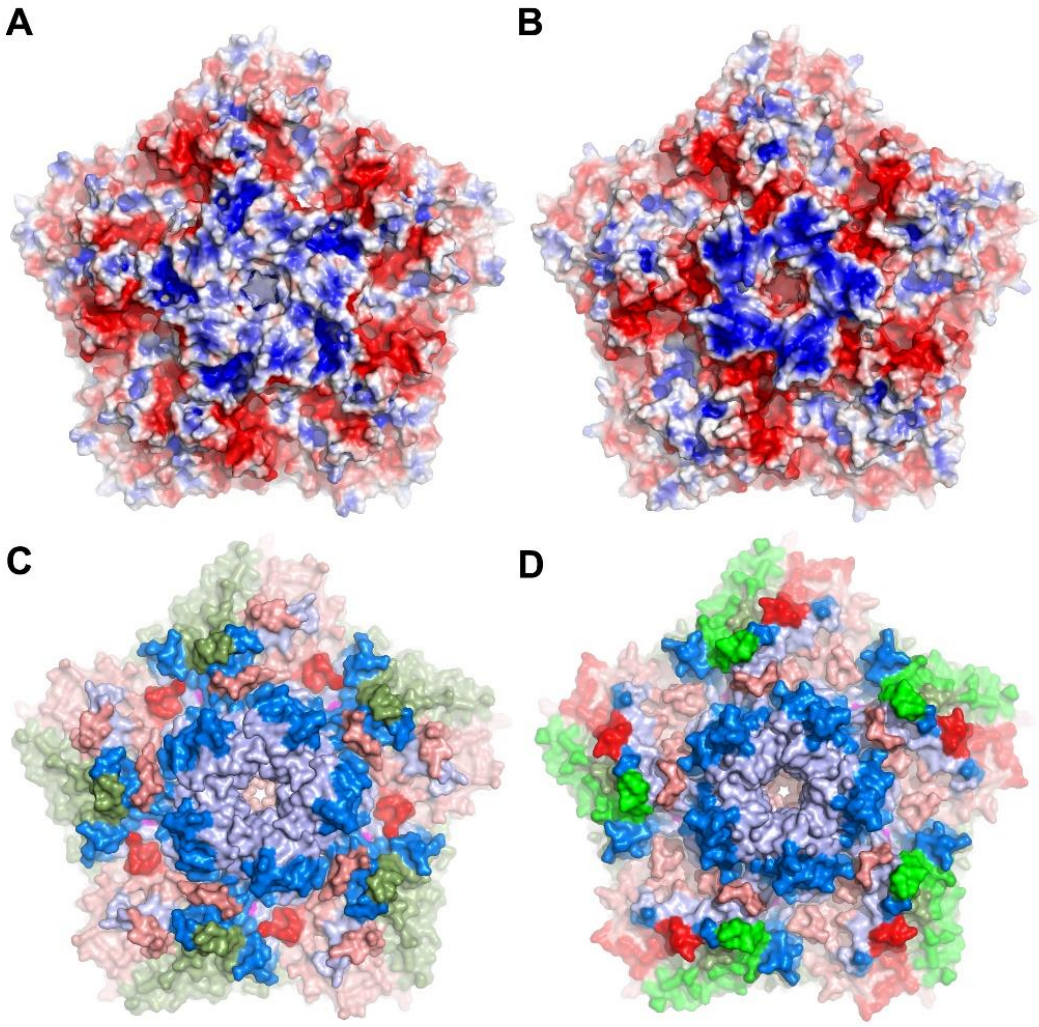

Fig. 5.7 Antigenic sites. Electronstatic surfaces of CAV16 (A) and EV71 (B). Blue and red represent positive charged and negative charged regions respectively. (C) and (D) Epitopes of CAV16 and EV71, respectively. Surfaces of VP1, VP2 and VP3 are in pale blue, green and red, respectively; epitopes are in bright colors.

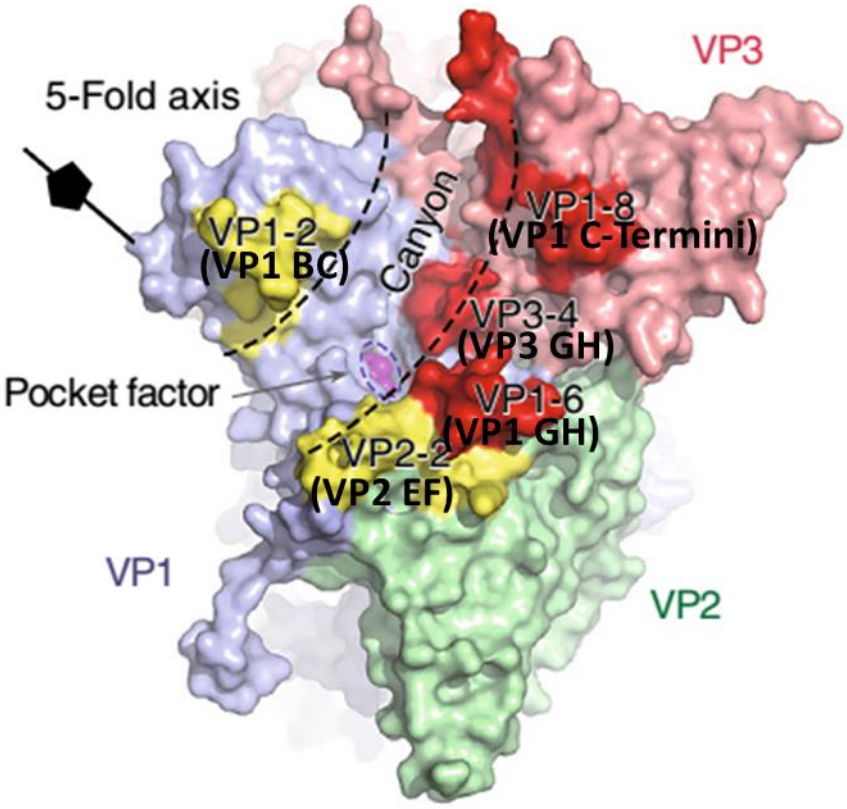

Fig. 5.8 Identification of binding interface between EV71 and SCARB2. Peptides around the "canyon" region of EV71 interact with SCARB2. Surface rendering of one icosahedral asymmetric unit (PDB code: 3VBH) of EV71. Peptides showing stronger interaction with SCARB2 are colored in red and peptides having a weaker affinity for SCARB2 in yellow. A 5-fold axis is shown as a black line and the pocket factor (cyan) indicated by a black arrow. Reproduced from [44].

Table. 5.2 *In vitro* neutralization assays of monoclonal antibodies against EV71 and CVA16. Human hepatitis A virus mAb #7 is used as a negative control.

Antibodies	Neutralization Titers	
	EV71	CVA16
D6	1:512	<1:8
A9	1:2048	<1:8
C33	<1:8	1:128
#7(HAV mAb)	<1:8	<1:8

To explore further why EV71 vaccines do not protect against CVA16 and whether CVA16 virus neutralizing antibodies can cross-neutralize EV71, two mAbs capable of neutralizing EV71, D6 and A9, and one neutralizing mAb against CVA16, C33, were generated (see Chapter 2.2.1 and 2.2.3, Table. 5.2). D6 and A9 have no cross-neutralizing activity against CVA16, and C33 could not protect against EV71 infection. Furthermore D6 and A9 do not bind to CVA16 and C33 does not bind EV71 by ELISA assay (see Chapter 2.2.4) (Fig. 5.9). CVA16 full, empty particles and VLPs exhibit similar binding affinity to C33, as expected since their surface structures are indistinguishable. In-line with this it has been demonstrated that CVA16 VLPs are able to induce neutralizing activity against CVA16 infection in mice.

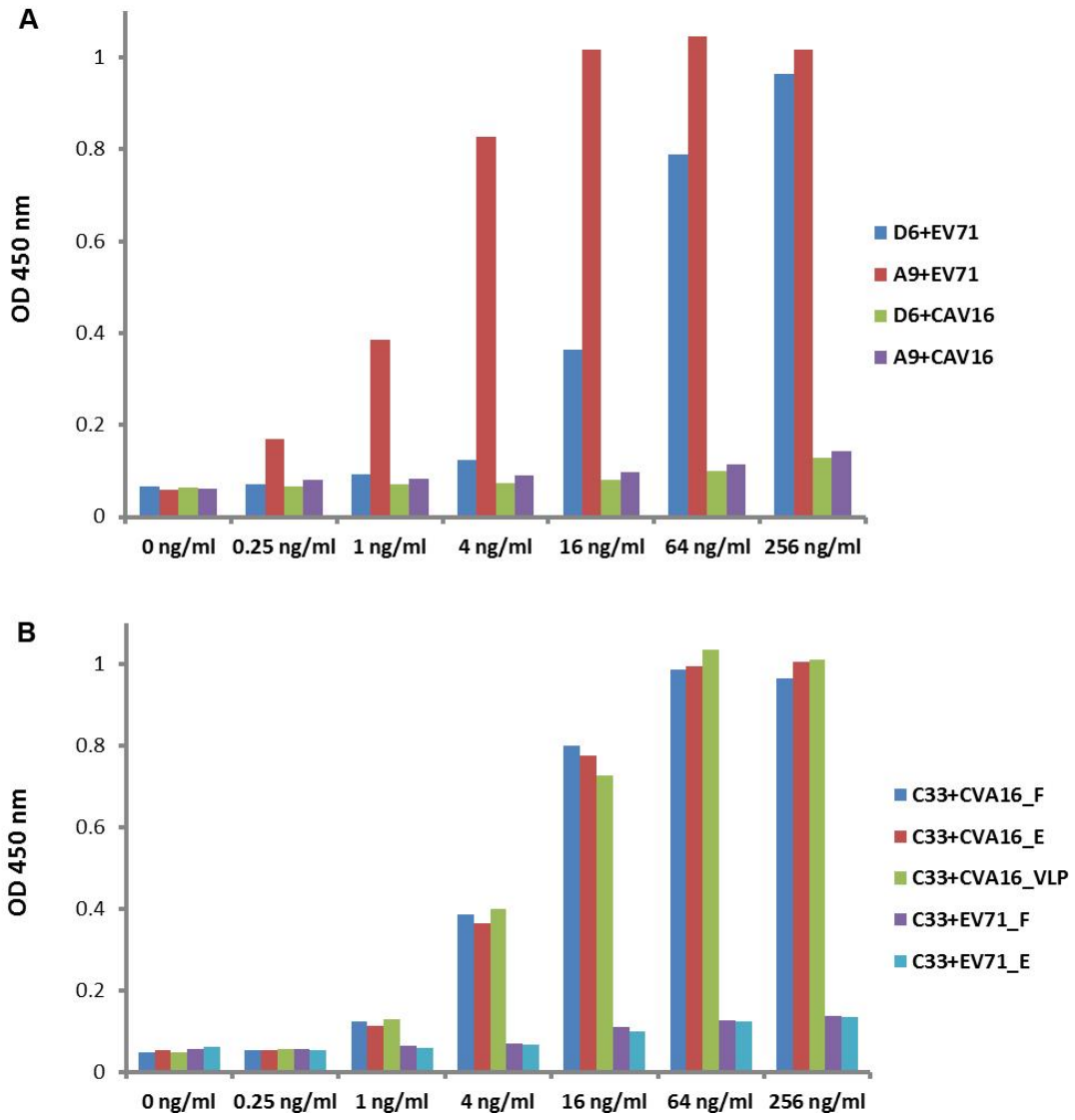

Fig. 5.9 Virus-mAb binding assay. The reactivity of EV71 and CVA16 particles against a panel of three purified neutralizing monoclonal antibodies at indicated dilutions was measured by ELISA. (A) Ability of neutralizing monoclonal antibodies (D6 and A9) to bind EV71 and CVA16 particles. (B) Ability of neutralizing monoclonal antibodies C33 to bind CVA16 full, empty, VLP and EV71 full, empty

5.6 Conclusion

We determined the crystal structure for CVA16 VLPs produced in insect cells. Structural comparisons of CVA16 VLP with CVA16 mature particles and natural empty capsids suggest that the outer surfaces are indistinguishable, interact similarly with monoclonal antibody and are able to elicit strong protection in mice [80]. The substantial overlap of antigenic sites between EV71 and CVA16, which are nonetheless not cross-reactive suggests that a bi-valent stabilised empty particle vaccine might be the best way to produce a broadly effective, safe HFMDV vaccine.

Chapter 6
Structure of a potent neutralizing antibody against hepatitis A virus and mechanism of neutralization

6.1 Introduction to HAV and its receptor

HAV is an ancient and ubiquitous pathogen found in primates and small mammals [173]. HAV belongs to the family of *Picornaviridae* and genus *Hepatovirus*, which is a sole member of this family. HAV is unique amongst picornaviruses in targeting the liver, and despite a successful vaccine it continues to be a source of mortality [174]. HAV isolates belong to a single serotype [175]. It has radically different properties from those of other picornaviruses: it exists in an enveloped form in the blood but is shed in feces as a naked, nonenveloped particle (Fig. 6.1) [176]; it possesses a low G/C ratio in the genome sequence and a strong codon bias [177]; it grows poorly in tissue culture; it possesses a 67-residue carboxy-terminal extension of VP1 (VP1-2A or VPX), which is important for viral assembly [178]; it has a very short, unmyristoylated VP4 (~23 residues) [179] and HAV is extremely resistant to degradation caused by environmental conditions, which include thermal denaturation (*i.e.*, HAV survives at 70 ℃ for up to 10 min), acid treatment (*i.e.*, pH 1 for 2 h at room temperature), 20% ether and chloroform, and detergent inactivation (*i.e.*, HAV survives at 37 ℃ for 30 min in 1% SDS) [180]. Due to its unique properties, HAV remains enigmatic and occupies an evolutionary position on the periphery of picornaviruses [25, 181]. T cell immunoglobulin and mucin domain 1 (TIM-1) [182] acts as a potential receptor for HAV, and although transcytosis occurs [183], it is not clear how the virus gets to the liver cells, its principal site of replication.

Recently, structures of a mature virion and an empty particle of HAV were determined [25], which extends our understanding of structural variability within the picornavirus family. The external surface of HAV appears as a faceted triakis icosahedron, and bears no a continuous hydrophobic pocket in VP1 [25]. HAV particle surface was remarkably negatively charged and the fringes of the pentameric assemblies, which showed some positive charge (Fig. 6.2), were decorated with a string of sulphate ions, derived from the crystallization media [25]. It showed no trace of the enterovirus canyon, often the site of receptor binding [20, 44] (Fig. 6.1), and provided no clues as to where TIM-1, the cellular receptor [184, 185] might attach. These structural features suggest that the HAV probably uncoats via a novel mechanism, which is different from those utilized by other picornaviruses [180].

Structural characterization of an HAV–TIM-1 complex would shed light on the cell entry mechanism, but has been challenging because of the difficulty in obtaining homogenous complex preparations due to very low binding affinity (unpublished observations).

However it is known that neutralizing antibodies protect against virus infection by mechanisms that include blocking attachment to the cellular receptor, disturbing viral genome release or physically destabilizing the virus [186, 187], structural studies on such neutralizing antibodies can therefore help illuminate the corresponding biological function.

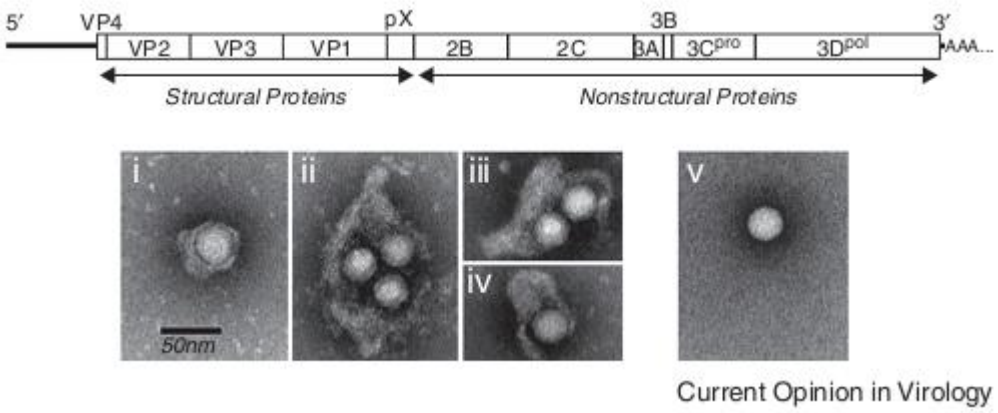

Fig. 6.1 HAV genome organization and electron microscopic images of negative-stained enveloped HAV particles (eHAV). Reprinted by permission from Macmillan Publishers Ltd: Nature [176], copyright (2013).

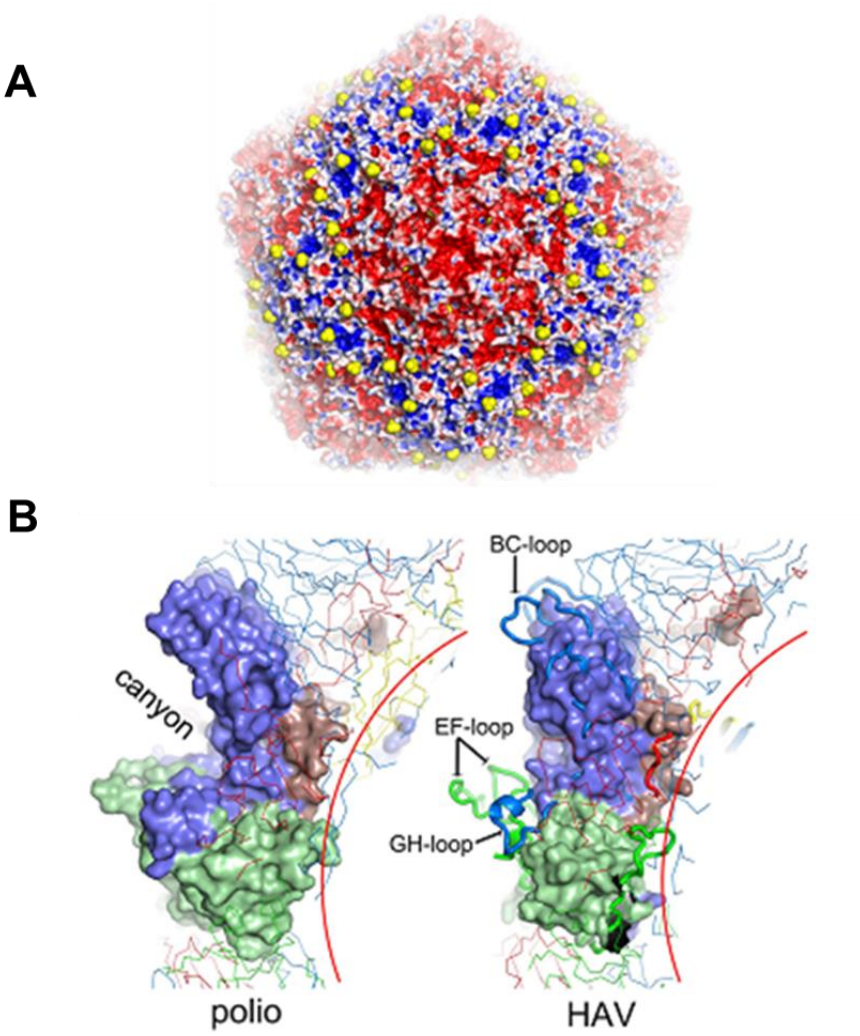

Fig. 6.2 Structure features of HAV. (A) The electrostatic surface of HAV computed using the APBS tool of PyMOL. Red represents negative, blue positive and white neutral charge. Sulphate ions are shown in yellow. (B) Comparison of HAV and poliovirus. Surface renditions of the biological protomer are shown against a ribbon depiction of the capsid shell cut through so the view is of a side of a protomer. The loops, which contribute to the walls of the canyon in poliovirus, are highlighted by a thicker cartoon representation and labeled. Reprinted by permission from Macmillan

Fig. 6.3 Stability of HAV particles.

Publishers Ltd: Nature **[25]**, copyright (2014).

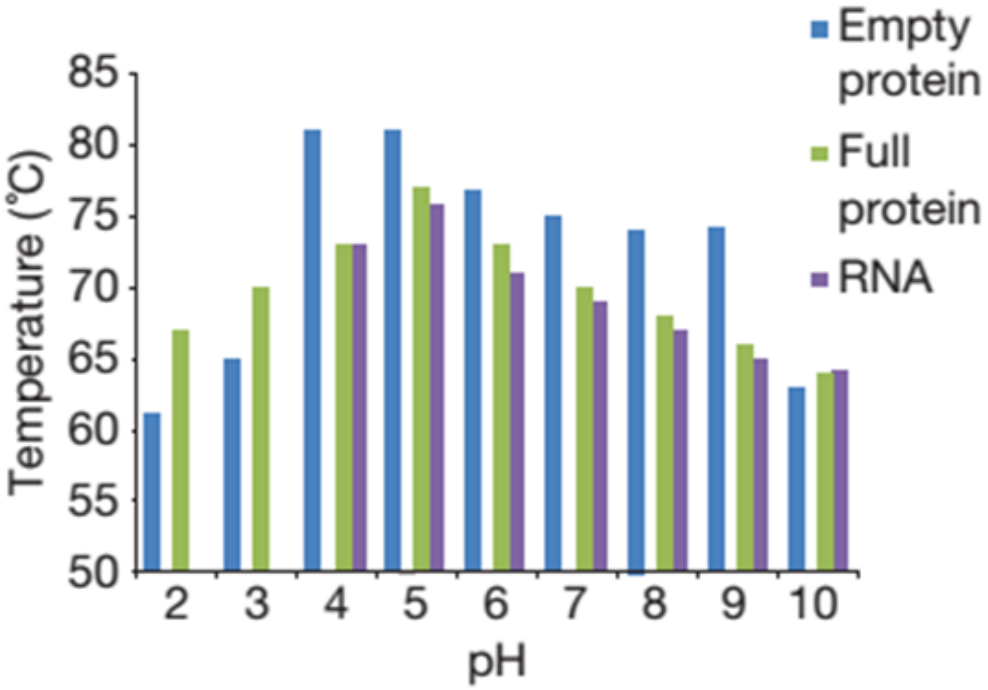

Fig. 6.3 Stability of HAV particles. Summary of thermal shift assays for HAV in the pH range from 2 to 10. The purple and green bars represent RNA release and protein melting temperatures respectively for the mature HAV; blue bars show protein melting temperatures for the empty particle. Reprinted by permission from Macmillan Publishers Ltd: Nature **[25]**, copyright (2014).

Fig. 6.3 Stability of HAV particles.

Table. 6.1 *In vitro* neutralization assays of monoclonal antibodies against HAV. EV71 mAb D6 is used as a negative control.

Antibodies	Neutralization Titers	Antibodies	Neutralization Titers
	HAV		HAV
R1	1:512	R14	1:512
R2	1:2048	R15	1:1024
R3	<1:8	R16	<1:8
R4	1:1024	R17	<1:8
R5	<1:8	R18	1:2048
R6	<1:8	R19	1:512
R7	<1:8	R20	<1:8
R8	1:1024	R21	<1:8
R9	<1:8	R22	1:512
R10	1:4096	R23	1:1024
R11	<1:8	R24	1:1024
R12	1:256	R25	<1:8
R13	<1:8	D6 (mAb)	<1:8

Fig. 6.3 Stability of HAV particles.

6.2 HAV neutralizing monoclonal antibodies preparation

Twenty-five monoclonal antibodies (mAbs) were generated by immunizing mice (see Chapter 2.2.1). Of these, thirteen mAbs show good neutralizing activities against HAV infection (Table. 6.1). Notably, R10 had the highest neutralizing title of 1:4096 (Table. 6.1). Thirteen neutralizing mAbs were sequenced and purified by protein A affinity chromatography from mice ascites (see Chapter 2.2.2 and Chapter 2.2.3). R10 Fab fragments were prepared with the use of the Pierce FAB preparation kit (Thermo Scientific) according to the manufacturer's instructions, dialyzed against 20 mM acetate (pH 5.0) at 4 ℃, loaded onto a Mono S column (GE Healthcare) and eluted using a 0–500 mM NaCl gradient. The main peak was collected and dialyzed into PBS buffer. The antibody and the Fab concentrations were determined by absorbance at 280 nm, and the purity confirmed by SDS–PAGE analysis (Fig. 6.4).

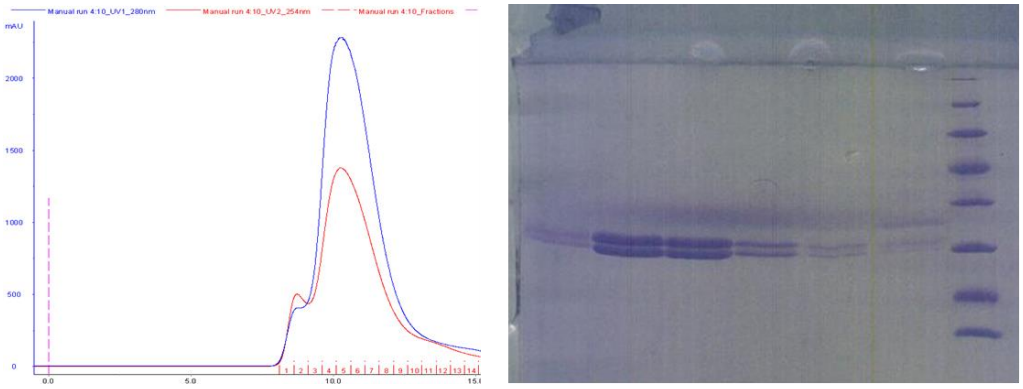

Fig. 6.4 Purification of R10 Fab (Left) using a Mono S column and SDS-PAGE analysis of purified R10 Fab (Right).

Fig. 6.3 Stability of HAV particles.

6.3 Expression and purification of TIM-1 Ig V domain

The Ig V domain of human TIM-1 (residues 22-129) was cloned into a pET-22b vector (Novagen) between Nde I and Xho I restriction sites with a C-terminal 6× His-tag and was expressed as inclusion bodies in *E. coli* BL21 (DE3). Protein from inclusion bodies was solubilized by using a de-naturation and refolding protocol. The refolding buffer (50mM Hepes, 0.4M L-arginine, 6.3mM GSH, 3.7mM GSSG, 2mM EDTA, pH 7.0) was used to refold the TIM-1 Ig V domain, which was denatured with the buffer of 20mM Tris, 6M guanidine hydrochloride, 2mM DTT, 10mM EDTA, pH 8.5. The denatured proteins were dialyzed against a 100-fold excess of refolding buffer. The re-folded protein was purified further using Ni-NTA affinity chromatography and size exclusion chromatography (Superdex G75 column). SDS-PAGE and thermal stability analysis verified that TIM-1 Ig V domain represents good purity and stability (Fig. 6.5).

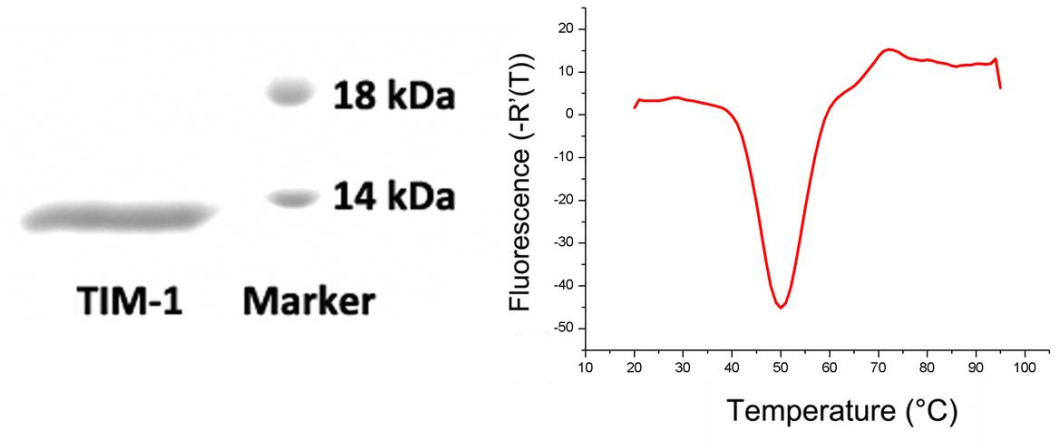

Fig. 6.5 SDS-PAGE and thermal stability analysis of purified TIM-1.

Fig. 6.3 Stability of HAV particles.

6.4 R10 interferes with viral uncoating

R10 had the strongest neutralizing activity against HAV (50% neutralizing concentration [$neut_{50}$] value of 1nM, ~0.15 μg/ml), and the Fab fragment is also strongly neutralizing ($neut_{50}$= 12nM, ~1.8 μg/ml) (Fig. 6.6). R10 does not recognize linear epitopes by immunoblot, but recognizes conformational epitopes by ELISA, and shows similar binding affinities to full and empty particles (Fig. 6.6). Interestingly a fluorescent assay revealed that the R10 Fab destabilizes full HAV particles by 7 ℃, whilst the bi-valent intact antibody induces a two-stage transition in protein conformation to release the RNA genome (Fig. 6.7), the first event also corresponds to a destabilization, whereas the second indicates enhanced stability, presumably due to the antibody holding the particles together. TIM-1 IgV domain alone has no effect on viral stability in thermofluor assays (Fig. 6.7). This observation is consistent with previous reports, which conclude that although TIM-1 Ig V domain is necessary for binding of HAV, both TIM-1 IgV domain and mucin domain are required to trigger uncoating of HAV [39]. Although low pH is necessary for uncoating in some picornaviruses, *e.g.* FMDV, HAV is extremely robust at low pH (pH 5.0), even after R10 binding (Fig. 6.7), suggesting that an acidic environment might not be essential for HAV uncoating. Note that even after Fab destabilization the HAV particles still do not start to uncoat at physiological temperature and remain as stable as most picornaviruses, so that destabilization is

Fig. 6.3 Stability of HAV particles.

unlikely to be the neutralization mechanism.

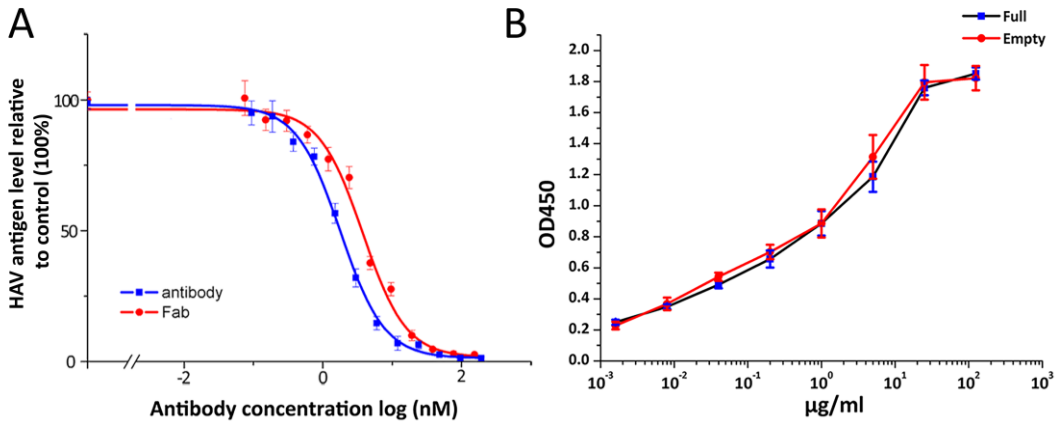

Fig. 6.6 Characterizations of R10. (A) Neutralization of HAV by R10. Whole Ig G and Fab fragments of R10 were used to block HAV infection at different concentrations by detecting HAV capsids. The red and blue symbols represent whole antibody and Fab fragments respectively. (B) Analysis of binding of R10 to HAV mature virions and empty particles by ELISA.

Fig. 6.3 Stability of HAV particles.

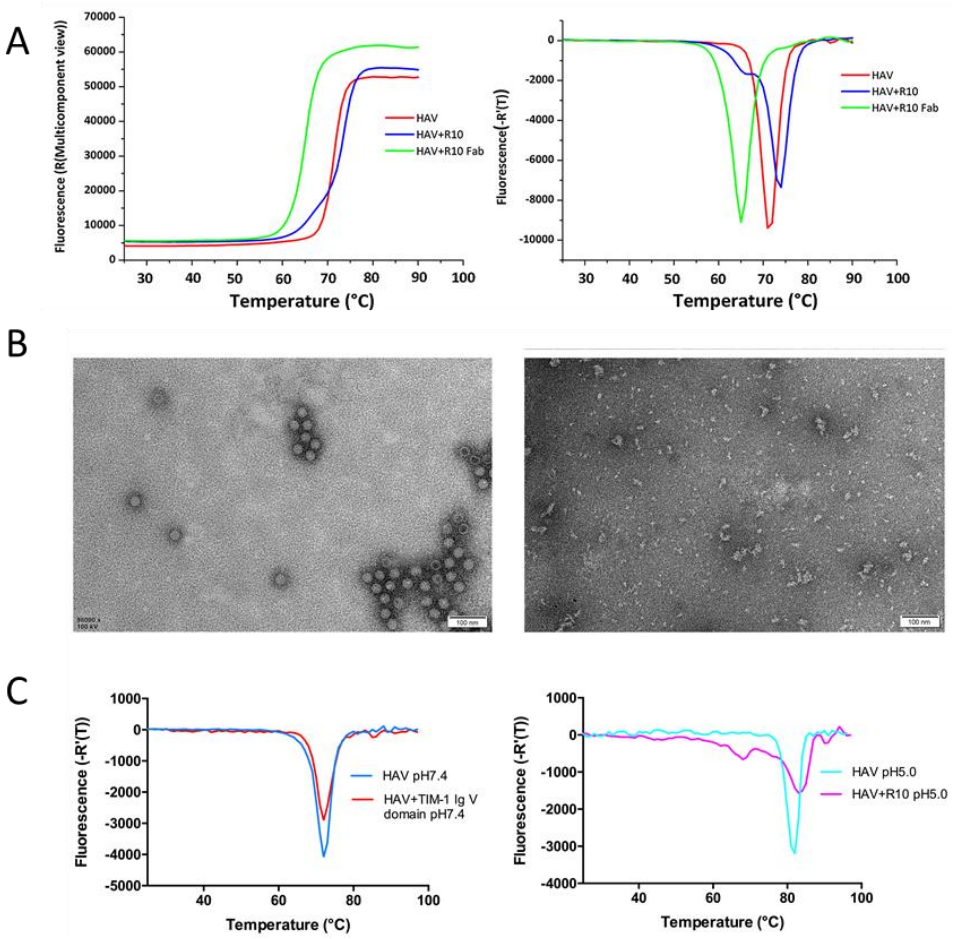

Fig. 6.7 Stability of HAV particles upon binding to R10 or R10 Fab or TIM-1 Ig V. (A) The stabilities of HAV full particles and their complexes with R10 whole Ig G and Fab fragments at neutral pH were determined by thermofluor assay using the dye SYTO9 to detect RNA exposure (Left). (B) Negative stain images of HAV particles complexed with R10 in PBS buffer at room temperature (Left) or after heated-treatment at 75 ℃ for 10 min (Right). (C) The stabilities of HAV full particles and their complexes with TIM-1 Ig V at neutral pH (Left) or the stabilities of HAV full particles and their complexes with R10 at acidic pH (Right) were determined by thermofluor assay using the dye SYTO9 to detect RNA exposure.

Fig. 6.3 Stability of HAV particles.

6.5 R10 prevents virus attachment

For HAV the mechanism of RNA genome release remains unclear and it is possible that a cellular receptor or a specific host factor may be required for particle disassembly. Given the ability of the R10 Fab to destabilize HAV it is possible that the binding sites on HAV of the host factor and R10 overlap partially or fully. To explore the mechanism of neutralization, real-time reverse transcriptase-PCR (RT-PCR) was carried out to quantify the virus remaining on the cell surface, following exposure to antibodies pre- and post-virus attachment to cells at 4 ℃. The results suggest that R10 prevents HAV attachment to the cell surface and is able to displace virus that has already bound to the cell receptor (Fig. 6.8). In addition, R10 competitively blocked TIM-1 binding to HAV (Fig. 6.8), suggesting that R10 prevents HAV from attaching to host cells by blocking the binding of HAV to its cellular receptor TIM-1. (RT-PCR experiments were performed by Dr. Xiangxi Wang).

Fig. 6.3 Stability of HAV particles.

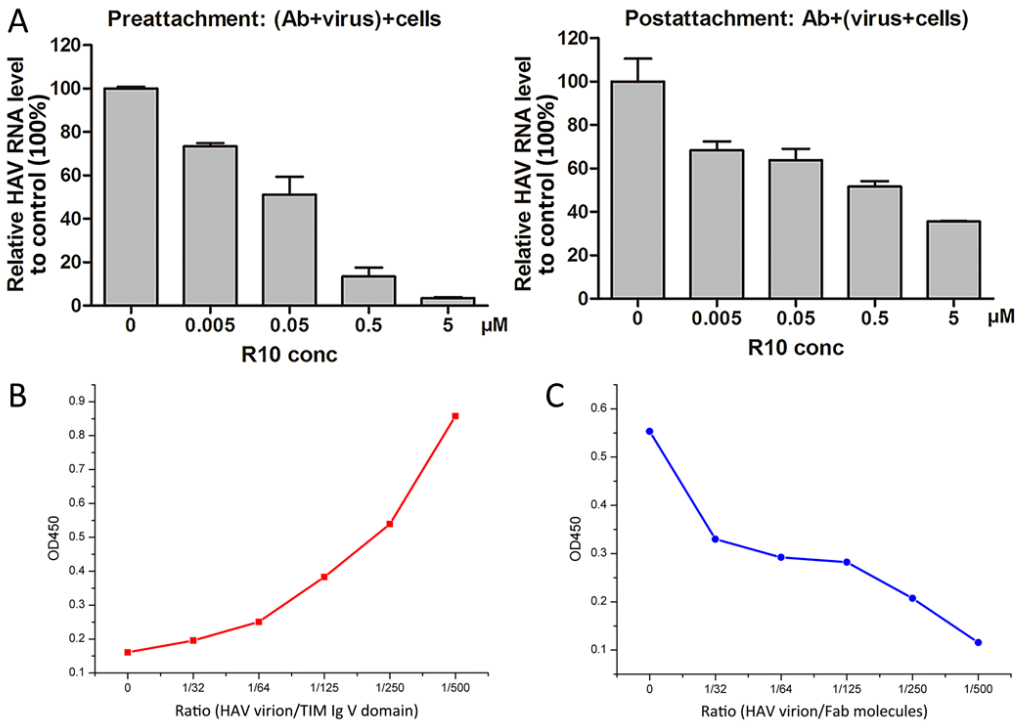

Fig. 6.8 R10 prevents virus attachment. (A) Amount of virus on the cell surface, as detected by RT-PCR, when exposed to R10 before (Left) and after (Right) the virus was allowed to attach to cells. High concentrations of R10 prevent attachment of HAV to the cell surface when HAV is exposed to R10 before cell attachment and R10 can strip HAV off the cell surface when HAV is exposed to R10 post attachment. (B) The binding of soluble TIM1 Ig V to HAV was measured by ELISA. 96-well plates were coated with HAV full particles and various concentrations of soluble TIM-1 Ig V (at ratios of ~32, 64, 125, 250 and 500 TIM-1 Ig V molecules per HAV virion) were added. The amount of bound TIM-1 Ig V was detected by HRP assay. (C) Blocking of soluble TIM-1 Ig V binding to HAV by R10 Fab was demonstrated

Fig. 6.3 Stability of HAV particles.

by ELISA. 96-well plates were coated with HAV full particles and mixtures of soluble TIM-1 Ig V and R10 Fab at different concentrations (the concentration of TIM-1 Ig V was fixed at ~250 TIM-1 Ig V molecules per HAV virion) and the indicated concentrations of R10 Fab (at ratios of ~32, 64, 125, 250 and 500 Fab molecules per HAV virion) were added. The amount of bound TIM-1 Ig V was detected by ELISA.

6.6 Crystallization, X-ray data collection and structure determination of the R10 Fab

The purified R10 Fab was concentrated to 8 mg/ml, and crystallization screening carried out using the sitting-drop vapour diffusion method. Cubic crystals appeared in 20% PEG3350, 0.2 M sodium thiocyanate within 2 weeks. Cryo-cooling was carried out by soaking the crystals in reservoir solution containing 20% (v/v) glycerol prior to flash-cooling with liquid nitrogen and kept at −173 °C during X-ray data collection at IO3, Diamond Light Source. Diffraction data images (exposure time 0.1 s with 40% beam transmission) of 0.1 ° rotation were recorded on a PILATUS 6M detector, at a wavelength of 0.9765 Å to a resolution of 2.9 Å. The data were processed, integrated, and scaled using the HKL2000 package [87]. The crystals belonged to space group $P2_1$ with cell parameters a = 52.5 Å, b = 140.5 Å, c = 68.9 Å, β = 110 °. Two Fab molecules in an asymmetric unit with a solvent

Fig. 6.3 Stability of HAV particles.

content of 51.74% (corresponding to a Matthews coefficient VM= 2.55 Å3/Da) was found from crystals of R10 Fab. Structure determination was by molecular replacement with a Fab search model (PDB ID 1QGC [188]) using the program Phaser [95]. Manual model building and refinement were performed with COOT [96] and PHENIX [97] with two fold NCS restraints applied. The r.m.s. deviation between the two NCS-related subunits of R10 Fab is 0.059 Å. Chain A (Light chain) and Chain B (Heavy chain) were selected for following structural analysis. Data collection and structure refinement statistics are summarized in Table. 6.2.

Table. 6.2 Data collection and refinement statistics.

Name	R10 Fab
Data collection	
Resolution (Å)	50.00-2.90 (3.00-2.90)
Unique reflections	20,094 (1,942)
Space group	$P2_1$
Cell dimensions	
a (Å)	52.5
b (Å)	140.5
c (Å)	68.9
α (°)	90.00
β (°)	110.36
γ (°)	90.00

Fig. 6.3 Stability of HAV particles.

Redundancy	3.1(2.6)
Completeness (%)	97.9 (95.6)
R_{merge}	0.26 (0.707)
$I/\sigma(I)$	3.68 (1.40)
Refinement	
Resolution(Å)	3.00
No.reflections	18,448
R_{work}/R_{free}	0.233/0.264
No. of non-H atoms	
Protein	6,520
Mean B-factor(Å^2)	20.3
Ramachandran statistics (%)	
Most favoured	93.62
Allowed	5.91
Outliers	0.47
R.m.s.deviations	
Bond lengths(Å)	0.005
Bond angles(◦)	1.048

Values in parentheses are for the highest-resolution shell.

[a] $R_{merge} = \Sigma_{hkl} \Sigma_i |I(hkl)_i - \langle I(hkl) \rangle| / \Sigma_{hkl} \Sigma_i I(hkl)_i$,

[b] $R_{work} = \Sigma_{hkl} |Fo(hkl) - Fc(hkl)| / \Sigma_{hkl} Fo(hkl)$.

[c] R_{free} was calculated for a test set of reflections (5%) omitted from the refinement.

Fig. 6.3 Stability of HAV particles.

6.7 Structural comparisons of R10 Fab with Ig V domain

The extracellular portion of TIM-1 contains an N-terminal immunoglobulin variable-like (Ig) domain (Ig V) followed by a mucin-like region before the protein enters the cell membrane. The Ig V is required for binding of HAV, but without the mucin-like region soluble Ig V binds and neutralizes HAV inefficiently [39]. Ig V shares structurally similarity with both the VH and VL domains of R10 Fab but is markedly more similar to the VL domain (RMSD for 89.3% and 95.4% of Cαs is 5.3 and 3.4 Å for VH and VL respectively) (Fig. 6.9). The major point of interaction of the VH domain is in the extended CDR3 region (Our lab determined the cryo-EM structure of the HAV full particle complexed with R10 Fab at 4.2 Å), which has no structural similarity in Ig V, however it is intriguing that the major interactions with the VL domain are with the framework region – a region which can be part of the adhesion surface in Ig-like adhesion molecules [189].

Fig. 6.3 Stability of HAV particles.

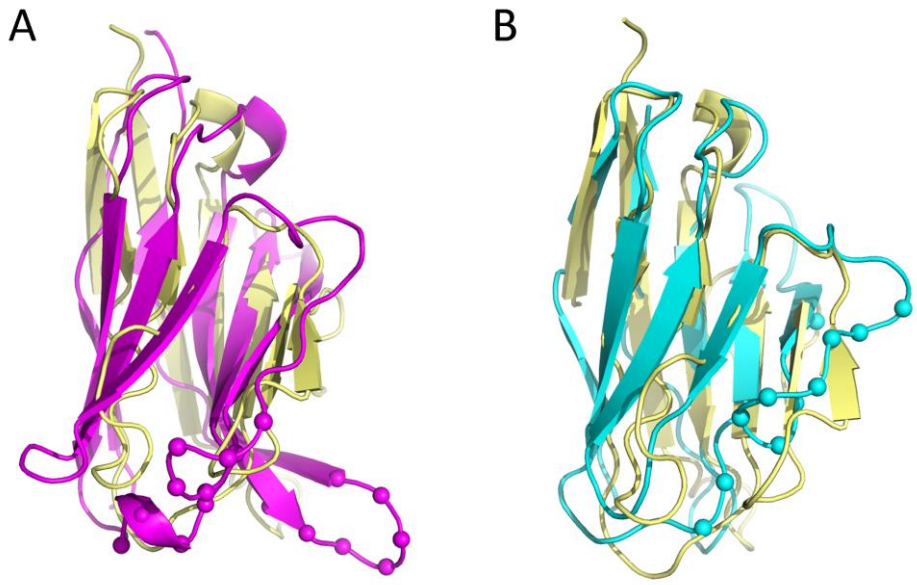

Fig. 6.9 Structural comparisons of the TIM-1 Ig V domain (PDB: 5DZO [185]) with R10 Fab heavy chain (A) and light chain (B). TIM-1 Ig V domain is colored in pale yellow, the R10 Fab heavy and light chains are colored in magenta and cyan respectively. Residues involved in binding HAV are represented as spheres.

Fig. 6.3 Stability of HAV particles.

6.8 Discussion-- a receptor mimic neutralizing mechanism

The cryo-EM structure of the HAV full particle complexed with R10 Fab at 4.2 Å, determined by our lab recently [190], together with the crystal structure of the R10 Fab allowed us to build a reliable model of the complex (Fig. 6.10). R10 binds to the viral surface along the edges of the pentameric building block of the virus, between the 2-fold and 3-fold axes (Fig. 6.10). The heavy-chain and light-chain variable domains contribute ~60% and ~40% of the protein-protein interface respectively, with the heavy chain predominantly binding VP3, whilst the light chain binds VP2 and VP3. Interestingly R10 binding displaces a string of sulphate ions bound to the positive charges fringing the pentameric assemblies contributed by R67 of VP2, and K150 and R209 of VP3 (Fig. 6.11) [25], an area predicted to bind the protein or glycans of TIM-1. Together with the observation that the R10 VL domain is markedly similar to the Ig V domain, it is therefore conceivable that TIM-1 binding to HAV involves both Ig V, interacting via interactions that may recapitulate the R10 VL contacts, and also via the mucin-like domain, however the binding of TIM-1 is much weaker than R10, perhaps consistent with much of the affinity of R10 deriving from VH interactions. These results, together with our observation that the R10 Fab destabilizes the capsid, suggest the use of a receptor mimic mechanism to neutralize virus infection, providing new opportunities for therapeutic intervention.

Fig. 6.3 Stability of HAV particles.

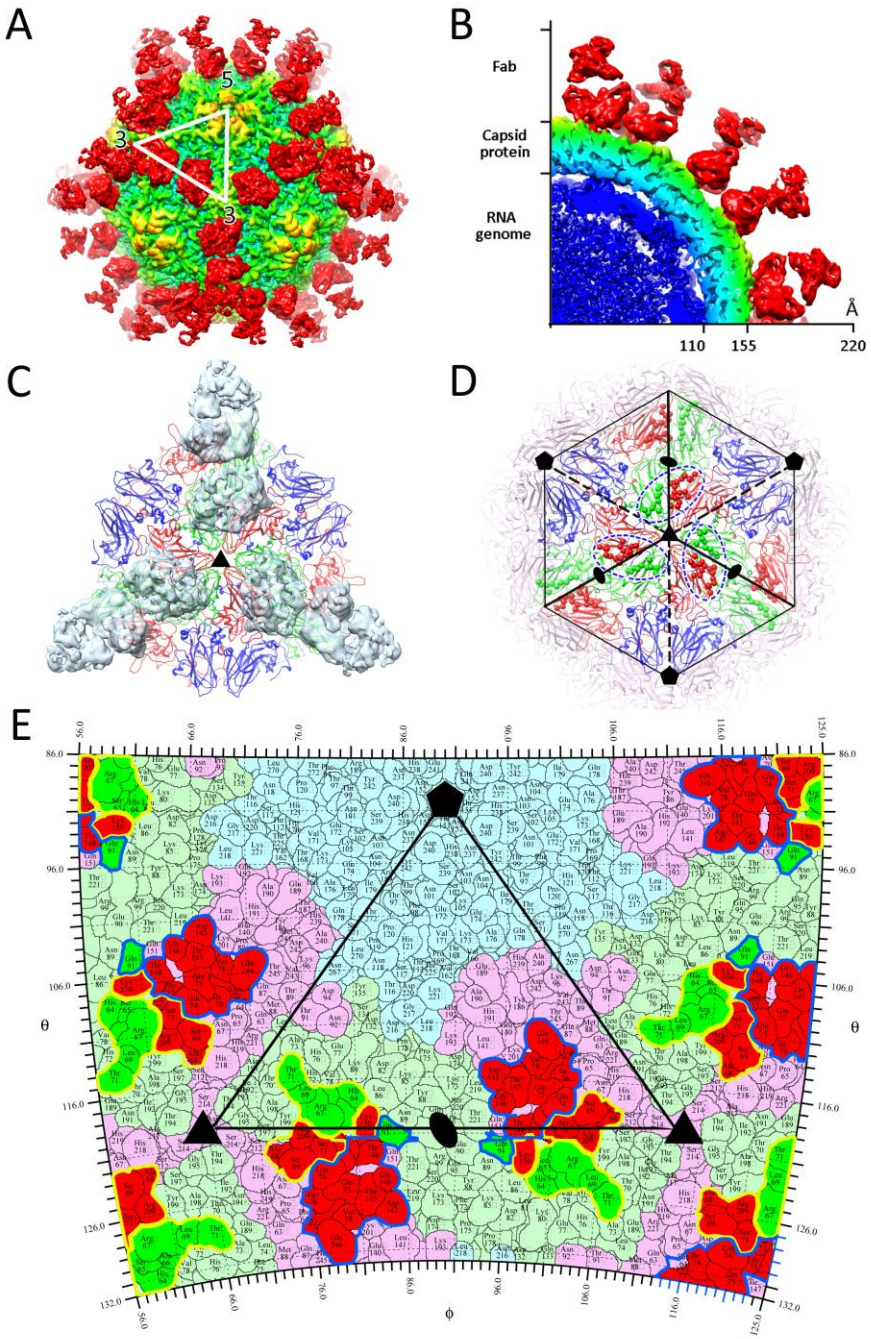

Fig. 6.10 The 4.2 Å resolution cryo-EM structure of the R10 Fab: HAV full particle complex. (A) Shows the surface and (B) the cross section of the cryo-EM

Fig. 6.3 Stability of HAV particles.

map. The HAV particle is radial colored as indicated and the R10 Fabs are shown in red. One icosahedral asymmetric unit is indicated by a white triangle. (C) The R10 Fab binds to the viral surface along the pentamer interface between the 2-fold and 3-fold axes. (D) The R10 epitopes on six asymmetric units of the HAV surface. VP1, VP2 and VP3 are colored in blue, green and red respectively, residues interacting with heavy and light chains of the Fab are shown as spheres. The boundary of each epitope is marked with a deep blue dashed ellipse. (E) The R10 footprints on the HAV surface. The figure shows a 2D projection of the HAV surface produced using RIVEM [191]. Residues of VP1, VP2, and VP3 are outlined in pale blue, green, and red, respectively; residues involved in binding to R10 are shown in brighter colors corresponding to the protein chain they belong to. The footprints of R10 heavy and light chains are indicated by blue and yellow lines respectively. Five-, three-, and twofold icosahedral symmetry axes are marked as for D on one icosahedral asymmetric unit.

Fig. 6.3 Stability of HAV particles.

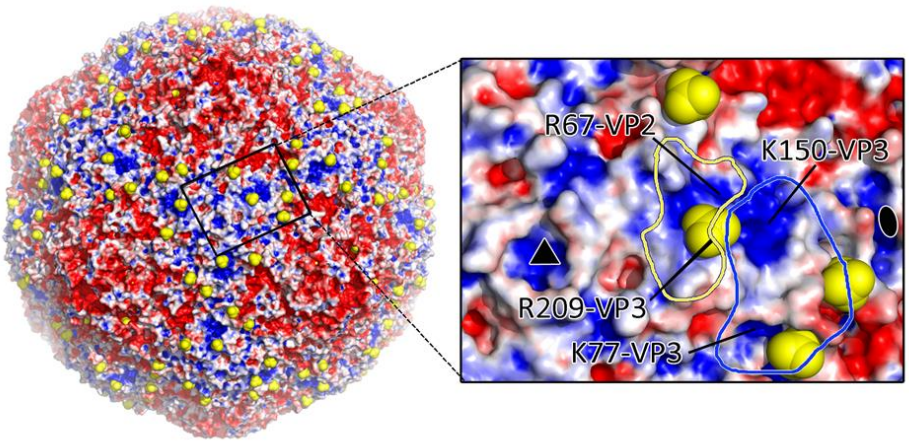

Fig. 6.11 HAV electrostatic surface. Red, blue and white represent negative, positive and no charges respectively. Yellow spheres mark the positions of bound sulphates in the X-ray structure. Right panel: Close up. Regions correlated with the R10 heavy and light chains binding sites are indicated by blue and yellow lines respectively. Residues that dominate the positively charged surface, as well as interacting with R10, are labeled. Reprinted by permission from Macmillan Publishers Ltd: Nature [25], copyright (2014).

Chapter 7
Structural and functional studies on 2As from the *Parechovirus* genus

7.1 Introduction to 2As from picornaviruses

The 2A protein appears to be the most diverse among picornaviruses, in contrast to the other non-structural proteins, which tend to be rather well conserved. In enteroviruses, the 2A acts as a protease, cleaving the site between the C-terminus of capsid protein VP1 and the N-terminus of the protease itself, thus separating the capsid polyprotein from the nonstructural polyprotein [192, 193] and also participating in the shutting down of the host protein synthesis through cleavage of the host eukaryotic initiation factor 4G (eIF4G) [194, 195]. In hepatitis A virus, the 2A is not a protease, but plays a critical role in viral assembly [196, 197] (Fig. 7.1). In contrast, in the cardio and aphthoviruses the cleavage site between the capsid protein and replicative protein regions occurs at the 2A/2B junction [198]. The cardiovirus 2A region is about 140 amino acids long whilst aphthovirus 2A is only 18 amino acids long. Although the function of the N-terminal region of cardiovirus 2A is unclear, the C-terminal end of cardiovirus 2A is similar to the aphthovirus 2A, both act as proteases to cleave the 2A/2B junction [199].

The 2A proteins of parechovirus family members are homologous to the corresponding region of the polyprotein of avian encephalomyelitis virus (AEV), and the 2A protein of Aichi virus [144]. Furthermore, these 2A proteins share a ~20%-25% amino acid sequence similarity (Fig. 7.2) with an identified family of cellular proteins [129], eg. Phospholipase 2 (PLA2), and a highly conserved

picornaviral H-box/NC motif is identified among them, which might provide a clue to the roles of 2As in the viral infection process (Fig. 7.1 and Fig. 7.3). PLA2 was reported to act as a tumor suppressor by suppressing HRAS induced transformation, inhibiting cell proliferation, colony formation, and promoting apoptosis, before its phospholipase activity was discovered [200]. Meanwhile PLA2 was reported to contribute to tumor progression through altered metabolic pathways that its hydrolysated product, lysophosphatidic acid (LPA), acting as a critical signal transduction molecule and metabolism regulator, promotes tumor progression by modulating cytoskeletal changes, cell-cell contacts, cell survival, proliferation, invasion and metastasis [200-202]. Interestingly, PLA2 was found to represent a switch between entry and clearance of *Picornaviridae* [203]. Regarding the entry of picornaviruses, PLA2 can be involved in initiating pore formation and facilitating viral genome release [203]. Given the fact that the 2A proteins of parechovirus and Aichivirus are homologues of PLA2, it is of interest to determine if the 2A in the parechovirus family presents the structural characteristics of PLA2 and exhibits phospholipase activity.

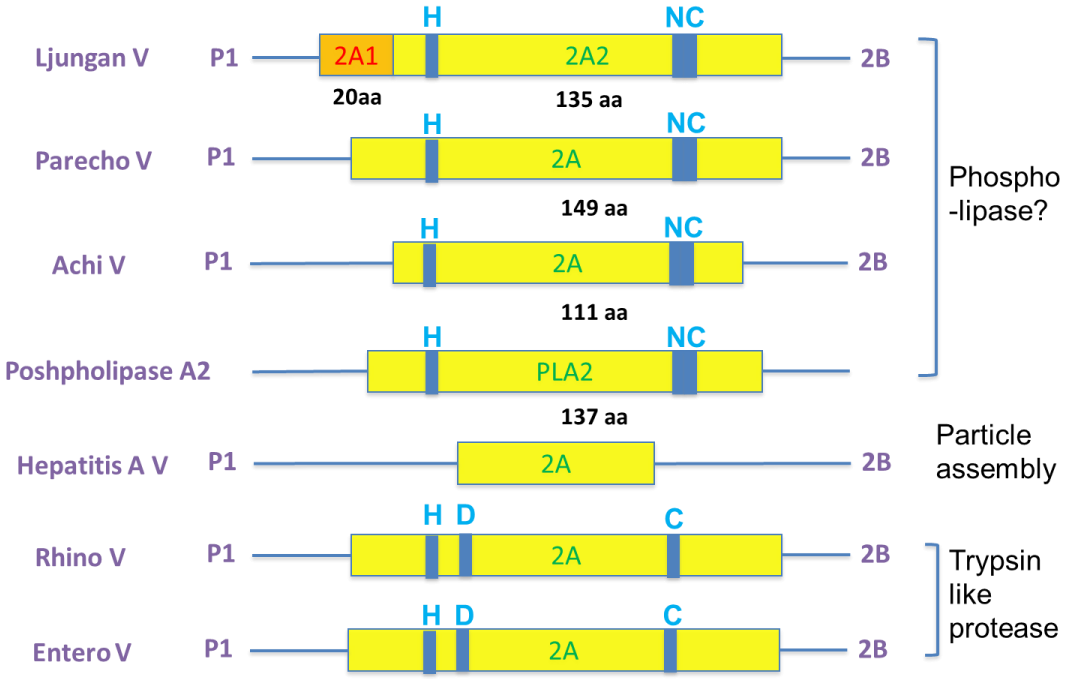

Fig. 7.1 Schematic diagram of conserved motifs of 2As in the picornavirus family.

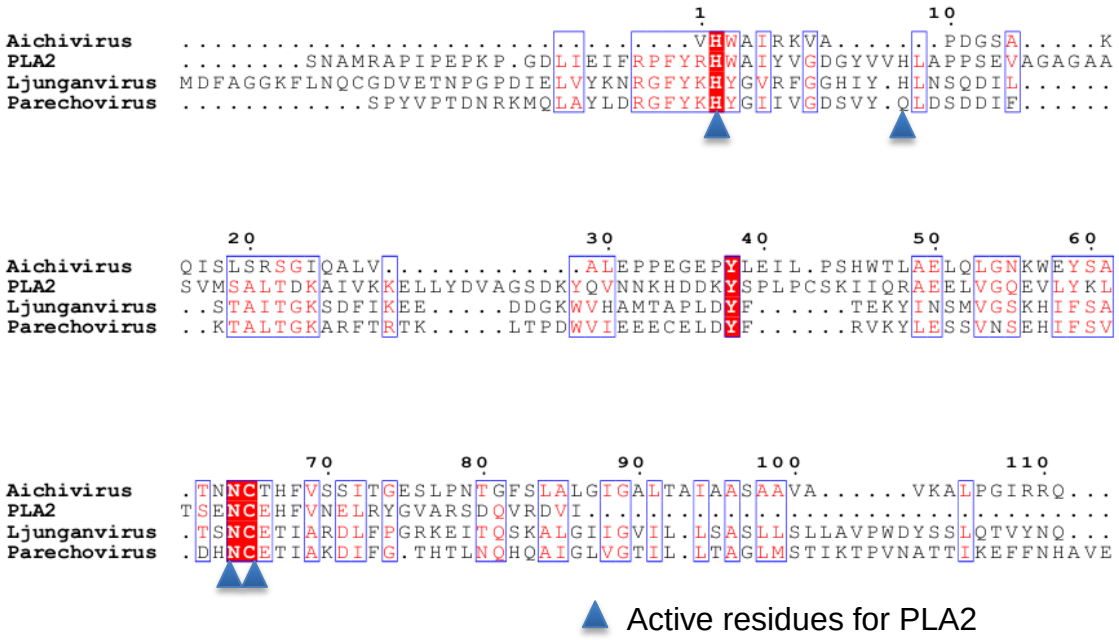

Fig. 7.2 Multi-sequence alignment of picornaviral 2As and PLA2.

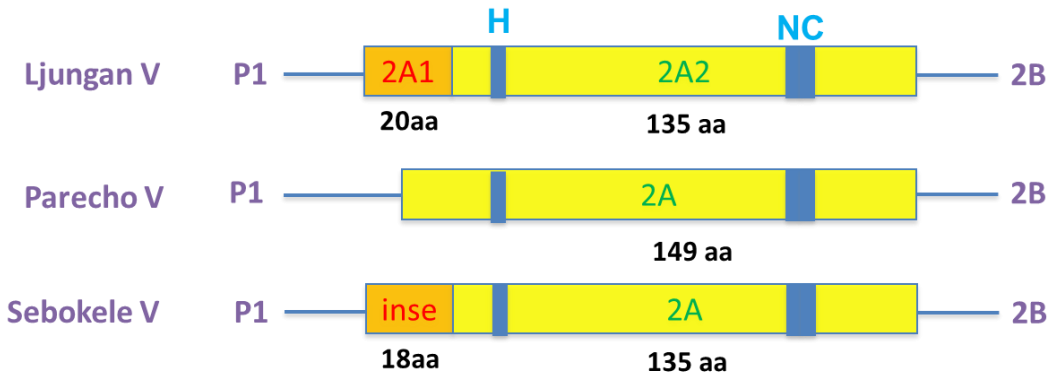

Fig. 7.3 Schematic diagram of 2As from LV, HPeV and SEBV. 2As from different species are expressed (Table. 7.1) and set up for crystallization and used for structure determination and functional study.

Table. 7.1 Constructs summary for 2As

Constructs	**Vectors**	**Expression**	**Crystallization**	**Structure solved**
LV 2A (21-155) at pH 7.5	PET28a	Good	Yes	Yes
LV 2A (21-111) truncation	PET28a	Not good	No	No
LV 2A (21-113) truncation	PET28a	Not good	No	No
LV 2A (21-115) truncation	PET28a	Not good	No	No
LV 2A (21-115) truncation	PGEX-6P-1	Good	Yes	No
HPeV 2A (1-149)	PET28a	Good	Yes	Yes
HPeV 2A (1-149)	PGEX-6P-1	Good	No	No
SEBV 2A (1-135)	PET28a	No	No	No
SEBV 2A (1-135)	PGEX-6P-1	Good	Yes	Yes
HRVC 2A	PGEX-6P-1	Good	Yes	Yes

7.2 2A proteins expression and purification

2As from HPeV, LV and SEBV, are ~150 residues in length with a conserved H-box/NC motif (Fig. 7.1). Some 15 different constructs have been designed and expression trials performed in *E. coli* BL21 star strains, with different tags (GST and 6xhistidine) at either the N-terminus or C-terminus of the proteins (Table. 7.1). Most of the constructs were selected for large-scale expression and purification, while only a small number of these constructs yielded crystals which diffracted to very high resolution (Table. 7.1). The purification procedures of 2As were similar with an affinity chromatography (Ni-NTA or GST based) step followed by ion-exchange chromatography and gel filtration. Fig. 7.4 and Fig. 7.5 show that the 2As from LV, HPeV3 and SEBV1 are homogeneous with very high purity.

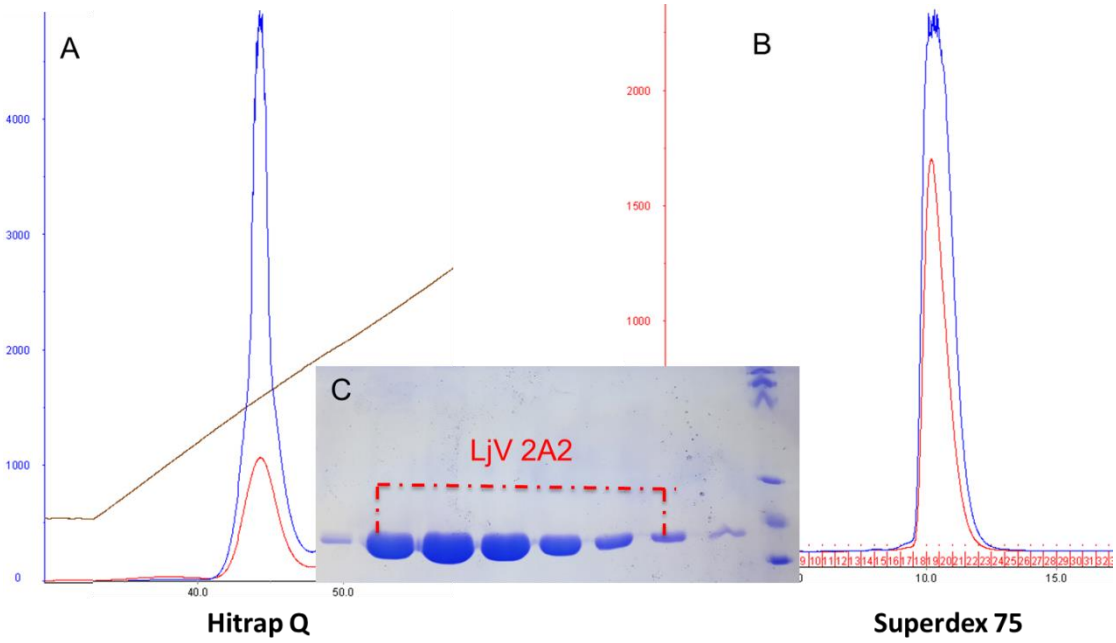

Fig. 7.4 Expression and purification of LV 2A2. (A and B) Hitrap Q and Gel filtration (Superdex 75) chromatography profiles, (C) SDS-PAGE gel of LV 2A2 after purification by gel filtration.

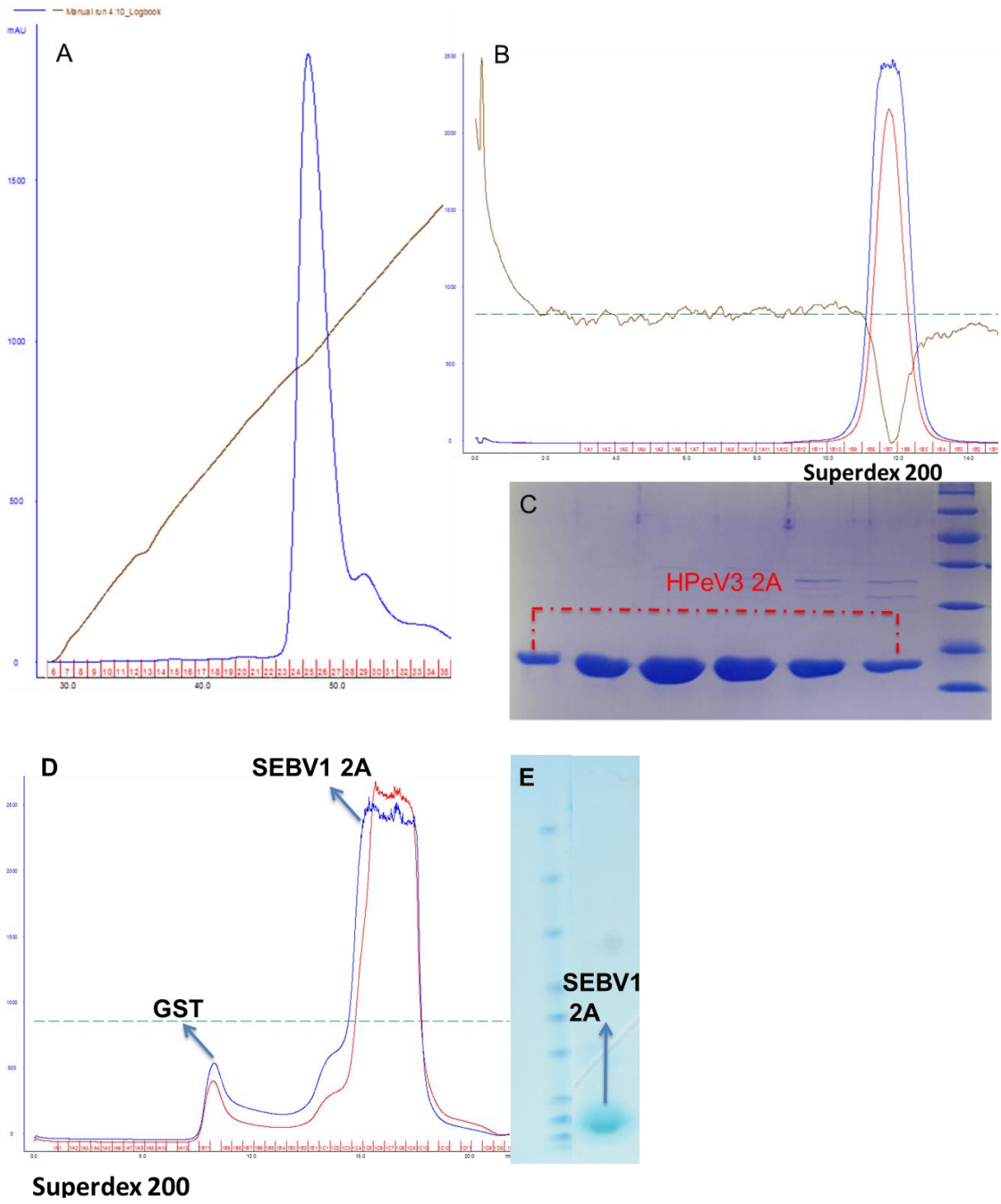

Fig. 7.5 Expression and purification of HPeV3 2A and SEBV1 2A. (A): Hitrap Q for HPeV 2A, (B) and (D): Gel filtration, (C) and (E): SDS-PAGE gels of HPeV 2A and SEBV1 2A after purification by gel filtration.

7.3 Crystallization and structure determination

Crystals of LV2 2A2 appeared from several conditions among the crystallization screens with 20% PEG3350 in different buffer solutions. Different approaches, including the standard dilution screen and additive screen, were applied to optimize the original crystallization conditions. Finally, thin plate crystals were grown at 16 ℃ using the sitting-drop vapor diffusion method [204] over a reservoir of 20% PEG3350, 0.2M sodium formate (pH 7.5) (Fig. 7.6). Crystals diffracted to 1.73 Å, belonged to the space group $P2_12_12_1$ and two protein molecules were in an asymmetric unit with a solvent content of 55% (corresponding to a Matthews coefficient VM=2.7 Å3 Da-1 [91]) (Detailed information about data collection is listed in Table. 2.2). The crystal structure of LV 2A2 was determined by using the molecular replacement method, with the crystal structure of HPeV1 2A (provided by Prof. Anastassis Perrakis) serving as the search model. The r.m.s. deviation between the two NCS-related subunits of LV 2A2 is 0.032 Å. Chain A was selected for following structural analysis. The final refinement Rwork value is 0.18 (Rfree of 0.22) (Table. 7.2).

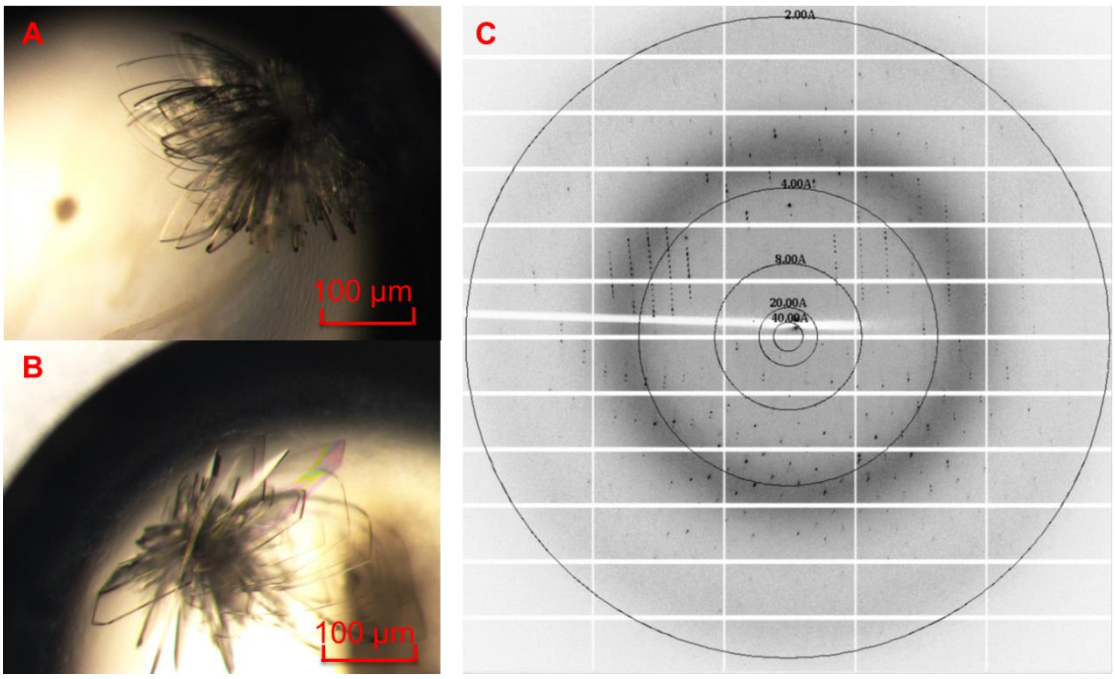

Fig. 7.6 LV 2A2 crystals and their diffraction pattern.

For HPeV3 and SEBV1 2As, crystallization used nano liter vapor diffusion in Greiner CrystalQuick X plates. Purified proteins were concentrated to ~70 mg/ml and 40 mg/ml respectively for crystallization. Many PEG conditions yielded "ball" crystals, which did not diffract well, finally, huge crystals of HPeV3 and thin plates crystals of SEBV1 were grown at optimized conditions of 1.7 M ammonium sulphate, 0.05 M sodium cacodylate trihydrate pH 6.0 and 30 % w/v polyethylene glycol 4000, 0.005 M magnesium acetate, 0.050 M sodium cacodylate pH 6.5 respectively (Fig. 7.7). The diffraction datasets for HPeV3 2A and SEBV1 2A were collected at beamline IO3, Diamond with the highest resolution being 2.4 Å and 1.5 Å, belonging to the space groups *R*3 and $P2_12_12$ respectively. Eight and two protein

molecules were found in an asymmetric unit with solvent contents of 51.74% and 58.52% for crystals of HPeV3 2A and SEBV1 2A respectively. The initial structure solutions of HPeV3 2A and SEBV1 2A were obtained by molecular replacement using the program Phaser with the crystal structure of LV 2A2 as a search model. Although there were eight HPeV3 2A molecules in an asymmetric unit, two classes of molecule with distinct conformations with r.m.s.deviation of 0.95 Å were observed among these eight HPeV3 2A proteins (the structural differences are discussed in Chapter 7.4). No NCS restraints were added during the refinement of HPeV3 2A. The r.m.s. deviation between the two NCS-related subunits of SEBV1 2A2 was 0.037 Å. Two fold NCS restraints were added during the refinement of SEBV1 2A2. Final refinement statistics are summarized in Table. 7.2.

Table. 7.2 Diffraction data from different 2As from the *parechovirus* genus.

Data collection			
Name	LV 2A2	HPeV3 2A	SEBV1 2A
Space group	$P2_12_12_1$	$R3$	$P2_12_12$
Cell dimensions (Å)	a = 39.79, b = 58.48, c = 110.24 Å	a = b = 141.9 Å, c = 184.0 Å	a = 64.4, b = 69.7, c = 57.3 Å

Resolution (Å)	50.0-1.73 (1.77-1.73)	50.0–2.40 (2.49–2.40)	50.0-1.50 (1.54–1.50)
Unique reflections	27,964 (1,979)	50,706 (6,580)	43,416 (2,911)
R_{merge}	0.122 (0.532)	0.112 (0.463)	0.075 (0.323)
$I / \sigma I$	12.2 (4.2)	10.8 (2.3)	22.9 (1.9)
Completeness (%)	99.9 (99.8)	100 (99.6)	99.4 (92.1)
Refinement			
Resolution (Å)	50.0 – 1.73	50.0 – 2.70	50.0 – 1.50
No. reflections	27,588	50,617	41,866
R_{work} /R_{free}	0.183/0.221	0.196/0.219	0.179/0.210
No. atoms	1,933	9,004	2,524
B-factors (Å^2)	35	43	40
R.m.s. deviations			
Bond lengths (Å)	0.012	0.011	0.008
Bond angles (°)	1.325	1.134	1.133

Values in parentheses are for the highest-resolution shell.

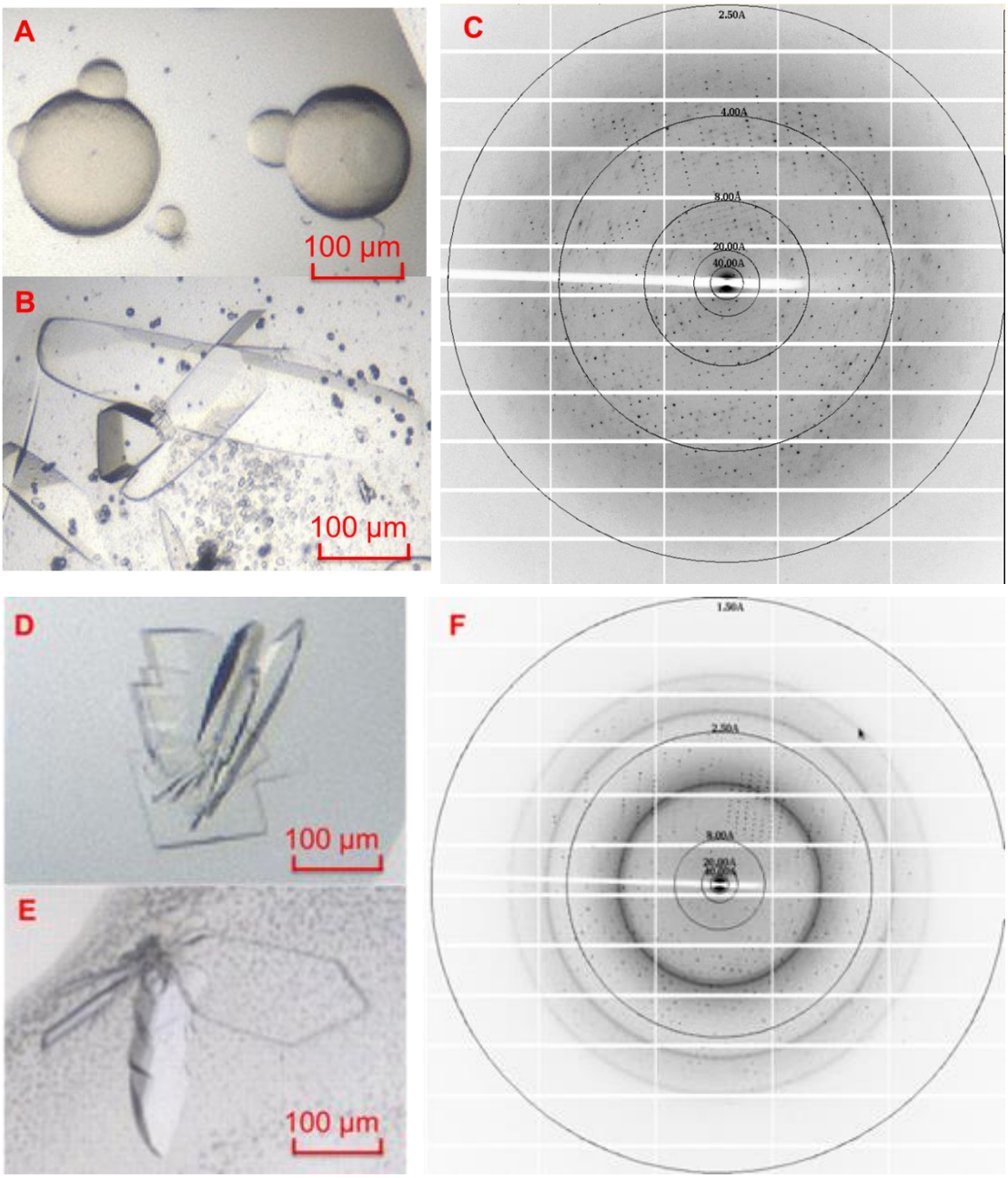

Fig. 7.7 HPeV3 2A (A-C) and SEBV1 2A (D-F) crystals and their diffraction patterns.

7.4 Overall structures and structural analysis

The crystal structure of LV 2A2 reported here reveals an α+β fold in a circular permutation of the topology of papain and members of the NlpC/P60 super-family of cysteine peptidases [205]. The N-terminal domain is mainly composed of five antiparallel β sheets and three α helices constitute the C-terminal domain with a very hydrophobic helix inserted into the core of the architecture, stabilized by a series of hydrophobic interactions with β strand B, α-turn and α Ⅰ (Fig. 7.8). The last ~15 C-terminal residues could not be traced in the electron density map. To explore the potential functions of LV 2A2 based on the structural analysis, the Dali Server was used to search the most similar structures. Adipose Phospholipase A2 (AdPLA) was selected as the highest scores. Exhibiting a relatively low primary sequence identity of about 20% with AdPLA [206], the overall structure of LV 2A2 showed a similarity with AdPLA with a root mean square deviation (r.m.s.d) of 3.85 Å for 102 C_α atom pairs. The largest deviations between LV 2A2 and AdPLA are observed in the C-domain with 3α helices circulating in opposite directions and a much longer, more hydrophobic helix in LV 2A2. The catalytic residues, comprising a distinctive His-His-Cys catalytic triad in AdPLA, are in a broadly similar configuration to that seen in the LV 2A2 structure, although one of these, the Cys, is pulled to the other side, a distance of 11 Å from the His (Fig. 7.10). Therefore, it is predicted that LV 2A2 can’t perform phospholipase activity in such a conformation. It would be very

interesting to know if LV 2A2 can adopt an alternative configuration.

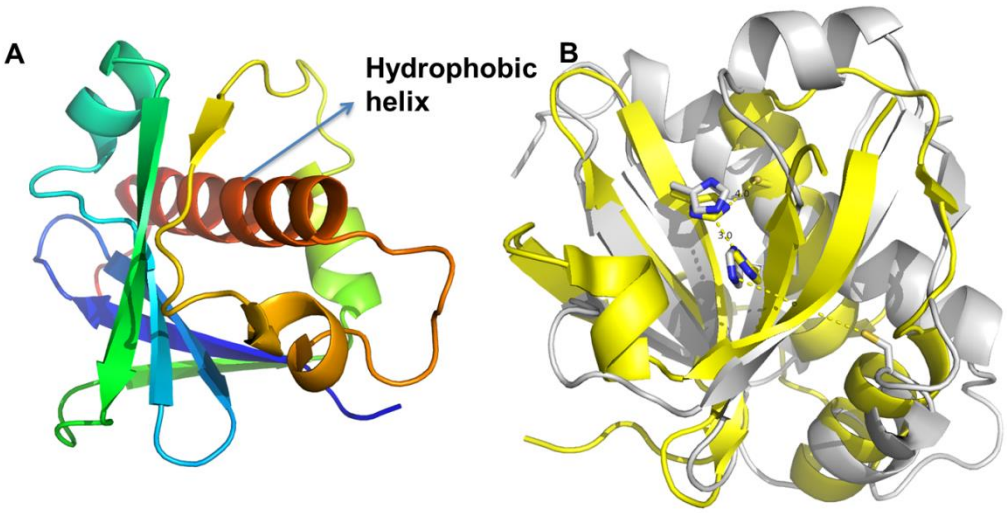

Fig. 7.8 Structural analysis of LV 2A2. (A) Overall structure of LV 2A2, a rainbow colored cartoon representation with N-terminal region colored in blue and C-terminal region colored in red; (B) Overlay of LV 2A2 (gray) and AdPLA (yellow).

In addition, we determined the structure of HPeV3 2A, which shows a very high similarity with LV 2A2 with a root mean square deviation (r.m.s.d) of 1.76 Å for 125 Cα atom pairs (Fig. 7.9). The differences include a loop of seven extra residues at the N-terminus, a ten-residue extension of the helix at the C-terminus in comparison with LV 2A2, and a different conformation of the region connecting the N-domain with the C-domain. Unlike the two molecules forming an asymmetric unit in LV 2A2, the structures of chain A and chain B vary slightly with a root mean square deviation (r.m.s.d) of 1.8 Å. The largest conformational differences between the molecules are

in the orientation of the C-terminal helix and the region connecting the N-domain with C-domain, which are circled and highlighted by black dashed lines in Fig. 7.9.

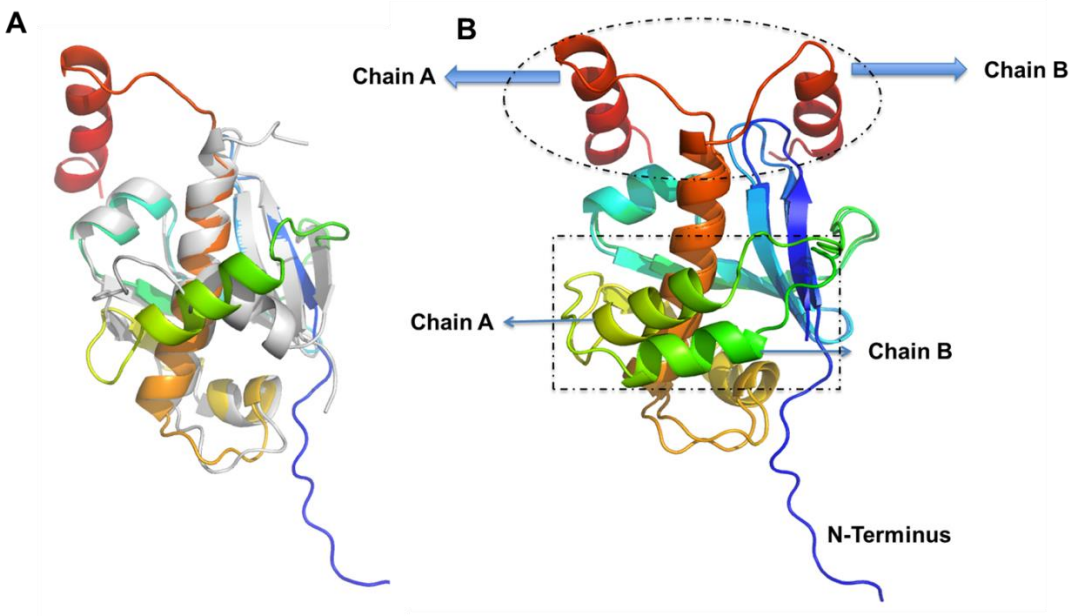

Fig. 7.9 Structural analysis of HPeV3 2A. (A). Overlay of LV 2A2 (gray) and HPeV3 2A (rainbow colored from blue N-terminus to red C-terminus); (B). Overlay of Chain A and Chain B molecules of HPeV3 2A (rainbow colored from blue N-terminus to red C-terminus), largest differences have been marked.

Like LV 2A2, HPeV3 2A does not form a potential catalytic triad, which suggests that what we observe is an inactive conformation. By overlaying the piconaviral 2As and AdPLA structures it would appear that AdPLA has refolded from one "key point" to form the active conformation (Fig. 7.10). What factors can trigger this

conformational switch would be very important to understand in order to uncover the roles of 2As in viral infection.

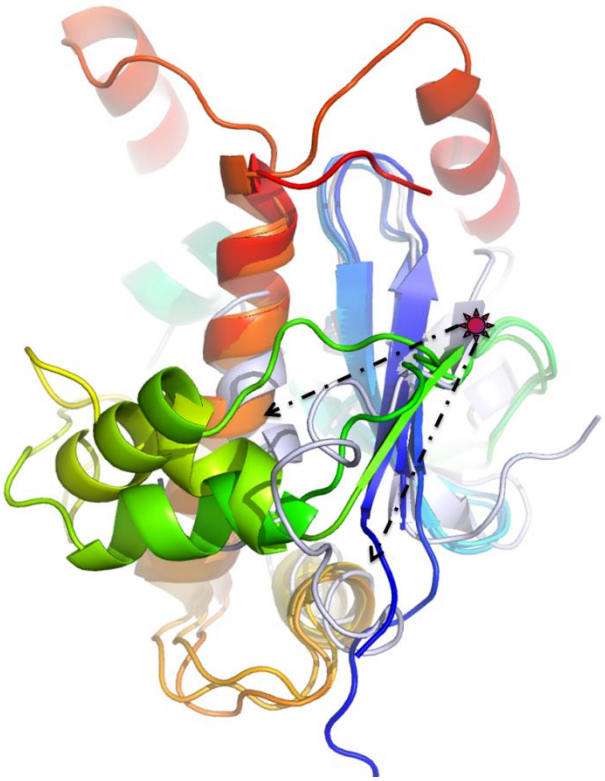

Fig. 7.10 Overlay of LV 2A2, Chain A, Chain B molecules of HPeV3 2A and AdPLA. AdPLA is drawn in grey whilst the 2As of LV and HPeV are shown in rainbow colors.

7.5 Can 2As from the parechovirus family exhibit phospholipase activity?

Since the structures of 2As from the parechovirus family are predicted to be in inactive conformations, we examined the activity of LV 2A2 using a boron-dipyrromethene (BODIPY)-labeled fluoro-genic phospholipid substrate, 1-O-(6-BODIPY 558/568-aminohexyl)-2-BODIPY FL C5-sn-glycerol-3-phosphocholine (BODIPY PC-A2; A10072, Invitrogen) to measure the rate of reaction [206, 207]. Release of the BODIPY FL pentanoic acid acyl chain from sn-2 of BODIPY PC-A2 results in an increase in the fluorescence signal (excitation, 488 nm; emission, 515 nm) due to decreased intramolecular quenching by fluorescence resonance energy transfer (FRET) of the BODIPY 558/568 dye attached at the sn-1 position. As expected that LV 2A2 did not show phospholipase activity in the suggested buffer solutions (Fig. 7.11).

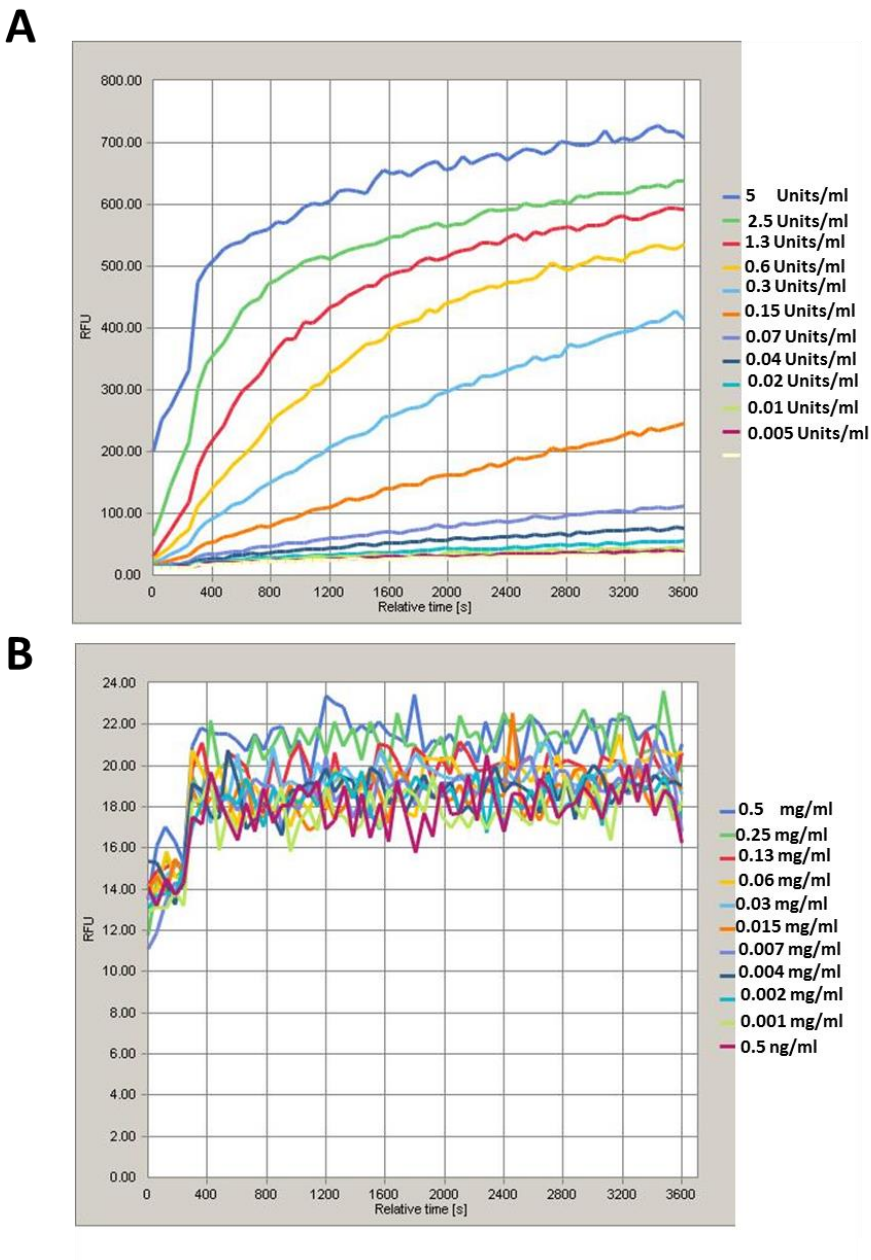

Fig. 7.11 Phospholipase activity of LV 2A2. BODIPY PC-A2 was used to measure the rate of reaction. The 488/515 nm fluorescence signal of liposomes containing the same concentration of BODIPY PC-A2 substrate with a series of concentration dilutions of PLA2 (A) and LV 2A2 (B) was recorded for 50 min to monitor the

background emission (PLA2: 0.005 to 5 units/ml in 2-fold series dilution; LV 2A2: 0.5 ng/ml to 0.5 mg/ml in 2-fold series dilution).

7.6 What can trigger 2A conformational changes to activate phospholipase activity?

To determine whether the oligomerization of LV 2A2 was a contributing factor, we carried out an analytical ultracentrifugation (AUC) assay. This revealed that only the dimer exists in solution (Fig. 7.12). The calculated molecular weight of LV 2A2 according to the sedimentation coefficient is 31.65 kDa and the theoretical molecular weight of dimeric 2A2 is 30.8 kDa. Based on our structural analysis, the C-terminal hydrophobic helices stabilize each other in forming the dimer with the contact area of ~550 $Å^2$ calculated by PISA [154] (Fig. 7.12). Together with all the structural information and biochemical data, we speculated that the C-terminal hydrophobic helix may affect protein refolding. If the C-terminal hydrophobic helix is removed or inserted into a membrane, can the 2As adopt an active refolded configuration?

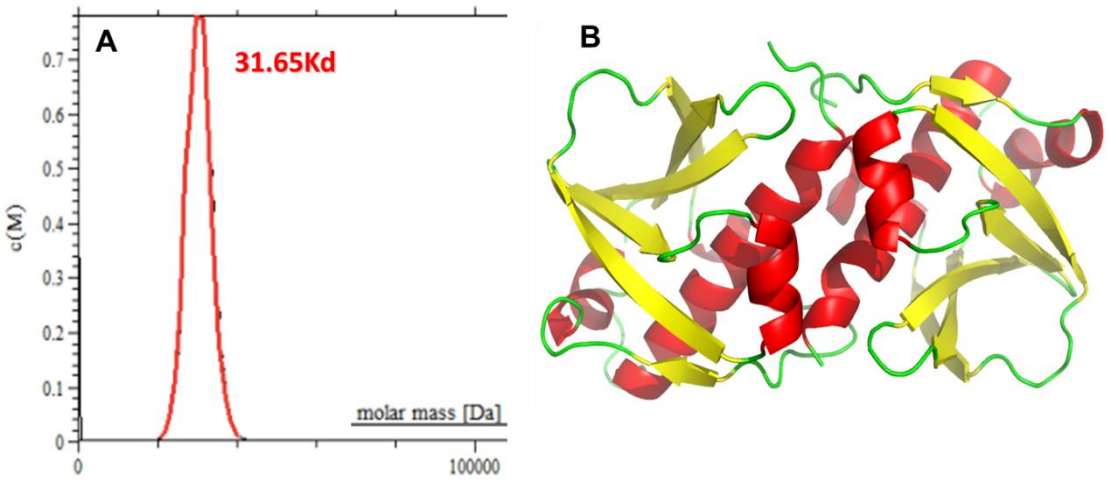

Fig. 7.12 AUC analysis of LV 2A2 and the dimer structure of LV 2A2. (A) LV 2A2 exists as dimers in solution. (B) α-helices, β-sheets and loops are colored in red, yellow and green respectively.

Low pH plays a key role in some picornavirus infections. To explore if pH could trigger the conformational changes of 2As, we used the thermal stability shift assay under a series of pHs ranging from pH 4 to pH 10 and different salt concentrations. Fig. 7.13 shows that LV 2A2 exhibits good stability at pH 7.2-8.8 but poor stability at low pH. It was noted that the melting temperature of 2A at pH 4.4 was significantly higher than the one at pH 4.8 and 5.2, which indicated that 2A might present an alternative structure at pH 4.4. To determine further if pH affects the structure, near-ultraviolet circular dichroism spectra was used. Consistent with the thermal stability results, conformational changes were induced under pH 4.5 (Fig. 7.14).

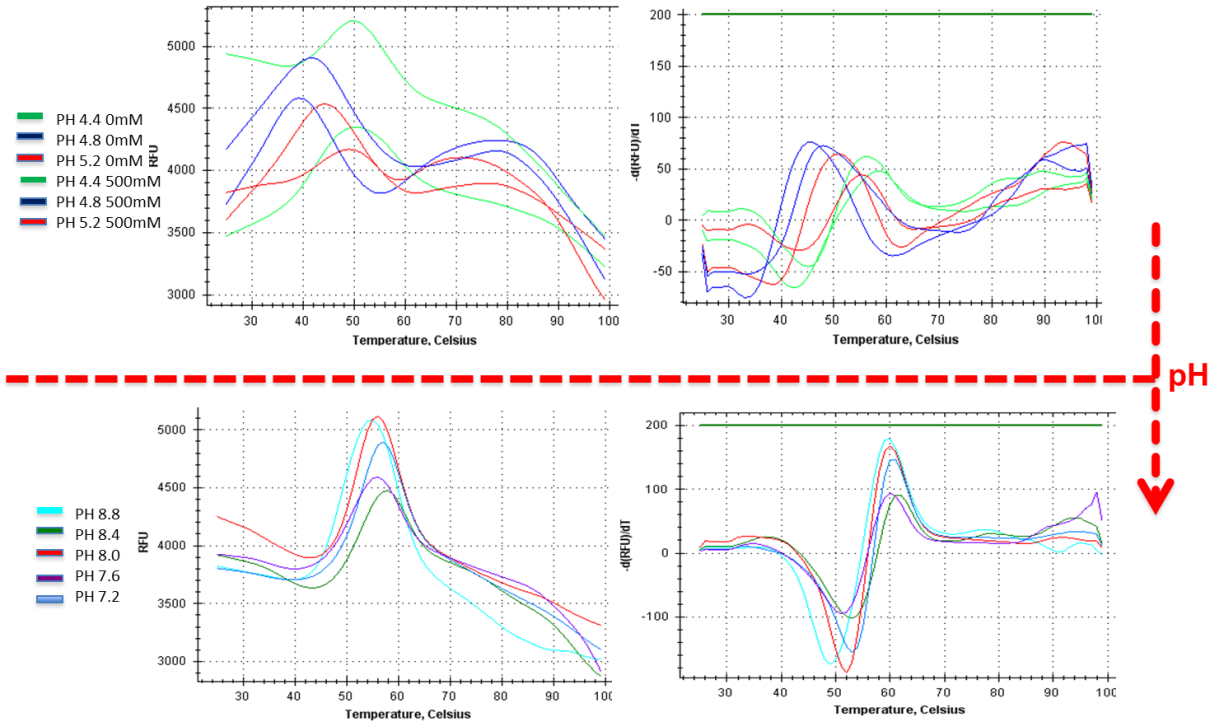

Fig. 7.13 Thermal stability analysis of LV 2A2 under various buffer solutions.

The colored curves stands for the thermal shift assay results of indicated concentrations of LV 2A2 under indicated pHs.

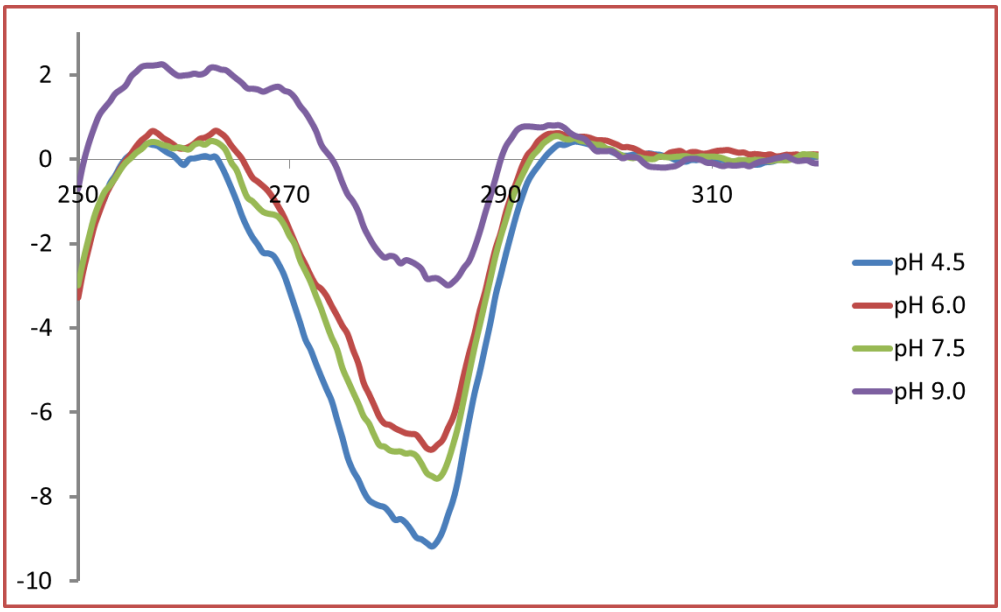

Fig. 7.14 Near-ultraviolet circular dichroism spectra analysis of LV 2A2. Blue, red, green and purple curves represent light absorption values of LV 2A2 under various pH conditions at indicated wavelengths.

7.7 Truncation of LV 2A2 and structure determination of LV 2A2 under low pH

Since the C-terminal hydrophobic helix might affect the refolding of 2A, removal of the hydrophobic helix seemed worthwhile. Three truncated constructs (Table. 7.1) were designed, cloned, expressed, purified and crystallized (Fig. 7.15). Unlike full-length 2A2, the truncated 2A2 with a C-terminal 6xHis tag became more insoluble and could not be concentrated for crystallization. Finally, we obtained soluble truncated 2A2 (removal of GST tag) from pGEX-6p-1 vector, which was used for setting up crystallizations (Fig. 7.15). Small needle crystals were obtained

under the screening conditions of 25% v/v tert-Butanol, 0.1 M Tris-Hcl pH 8.5. Crystallization optimization is ongoing.

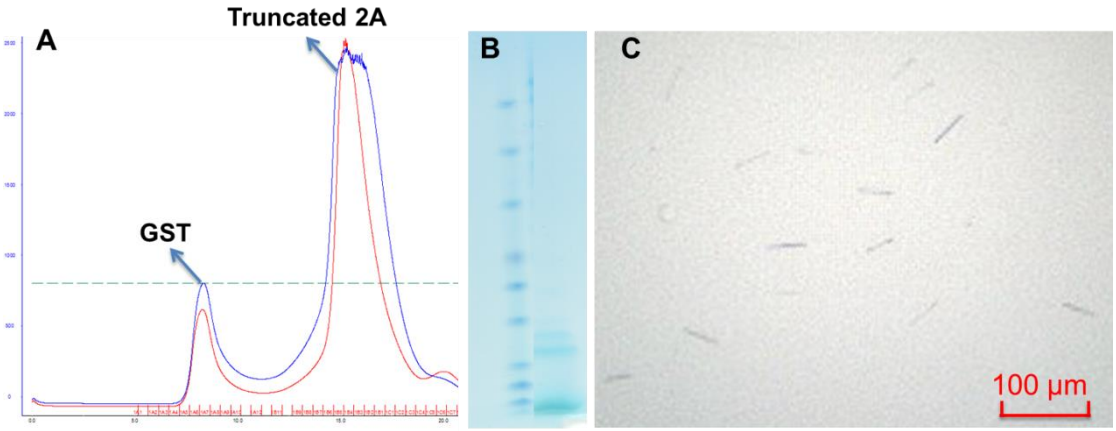

Fig. 7.15 Expression, purification and crystallization of the truncated LV 2A2. (A) Gel filtration peaks of GST and truncated LV 2A2, (B) SDS-PAGE gel for truncated LV 2A2 after purified by gel filtration, (C) Needle-shaped crystals of truncated LV 2A2.

7.8 Discussion

Sequence and structure similarities of the 2As in parechoviruses with PLA2 suggest that the 2A may exhibit phospholipase activity in the viral entry process in particular environments. Unexpectedly, the active residues of the distinctive His-His-Cys catalytic triad in PLA2 are not in the same configuration as observed in our 2A structures, since the Cys, one of catalytic residues is pulled to the other side of the C-terminal helix with a distance of 11 Å from the His (Fig. 7.8) (this is referred to as the inactive conformation). Thus 2As are not capable of performing phospholipase activity, which was verified by a Fluorogenic Phospholipase A2 Assay. Structures of the 3 homologs of 2As (LV 2A2, HPeV3 2A and SEBV1 2A) exhibit a high degree of conformational plasticity at the C-terminus where a couple of hydrophobic helices are located (Fig. 7.9). We speculate some unknown factors might trigger conformational changes to form a His-His-Cys catalytic triad, exposing the hydrophobic helices and exhibiting phospholipase activity. However, up to now 2A has not been detected from viral particles by ELISA/western blot and also there is no experimental evidence to demonstrate that 2A is a structural protein. Therefore more experimental evidence is needed to support this speculation.

Chapter 8
Final comments and future directions

8.1 Summary

The *Picornaviridae* is one of the most genetically diverse families of positive-sense single stranded RNA viruses, and is composed of at least 33 genera, including *Enterovirus*, *Cardiovirus*, *Aphthovirus*, *Kobuvirus*, *Hepatovirus* and *Parechovirus*, which are responsible for some of the most common and debilitating illnesses affecting humans and animals worldwide. In the past two decades, structural and functional studies of picornaviruses have mainly focused on *Enteroviruses*, *Aphthoviruses* and *Cardioviruses*, including PV [9], HRV [27], EV71 [20], FMDV [28] *etc*. However, understanding of the structural details and molecular basis of viral entry for other genera are quite limited. In 2015, Wang X *et al.* [25] reported the structure of HAV, the first structure of Group 3.

Here I have determined by cryo-EM the atomic structure of the first member of the genus of *Parechovirus*, Ljungan virus, which has been linked to diabetes and birth defects in humans. The 3.78 Å resolution structure showed some remarkable features, including an RNA binding motif at the N-terminus of VP3, which associates with the RNA genome, allowing us to model some 12% of the viral genome, and a major protuberance on the outer surface of the virus, which was due to the extended C-terminus on VP1. These structural features presumably reflect functional adaptations, and presumably reflect different solutions to problems of cell attachment and genome encapsidation explored early in the evolution of

picornaviruses.

Afterwards, using cryo-EM, the atomic structure of Aichi virus, an unusual and poorly characterized picornavirus, that can cause severe gastroenteritis and deaths in children below the age of five years, was determined at the resolution of 3.68 Å. This first high-resolution structure for a *kobuvirus* was intermediate between those of the enteroviruses and cardioviruses, with a shallow, narrow depression bounded by the prominent VP0 CD loops (linking the C and D strands of the β-barrel), replacing the depression known as the canyon, frequently the site of receptor attachment in enteroviruses. VP0 was not cleaved to form VP2 and VP4 but formed extended unique structures on the inside of the capsid, with VP2 retaining the classical intra-pentamer organization seen in most other picornaviruses. On the outer surface a polyproline helix structure, unique amongst picornaviruses was displayed at the C-terminus of VP1, corresponding to the position where integrin binding motifs are found in some other picornaviruses. A peptide corresponding to this polyproline motif somewhat attenuated virus infectivity suggesting a role in attachment to a cellular receptor, which is helpful to identify the cellular receptor for AiV.

The HAV particle is extremely physically robust, and the recently solved structure by our lab gave no hints as to where the reported cellular receptor (TIM-1) binds or how the particle can be destabilized to release the genome and initiate infection. In

collaboration with Dr. Xiangxi Wang, we identified one potent neutralizing mAb against HAV infection, named R10, whose Fab portion dramatically destabilized full HAV particles. Furthermore, R10 prevented HAV attachment to the cell surface by blocking the interactions between HAV and TIM-1 and was able to displace virus that had already bound to the cell receptor. Given the ability of the R10 Fab to destabilize HAV and to block the binding of HAV to TIM-1, the binding sites on HAV of TIM-1 and R10 may overlap partially or fully. The high-resolution cryo-EM structure of the complex of HAV with R10 Fab revealed the atomic details of antibody binding and pointed to a receptor recognition site at the pentamer interface. These results, together with our experimental observations demonstrated that the R10 Fab destabilized the capsid, suggesting the use of a receptor mimic mechanism to neutralize virus infection.

EV71 and a second enterovirus, CAV16, are, taken together, the dominant cause of hand, foot and mouth disease virus in East Asia. Although an EV71 vaccine has been successfully developed using inactivated virus, it does not provide protection against CVA16 infection. A CVA16 vaccine or a bivalent vaccine against both viruses is therefore urgently needed to combat HFMD. I used the Bac-to-Bac baculovirus expression system to express the recombinant CVA16 VLP, which exhibited similar immunogenicity to inactivated CVA16 full particles. In line with the immunogenicity results, the structure of CVA16 VLP is antigenically identical to the CVA16 mature

particle. Therefore, the CVA16 VLP could be used as vaccine antigen. The substantial overlap of antigenic sites between EV71 and CVA16, which are nonetheless not cross-reactive suggests that a bi-valent recombinant VLP vaccine might be a good way to produce a broadly effective, safe HFMDV vaccine.

Apart from the structural and functional studies of viral particles, I also reported some progress on the characterization of 2As from human parechovirus, Ljungan virus and Sebokele virus. I successfully expressed, purified, crystallized and determined the structures of the above three 2A proteins in the past 3 years. Although the structures of the three 2A proteins share high similarity with PLA2, the functions of the three 2As need to be explored further.

8.2 Future plans

The experiments described in this thesis raise a number of further questions about viral entry and assembly of the *Kobuvirus*, *Hepatovirus* and *Parechovirus* genera: 1) What roles might the LV VP1 C-terminus play? Is it related to receptor(s) recognition? 2) What are the cellular receptor(s) for AiV? How does the poly proline motif interact with the potential receptor? 3) Where does TIM-1 bind to HAV? How does the extremely stable HAV virion uncoat? 4) What are the functions of the 2A proteins of Parechovirus? Are they essential for parechovirus entry? Regarding the above scientific questions, future experiments aimed at shedding further light on

these questions are outlined below:

- Deletion the VP1 C-terminal region in LV genome using the reverse genetics technique might provide insights into its biological functions. Of course, the deletion might be lethal. However, the fact that the VP1 C-terminus is poorly ordered and best seen in a lower resolution reconstruction at the external surface reveals it is not involved in the interactions with the surrounding subunits. The experimental observations of the behaviour of LV deletion mutants might demonstrate my speculation that the deletion of the VP1 C-terminus might not affect viral assembly, but possibly abort viral infection by blocking its ability to enter into the host cells.
- Since the poly proline motif plays a role in cell attachment, it may be possible to utilize this motif to fish out the putative receptors of AiV. Recombinant expression of the poly proline motif with an His or GST tag is helpful to identify the putative receptors by a pull-down assay. Briefly, 1 L host cells (sensitive to AiV infection, eg. vero cells) pellets will be solubilized for 1 h at 4 ℃ with PBS buffer containing protease inhibitor tablets (complete protease inhibitor cocktail tablets, Roche) and 1.5% DM (b-decylmaltoside). Nuclei and other unsolubilized material can be removed by centrifugation and the supernatant incubated with the

recombinant poly-proline with a GST tag bound to sepharose (Amersham Biosciences). After 3–4 h, wash the matrix with PBS, pH 7, and 0.125% DM, and elute the target proteins by elution buffer (PBS pH 7 and 0.125% DM and 10 mM GSH). Run an SDS-PAGE gel and identify the potential poly proline motif binders by Mass Spec.

- Elucidation of cryo-EM structures of HAV full particles in complex with TIM-1 is the priority for future work to clarify the entry mechanism of HAV. Large-scale production of HAV and recombinant expression of TIM-1 Ig V domain with a high purity have been done already in this thesis, and the high resolution structures of HAV and TIM-1 are ready as well. It will be required to optimize the incubation conditions, including temperature, pH, time and cross-linking *etc* to obtain homogeneous and stable complexes and determine the complex structure by cryo-EM.
- The functions of 2As from the *Parechovirus* genus are still unclear, even though it is now clear that they share structural similarities with PLA2. Hopefully, in collaboration with Prof. Anastassis Perrakis and Prof. Thijin R. Brummelkamp, more experiments including reverse genetics and viral related assays will be performed to elucidate their functions.

References

1. Ganem, D. and R.J. Schneider, *Hepadnaviridae: the viruses and their replication.* Fields virology, 2001. **2**: p. 2923-2969.
2. Racaniello, V.R., *Picornaviridae: the viruses and their replication.* Fields virology, 2001.
3. Schmidt, N.J., E.H. Lennette, and H.H. Ho, *An apparently new enterovirus isolated from patients with disease of the central nervous system.* Journal of Infectious Diseases, 1974. **129**(3): p. 304-309.
4. Jiang, P., et al., *Picornavirus morphogenesis.* Microbiol Mol Biol Rev, 2014. **78**(3): p. 418-37.
5. Carstens, E., *Ratification vote on taxonomic proposals to the International Committee on Taxonomy of Viruses (2009).* Archives of virology, 2010. **155**(1): p. 133-146.
6. Solomon, T., et al., *Virology, epidemiology, pathogenesis, and control of enterovirus 71.* The Lancet Infectious Diseases, 2010. **10**(11): p. 778-790.
7. Tuthill, T.J., et al., *Picornaviruses*, in *Cell Entry by Non-Enveloped Viruses*. 2010, Springer. p. 43-89.
8. Johansson, S., et al., *Molecular analysis of three Ljungan virus isolates reveals a new, close-to-root lineage of the Picornaviridae with a cluster of two unrelated 2A proteins.* Journal of virology, 2002. **76**(17): p. 8920-8930.
9. Hogle, J., M. Chow, and D. Filman, *Three-dimensional structure of poliovirus at 2.9 A resolution.* Science, 1985. **229**(4720): p. 1358-1365.
10. Rossmann, M.G., Y. He, and R.J. Kuhn, *Picornavirus–receptor interactions.* Trends in microbiology, 2002. **10**(7): p. 324-331.
11. Basavappa, R., et al., *Role and mechanism of the maturation cleavage of VP0 in poliovirus assembly: structure of the empty capsid assembly intermediate at 2.9 Å resolution.* Protein Science, 1994. **3**(10): p. 1651-1669.
12. Norder, H., et al., *Picornavirus non-structural proteins as targets for new anti-virals with broad activity.* Antiviral Res, 2011. **89**(3): p. 204-18.
13. Etchison, D., et al., *Inhibition of HeLa cell protein synthesis following poliovirus infection correlates with the proteolysis of a 220,000-dalton polypeptide associated with eucaryotic initiation factor 3 and a cap binding protein complex.* J Biol Chem, 1982. **257**(24): p. 14806-10.
14. Teterina, N.L., et al., *Testing the modularity of the N-terminal amphipathic helix conserved in picornavirus 2C proteins and hepatitis C NS5A protein.* Virology, 2006. **344**(2): p. 453-67.
15. Guan, H., et al., *Crystal structure of 2C helicase from enterovirus 71.* Sci Adv, 2017. **3**(4): p. e1602573.
16. Cheah, K.C., L.E. Leong, and A.G. Porter, *Site-directed mutagenesis suggests close functional relationship between a human rhinovirus 3C cysteine protease and cellular trypsin-like serine proteases.* J Biol Chem, 1990. **265**(13): p. 7180-7.

17. Sankar, S. and A.G. Porter, *Point mutations which drastically affect the polymerization activity of encephalomyocarditis virus RNA-dependent RNA polymerase correspond to the active site of Escherichia coli DNA polymerase I.* J Biol Chem, 1992. **267**(14): p. 10168-76.
18. Fry, E.E., D.I. Stuart, and D.J. Rowlands, *The structure of foot-and-mouth disease virus.* Curr Top Microbiol Immunol, 2005. **288**: p. 71-101.
19. Tuthill, T.J., et al., *Equine rhinitis A virus and its low pH empty particle: clues towards an aphthovirus entry mechanism?* PLoS Pathog, 2009. **5**(10): p. e1000620.
20. Wang, X., et al., *A sensor-adaptor mechanism for enterovirus uncoating from structures of EV71.* Nature Structural & Molecular Biology, 2012. **19**(4): p. 424-429.
21. Ren, J., et al., *Picornavirus uncoating intermediate captured in atomic detail.* Nature communications, 2013. **4**.
22. Sun, Y., et al., *An open conformation determined by a structural switch for 2A protease from coxsackievirus A16.* Protein & cell, 2013. **4**(10): p. 782-792.
23. Logan, D., et al., *Structure of a major immunogenic site on foot-and-mouth disease virus.* 1993.
24. Verdaguer, N., et al., *Structure of the major antigenic loop of foot-and-mouth disease virus complexed with a neutralizing antibody: direct involvement of the Arg-Gly-Asp motif in the interaction.* The EMBO Journal, 1995. **14**(8): p. 1690.
25. Wang, X., et al., *Hepatitis A virus and the origins of picornaviruses.* nature, 2014.
26. Stamatakis, A., P. Hoover, and J. Rougemont, *A rapid bootstrap algorithm for the RAxML Web servers.* Syst Biol, 2008. **57**(5): p. 758-71.
27. Kim, S., et al., *Crystal structure of human rhinovirus serotype 1A (HRV1A).* Journal of molecular biology, 1989. **210**(1): p. 91-111.
28. Fry, E.E., et al., *The structure and function of a foot-and-mouth disease virus-oligosaccharide receptor complex.* EMBO J, 1999. **18**(3): p. 543-54.
29. Zhu, L., et al., *Structure of Ljungan virus provides insight into genome packaging of this picornavirus.* Nature communications, 2015. **6**.
30. Ren, J., et al., *Structures of coxsackievirus A16 capsids with native antigenicity: implications for particle expansion, receptor binding, and immunogenicity.* Journal of virology, 2015. **89**(20): p. 10500-10511.
31. Rossmann, M.G., et al., *Structure of a human common cold virus and functional relationship to other picornaviruses.* nature, 1985. **317**(6033): p. 145-53.
32. Logan, D., et al., *Structure of a major immunogenic site on foot-and-mouth disease virus.* nature, 1993. **362**(6420): p. 566-8.
33. Greve, J.M., et al., *The major human rhinovirus receptor is ICAM-1.* Cell, 1989. **56**(5): p. 839-847.
34. Hofer, F., et al., *Members of the low density lipoprotein receptor family mediate cell entry of a minor-group common cold virus.* Proceedings of the National Academy of Sciences, 1994. **91**(5): p. 1839-1842.
35. Jackson, T., et al., *The epithelial integrin αvβ6 is a receptor for foot-and-mouth disease virus.* Journal of virology, 2000. **74**(11): p. 4949-4956.

36. Nishimura, Y., et al., *Human P-selectin glycoprotein ligand-1 is a functional receptor for enterovirus 71.* Nature medicine, 2009. **15**(7): p. 794-797.
37. Yamayoshi, S., et al., *Scavenger receptor B2 is a cellular receptor for enterovirus 71.* Nature medicine, 2009. **15**(7): p. 798-801.
38. Bergelson, J.M., et al., *Decay-accelerating factor (CD55), a glycosylphosphatidylinositol-anchored complement regulatory protein, is a receptor for several echoviruses.* Proceedings of the National Academy of Sciences, 1994. **91**(13): p. 6245-6248.
39. Silberstein, E., et al., *Alteration of hepatitis A virus (HAV) particles by a soluble form of HAV cellular receptor 1 containing the immunoglobulin-and mucin-like regions.* Journal of virology, 2003. **77**(16): p. 8765-8774.
40. Bochkov, Y.A., et al., *Cadherin-related family member 3, a childhood asthma susceptibility gene product, mediates rhinovirus C binding and replication.* Proc Natl Acad Sci U S A, 2015. **112**(17): p. 5485-90.
41. Bergelson, J., *Receptors.* The picornaviruses, 2010: p. 73-86.
42. Mendelsohn, C.L., E. Wimmer, and V.R. Racaniello, *Cellular receptor for poliovirus: molecular cloning, nucleotide sequence, and expression of a new member of the immunoglobulin superfamily.* Cell, 1989. **56**(5): p. 855-865.
43. Carson, S.D., *Receptor for the group B coxsackieviruses and adenoviruses: CAR.* Reviews in medical virology, 2001. **11**(4): p. 219-226.
44. Dang, M., et al., *Molecular mechanism of SCARB2-mediated attachment and uncoating of EV71.* Protein & cell, 2014. **5**(9): p. 692-703.
45. Olson, N.H., et al., *Structure of a human rhinovirus complexed with its receptor molecule*, in *Regulation of Gene Expression in Animal Viruses*. 1993, Springer. p. 1-12.
46. Rossmann, M.G., et al., *Cell recognition and entry by rhino-and enteroviruses.* Virology, 2000. **269**(2): p. 239-247.
47. Williams, Ç.H., et al., *Integrin αvβ6 is an RGD-dependent receptor for coxsackievirus A9.* Journal of virology, 2004. **78**(13): p. 6967-6973.
48. Schober, D., et al., *Major and minor receptor group human rhinoviruses penetrate from endosomes by different mechanisms.* J Virol, 1998. **72**(2): p. 1354-64.
49. Yamayoshi, S., et al., *Functional comparison of SCARB2 and PSGL1 as receptors for enterovirus 71.* Journal of virology, 2013. **87**(6): p. 3335-3347.
50. Patel, K.P. and J.M. Bergelson, *Receptors identified for hand, foot and mouth virus.* Nature medicine, 2009. **15**(7): p. 728-729.
51. Pelkmans, L. and A. Helenius, *Insider information: what viruses tell us about endocytosis.* Current Opinion in Cell Biology, 2003. **15**(4): p. 414-422.
52. Pelkmans, L., et al., *Caveolin-stabilized membrane domains as multifunctional transport and sorting devices in endocytic membrane traffic.* Cell, 2004. **118**(6): p. 767-780.
53. Leong, K.L.J., M.M.-L. Ng, and J.J.H. Chu, *The essential role of clathrin-mediated endocytosis in the infectious entry of human enterovirus 71.* Journal of Biological Chemistry, 2011. **286**(1): p. 309-321.

54. Lin, Y.-W., et al., *Human SCARB2-mediated entry and endocytosis of EV71.* PLoS One, 2012. **7**(1): p. e30507.
55. Arita, M., et al., *Interaction of poliovirus with its purified receptor and conformational alteration in the virion.* Journal of virology, 1998. **72**(5): p. 3578-3586.
56. Milstone, A.M., et al., *Interaction with coxsackievirus and adenovirus receptor, but not with decay-accelerating factor (DAF), induces A-particle formation in a DAF-binding coxsackievirus B3 isolate.* J Virol, 2005. **79**(1): p. 655-60.
57. Prchla, E., et al., *Uncoating of human rhinovirus serotype 2 from late endosomes.* J Virol, 1994. **68**(6): p. 3713-23.
58. Kotecha, A., et al., *Structure-based energetics of protein interfaces guides foot-and-mouth disease virus vaccine design.* Nature structural & molecular biology, 2015. **22**(10): p. 788-794.
59. Seitsonen, J.J., et al., *Structural analysis of coxsackievirus A7 reveals conformational changes associated with uncoating.* J Virol, 2012. **86**(13): p. 7207-15.
60. Bostina, M., et al., *Poliovirus RNA is released from the capsid near a twofold symmetry axis.* Journal of virology, 2011. **85**(2): p. 776-783.
61. Strauss, M., et al., *RNA transfer from poliovirus 135S particles across membranes is mediated by long umbilical connectors.* Journal of virology, 2013. **87**(7): p. 3903-3914.
62. Levy, H.C., et al., *Catching a virus in the act of RNA release: a novel poliovirus uncoating intermediate characterized by cryo-electron microscopy.* J Virol, 2010. **84**(9): p. 4426-41.
63. Fricks, C.E. and J.M. Hogle, *Cell-induced conformational change in poliovirus: externalization of the amino terminus of VP1 is responsible for liposome binding.* Journal of virology, 1990. **64**(5): p. 1934-1945.
64. Feil, S.C., et al., *An Orally Available 3-Ethoxybenzisoxazole Capsid Binder with Clinical Activity against Human Rhinovirus.* ACS Med Chem Lett, 2012. **3**(4): p. 303-7.
65. De Palma, A.M., et al., *Selective inhibitors of picornavirus replication.* Med Res Rev, 2008. **28**(6): p. 823-84.
66. De Colibus, L., et al., *More-powerful virus inhibitors from structure-based analysis of HEV71 capsid-binding molecules.* Nature structural & molecular biology, 2014.
67. Rao, A.L., *Genome packaging by spherical plant RNA viruses.* Annu Rev Phytopathol, 2006. **44**: p. 61-87.
68. Ni, P. and C. Cheng Kao, *Non-encapsidation activities of the capsid proteins of positive-strand RNA viruses.* Virology, 2013. **446**(1-2): p. 123-32.
69. Casjens, S.R., *The DNA-packaging nanomotor of tailed bacteriophages.* Nat Rev Microbiol, 2011. **9**(9): p. 647-57.
70. Ford, R.J., et al., *Sequence-specific, RNA-protein interactions overcome electrostatic barriers preventing assembly of satellite tobacco necrosis virus coat protein.* J Mol Biol, 2013. **425**(6): p. 1050-64.
71. Sasaki, J. and K. Taniguchi, *The 5'-end sequence of the genome of Aichi virus, a picornavirus, contains an element critical for viral RNA encapsidation.* J Virol, 2003. **77**(6): p. 3542-8.
72. Liu, Y., et al., *Direct interaction between two viral proteins, the nonstructural protein 2C and*

the capsid protein VP3, is required for enterovirus morphogenesis. PLoS Pathog, 2010. **6**(8): p. e1001066.

73. Casal, J.I., *Use of parvovirus-like particles for vaccination and induction of multiple immune responses.* Biotechnol Appl Biochem, 1999. **29 (Pt 2)**: p. 141-50.
74. Roy, P., *Genetically engineered particulate virus-like structures and their use as vaccine delivery systems.* Intervirology, 1996. **39**(1-2): p. 62-71.
75. Buonaguro, L., et al., *Baculovirus-derived human immunodeficiency virus type 1 virus-like particles activate dendritic cells and induce ex vivo T-cell responses.* J Virol, 2006. **80**(18): p. 9134-43.
76. Chung, Y.C., et al., *Expression, purification and characterization of enterovirus-71 virus-like particles.* World J Gastroenterol, 2006. **12**(6): p. 921-7.
77. Gong, M., et al., *Cryo-electron microscopy study of insect cell-expressed enterovirus 71 and coxsackievirus a16 virus-like particles provides a structural basis for vaccine development.* J Virol, 2014. **88**(11): p. 6444-52.
78. Lin, Y.J., et al., *Expression of enterovirus 71 virus-like particles in transgenic enoki (Flammulina velutipes).* Appl Microbiol Biotechnol, 2015. **99**(16): p. 6765-74.
79. Lin, S.Y., et al., *Enhanced enterovirus 71 virus-like particle yield from a new baculovirus design.* Biotechnol Bioeng, 2015. **112**(10): p. 2005-15.
80. Liu, Q., et al., *A virus-like particle vaccine for coxsackievirus A16 potently elicits neutralizing antibodies that protect mice against lethal challenge.* Vaccine, 2012. **30**(47): p. 6642-8.
81. Xue, W., et al., *Immunogenicity of a modified-live virus vaccine against bovine viral diarrhea virus types 1 and 2, infectious bovine rhinotracheitis virus, bovine parainfluenza-3 virus, and bovine respiratory syncytial virus when administered intranasally in young calves.* Vaccine, 2010. **28**(22): p. 3784-92.
82. *Imported vaccine-associated paralytic poliomyelitis--United States, 2005.* MMWR Morb Mortal Wkly Rep, 2006. **55**(4): p. 97-9.
83. Porta, C., et al., *Rational engineering of recombinant picornavirus capsids to produce safe, protective vaccine antigen.* PLoS Pathog, 2013. **9**(3): p. e1003255.
84. Zhu, F.C., et al., *Efficacy, safety, and immunology of an inactivated alum-adjuvant enterovirus 71 vaccine in children in China: a multicentre, randomised, double-blind, placebo-controlled, phase 3 trial.* Lancet, 2013. **381**(9882): p. 2024-32.
85. Zhu, F.C., et al., *Immunogenicity and safety of an enterovirus 71 vaccine in healthy Chinese children and infants: a randomised, double-blind, placebo-controlled phase 2 clinical trial.* Lancet, 2013. **381**(9871): p. 1037-45.
86. Walter, T.S., et al., *A procedure for setting up high-throughput nanolitre crystallization experiments. Crystallization workflow for initial screening, automated storage, imaging and optimization.* Acta Crystallographica Section D: Biological Crystallography, 2005. **61**(6): p. 651-657.
87. Minor, W. and Z. Otwinowski, *HKL2000 (Denzo-SMN) Software Package. Processing of X-ray Diffraction Data Collected in Oscillation Mode.* Methods in Enzymology, Macromolecular Crystallography, Academic Press, New York, 1997.

88. Winter, G., *xia2: an expert system for macromolecular crystallography data reduction.* Journal of applied crystallography, 2010. **43**: p. 186-190.
89. Drenth, J., *Principles of protein X-ray crystallography*. 1999: Springer Verlag.
90. Rossmann, M.G., *Molecular replacement-historical background.* Acta Crystallographica Section D: Biological Crystallography, 2001. **57**(10): p. 1360-1366.
91. Matthews, B.W., *Solvent content of protein crystals.* Journal of molecular biology, 1968. **33**(2): p. 491-497.
92. Kantardjieff, K.A. and B. Rupp, *Matthews coefficient probabilities: Improved estimates for unit cell contents of proteins, DNA, and protein-nucleic acid complex crystals.* Protein Sci, 2003. **12**(9): p. 1865-71.
93. Rossmann, M.G., *The molecular replacement method.* Acta Crystallographica Section A: Foundations of Crystallography, 1990. **46**(2): p. 73-82.
94. Hewat, E.A., et al., *Structure of the complex of an Fab fragment of a neutralizing antibody with foot-and-mouth disease virus: positioning of a highly mobile antigenic loop.* EMBO J, 1997. **16**(7): p. 1492-500.
95. McCoy, A.J., et al., *Phaser crystallographic software.* Journal of applied crystallography, 2007. **40**(4): p. 658-674.
96. Emsley, P. and K. Cowtan, *Coot: model-building tools for molecular graphics.* Acta Crystallographica Section D: Biological Crystallography, 2004. **60**(12): p. 2126-2132.
97. Adams, P.D., et al., *PHENIX: a comprehensive Python-based system for macromolecular structure solution.* Acta Crystallographica Section D: Biological Crystallography, 2010. **66**(2): p. 213-221.
98. Laskowski, R.A., et al., *PROCHECK: a program to check the stereochemical quality of protein structures.* Journal of applied crystallography, 1993. **26**(2): p. 283-291.
99. Larkin, M., et al., *Clustal W and Clustal X version 2.0.* Bioinformatics, 2007. **23**(21): p. 2947-2948.
100. Gouet, P., E. Courcelle, and D.I. Stuart, *ESPript: analysis of multiple sequence alignments in PostScript.* Bioinformatics, 1999. **15**(4): p. 305-308.
101. DeLano, W.L., *The PyMOL molecular graphics system.* 2002.
102. Pettersen, E.F., et al., *UCSF Chimera—a visualization system for exploratory research and analysis.* Journal of computational chemistry, 2004. **25**(13): p. 1605-1612.
103. Milne, J.L., et al., *Cryo-electron microscopy--a primer for the non-microscopist.* FEBS J, 2013. **280**(1): p. 28-45.
104. Orlova, E.V. and H.R. Saibil, *Structural analysis of macromolecular assemblies by electron microscopy.* Chem Rev, 2011. **111**(12): p. 7710-48.
105. Chiu, P.L., et al., *Evaluation of super-resolution performance of the K2 electron-counting camera using 2D crystals of aquaporin-0.* J Struct Biol, 2015. **192**(2): p. 163-73.
106. Li, X., et al., *Electron counting and beam-induced motion correction enable near-atomic-resolution single-particle cryo-EM.* Nature methods, 2013. **10**(6): p. 584-590.
107. Zhu, L., et al., *Structure of human Aichi virus and implications for receptor binding.* Nat Microbiol, 2016. **1**: p. 16150.

108. Ruskin, R.S., Z. Yu, and N. Grigorieff, *Quantitative characterization of electron detectors for transmission electron microscopy.* J Struct Biol, 2013. **184**(3): p. 385-93.
109. Scheres, S.H., *Processing of Structurally Heterogeneous Cryo-EM Data in RELION.* Methods enzymol, 2016. **579**: p. 125-57.
110. Zhang, K., *Gctf: Real-time CTF determination and correction.* J Struct Biol, 2016. **193**(1): p. 1-12.
111. Mindell, J.A. and N. Grigorieff, *Accurate determination of local defocus and specimen tilt in electron microscopy.* J Struct Biol, 2003. **142**(3): p. 334-47.
112. Rohou, A. and N. Grigorieff, *CTFFIND4: Fast and accurate defocus estimation from electron micrographs.* J Struct Biol, 2015. **192**(2): p. 216-21.
113. Kivioja, T., et al., *Local average intensity-based method for identifying spherical particles in electron micrographs.* Journal of structural biology, 2000. **131**(2): p. 126-134.
114. Ludtke, S.J., P.R. Baldwin, and W. Chiu, *EMAN: semiautomated software for high-resolution single-particle reconstructions.* Journal of structural biology, 1999. **128**(1): p. 82-97.
115. Scheres, S.H., *RELION: implementation of a Bayesian approach to cryo-EM structure determination.* Journal of structural biology, 2012. **180**(3): p. 519-530.
116. Scheres, S.H. and S. Chen, *Prevention of overfitting in cryo-EM structure determination.* Nature methods, 2012. **9**(9): p. 853-854.
117. Tang, G., et al., *EMAN2: an extensible image processing suite for electron microscopy.* Journal of structural biology, 2007. **157**(1): p. 38-46.
118. Kucukelbir, A., F.J. Sigworth, and H.D. Tagare, *Quantifying the local resolution of cryo-EM density maps.* Nature methods, 2014. **11**(1): p. 63-65.
119. Brown, A., et al., *Tools for macromolecular model building and refinement into electron cryo-microscopy reconstructions.* Acta Crystallographica Section D-Structural Biology, 2015. **71**: p. 136-153.
120. Afonine, P.V., et al., *Towards automated crystallographic structure refinement with phenix. refine.* Acta Crystallographica Section D: Biological Crystallography, 2012. **68**(4): p. 352-367.
121. Walter, T.S., et al., *A plate-based high-throughput assay for virus stability and vaccine formulation.* J Virol Methods, 2012. **185**(1): p. 166-70.
122. Joffret, M.-L., et al., *Genomic characterization of Sebokele virus 1 (SEBV1) reveals a new candidate species among the genus Parechovirus.* Journal of general virology, 2013. **94**(Pt 7): p. 1547-1553.
123. Benschop, K., et al., *Human parechovirus infections in Dutch children and the association between serotype and disease severity.* Clinical infectious diseases, 2006. **42**(2): p. 204-210.
124. Niklasson, B., et al., *Association of zoonotic Ljungan virus with intrauterine fetal deaths.* Birth Defects Research Part A: Clinical and Molecular Teratology, 2007. **79**(6): p. 488-493.
125. Blixt, M., B. Niklasson, and S. Sandler, *Characterization of β-cell function of pancreatic islets isolated from bank voles developing glucose intolerance/diabetes: An animal model showing features of both type 1 and type 2 diabetes mellitus, and a possible role of the Ljungan virus.* General and comparative endocrinology, 2007. **154**(1): p. 41-47.
126. Digoutte, J., *Sebokele (SEB) Strain: An B 1227 d.* The American Journal of Tropical Medicine

and Hygiene, 1978. **27**(2 Part 2): p. 424-425.

127. Stanway, G. and T. Hyypia, *Parechoviruses.* J Virol, 1999. **73**(7): p. 5249-54.
128. Seitsonen, J., et al., *Interaction of alphaVbeta3 and alphaVbeta6 integrins with human parechovirus 1.* J Virol, 2010. **84**(17): p. 8509-19.
129. Hughes, P.J. and G. Stanway, *The 2A proteins of three diverse picornaviruses are related to each other and to the H-rev107 family of proteins involved in the control of cell proliferation.* J Gen Virol, 2000. **81**(Pt 1): p. 201-7.
130. Panjwani, A., et al., *Capsid protein VP4 of human rhinovirus induces membrane permeability by the formation of a size-selective multimeric pore.* PLoS Pathog, 2014. **10**(8): p. e1004294.
131. Triantafilou, K., et al., *Human parechovirus 1 utilizes integrins alphavbeta3 and alphavbeta1 as receptors.* J Virol, 2000. **74**(13): p. 5856-62.
132. Petrek, M., et al., *CAVER: a new tool to explore routes from protein clefts, pockets and cavities.* BMC Bioinformatics, 2006. **7**: p. 316.
133. Squires, G., et al., *Structure of the Triatoma virus capsid.* Acta Crystallogr D Biol Crystallogr, 2013. **69**(Pt 6): p. 1026-37.
134. Holm, L. and P. Rosenstrom, *Dali server: conservation mapping in 3D.* Nucleic Acids Res, 2010. **38**(Web Server issue): p. W545-9.
135. Tkaczuk, K.L., et al., *Structural and functional insight into the universal stress protein family.* Evolutionary Applications, 2013. **6**(3): p. 434-449.
136. Tolf, C., et al., *Identification of amino acid residues of Ljungan virus VP0 and VP1 associated with cytolytic replication in cultured cells.* Archives of virology, 2009. **154**(8): p. 1271-1284.
137. Larson, S.B., et al., *The RNA of turnip yellow mosaic virus exhibits icosahedral order.* Virology, 2005. **334**(2): p. 245-54.
138. Larson, S.B., et al., *Double-Helical Rna in Satellite Tobacco Mosaic-Virus.* nature, 1993. **361**(6408): p. 179-182.
139. Tang, L., et al., *The structure of pariacoto virus reveals a dodecahedral cage of duplex RNA.* Nat Struct Biol, 2001. **8**(1): p. 77-83.
140. Fisher, A.J. and J.E. Johnson, *Ordered duplex RNA controls capsid architecture in an icosahedral animal virus.* nature, 1993. **361**(6408): p. 176-9.
141. Dong, X.F., et al., *Particle polymorphism caused by deletion of a peptide molecular switch in a quasiequivalent icosahedral virus.* J Virol, 1998. **72**(7): p. 6024-33.
142. Green, T.J., et al., *Common mechanism for RNA encapsidation by negative-strand RNA viruses.* J Virol, 2014. **88**(7): p. 3766-75.
143. Shakeel, S., et al., *Genomic RNA folding mediates assembly of human parechovirus.* Nat Commun, 2017. **8**(1): p. 5.
144. Reuter, G., Á. Boros, and P. Pankovics, *Kobuviruses–a comprehensive review.* Reviews in medical virology, 2011. **21**(1): p. 32-41.
145. Kitajima, M. and C.P. Gerba, *Aichi virus 1: environmental occurrence and behavior.* Pathogens, 2015. **4**(2): p. 256-68.
146. Drexler, J.F., et al., *Aichi virus shedding in high concentrations in patients with acute diarrhea.* Emerg Infect Dis, 2011. **17**(8): p. 1544-8.

147. Sdiri-Loulizi, K., et al., *Aichi virus IgG seroprevalence in Tunisia parallels genomic detection and clinical presentation in children with gastroenteritis.* Clinical and Vaccine Immunology, 2010. **17**(7): p. 1111-1116.

148. Sasaki, J. and K. Taniguchi, *The 5′-end sequence of the genome of Aichi virus, a picornavirus, contains an element critical for viral RNA encapsidation.* Journal of virology, 2003. **77**(6): p. 3542-3548.

149. Lukashev, A.N., et al., *Genetic variation and recombination in Aichi virus.* Journal of general virology, 2012. **93**(Pt 6): p. 1226-1235.

150. Sasaki, J. and K. Taniguchi, *Aichi virus 2A protein is involved in viral RNA replication.* Journal of virology, 2008. **82**(19): p. 9765-9769.

151. Acharya, R., et al., *The three-dimensional structure of foot-and-mouth disease virus at 2.9 Å resolution.* 1989.

152. Krishnaswamy, S. and M.G. Rossmann, *Structural refinement and analysis of Mengo virus.* Journal of molecular biology, 1990. **211**(4): p. 803-844.

153. Monis, P.T., S. Giglio, and C.P. Saint, *Comparison of SYTO9 and SYBR Green I for real-time polymerase chain reaction and investigation of the effect of dye concentration on amplification and DNA melting curve analysis.* Analytical biochemistry, 2005. **340**(1): p. 24-34.

154. Krissinel, E. and K. Henrick, *Inference of macromolecular assemblies from crystalline state.* Journal of molecular biology, 2007. **372**(3): p. 774-797.

155. Adzhubei, A.A., M.J. Sternberg, and A.A. Makarov, *Polyproline-II helix in proteins: structure and function.* Journal of molecular biology, 2013. **425**(12): p. 2100-2132.

156. Berisio, R. and L. Vitagliano, *Polyproline and triple helix motifs in host-pathogen recognition.* Current protein & peptide science, 2012. **13**(8): p. 855.

157. Vermeire, J., et al., *The Nef-infectivity enigma: mechanisms of enhanced lentiviral infection.* Current HIV research, 2011. **9**(7): p. 474-489.

158. Liang, Z., et al., *Establishing China's national standards of antigen content and neutralizing antibody responses for evaluation of enterovirus 71 (EV71) vaccines.* Vaccine, 2011. **29**(52): p. 9668-9674.

159. Solomon, T., et al., *Virology, epidemiology, pathogenesis, and control of enterovirus 71.* Lancet Infect Dis, 2010. **10**(11): p. 778-90.

160. Li, M., Y. Yin, and J. Li, *[An overview of the evolution of EV71 vaccine].* Sheng Wu Yi Xue Gong Cheng Xue Za Zhi, 2010. **27**(4): p. 933-6.

161. Chung, Y.C., et al., *Immunization with virus-like particles of enterovirus 71 elicits potent immune responses and protects mice against lethal challenge.* Vaccine, 2008. **26**(15): p. 1855-62.

162. Li, H.Y., et al., *Virus-like particles for enterovirus 71 produced from Saccharomyces cerevisiae potently elicits protective immune responses in mice.* Vaccine, 2013. **31**(32): p. 3281-7.

163. Lin, Y.L., et al., *Enterovirus type 71 neutralizing antibodies in the serum of macaque monkeys immunized with EV71 virus-like particles.* Vaccine, 2012. **30**(7): p. 1305-12.

164. Brunger, A.T., et al., *Crystallography & NMR system: A new software suite for*

macromolecular structure determination. Acta Crystallographica Section D: Biological Crystallography, 1998. **54**(5): p. 905-921.

165. Li, R., et al., *An inactivated enterovirus 71 vaccine in healthy children.* N Engl J Med, 2014. **370**(9): p. 829-37.
166. Kiener, T.K., et al., *Characterization and specificity of the linear epitope of the enterovirus 71 VP2 protein.* Virol J, 2012. **9**: p. 55.
167. Liu, C.C., et al., *Identification and characterization of a cross-neutralization epitope of Enterovirus 71.* Vaccine, 2011. **29**(26): p. 4362-72.
168. Foo, D.G., et al., *Identification of neutralizing linear epitopes from the VP1 capsid protein of Enterovirus 71 using synthetic peptides.* Virus Res, 2007. **125**(1): p. 61-8.
169. Foo, D.G., et al., *Identification of immunodominant VP1 linear epitope of enterovirus 71 (EV71) using synthetic peptides for detecting human anti-EV71 IgG antibodies in Western blots.* Clin Microbiol Infect, 2008. **14**(3): p. 286-8.
170. Ku, Z., et al., *Neutralizing antibodies induced by recombinant virus-like particles of enterovirus 71 genotype C4 inhibit infection at pre- and post-attachment steps.* PLoS One, 2013. **8**(2): p. e57601.
171. Lee, H., et al., *A strain-specific epitope of enterovirus 71 identified by cryo-electron microscopy of the complex with fab from neutralizing antibody.* J Virol, 2013. **87**(21): p. 11363-70.
172. Plevka, P., et al., *Neutralizing antibodies can initiate genome release from human enterovirus 71.* Proceedings of the National Academy of Sciences of the United States of America, 2014. **111**(6): p. 2134-2139.
173. Drexler, J.F., et al., *Evolutionary origins of hepatitis A virus in small mammals.* Proceedings of the National Academy of Sciences, 2015: p. 201516992.
174. Deinhardt, F., *Prevention of viral hepatitis A: past, present and future.* Vaccine, 1992. **10 Suppl 1**: p. S10-4.
175. Lemon, S.M. and L.N. Binn, *Antigenic relatedness of two strains of hepatitis A virus determined by cross-neutralization.* Infect Immun, 1983. **42**(1): p. 418-20.
176. Feng, Z., et al., *A pathogenic picornavirus acquires an envelope by hijacking cellular membranes.* nature, 2013. **496**(7445): p. 367-371.
177. Aragonès, L., et al., *Fine-tuning translation kinetics selection as the driving force of codon usage bias in the hepatitis A virus capsid.* PLoS Pathog, 2010. **6**(3): p. e1000797.
178. Cohen, L., D. Bénichou, and A. Martin, *Analysis of deletion mutants indicates that the 2A polypeptide of hepatitis A virus participates in virion morphogenesis.* Journal of virology, 2002. **76**(15): p. 7495-7505.
179. Tesar, M., et al., *Analysis of a potential myristoylation site in hepatitis A virus capsid protein VP4.* Virology, 1993. **194**(2): p. 616-626.
180. Zhu, L. and X. Zhang, *Hepatitis A virus exhibits a structure unique among picornaviruses.* Protein Cell, 2015. **6**(2): p. 79-80.
181. Rowlands, D.J., *Human hepatitis A virus is united with a host of relations.* Proceedings of the National Academy of Sciences, 2015: p. 201520121.

182. Kaplan, G., et al., *Identification of a surface glycoprotein on African green monkey kidney cells as a receptor for hepatitis A virus.* EMBO J, 1996. **15**(16): p. 4282-96.
183. Dotzauer, A., et al., *IgA-coated particles of Hepatitis A virus are translocalized antivectorially from the apical to the basolateral site of polarized epithelial cells via the polymeric immunoglobulin receptor.* J Gen Virol, 2005. **86**(Pt 10): p. 2747-51.
184. Kaplan, G., et al., *Identification of a surface glycoprotein on African green monkey kidney cells as a receptor for hepatitis A virus.* The EMBO Journal, 1996. **15**(16): p. 4282.
185. Yuan, S., et al., *TIM-1 acts a dual-attachment receptor for Ebolavirus by interacting directly with viral GP and the PS on the viral envelope.* Protein & cell, 2015. **6**(11): p. 814-824.
186. Lin, J., et al., *Structure of the Fab-labeled "breathing" state of native poliovirus.* Journal of virology, 2012. **86**(10): p. 5959-5962.
187. Plevka, P., et al., *Neutralizing antibodies can initiate genome release from human enterovirus 71.* Proceedings of the National Academy of Sciences, 2014. **111**(6): p. 2134-2139.
188. Hewat, E.A., et al., *Structure of the complex of an Fab fragment of a neutralizing antibody with foot‐and‐mouth disease virus: positioning of a highly mobile antigenic loop.* The EMBO Journal, 1997. **16**(7): p. 1492-1500.
189. Springer, T.A. and J.-H. Wang, *The three-dimensional structure of integrins and their ligands, and conformational regulation of cell adhesion.* Advances in protein chemistry, 2004. **68**: p. 29-63.
190. Wang, X., et al., *Potent neutralization of hepatitis A virus reveals a receptor mimic mechanism and the receptor recognition site.* Proc Natl Acad Sci U S A, 2017. **114**(4): p. 770-775.
191. Xiao, C. and M.G. Rossmann, *Interpretation of electron density with stereographic roadmap projections.* Journal of structural biology, 2007. **158**(2): p. 182-187.
192. Toyoda, H., et al., *A second virus-encoded proteinase involved in proteolytic processing of poliovirus polyprotein.* Cell, 1986. **45**(5): p. 761-70.
193. Lu, H.H., et al., *Analysis of picornavirus 2A (pro) proteins: separation of proteinase from translation and replication functions.* Journal of virology, 1995. **69**(12): p. 7445-7452.
194. Foeger, N., W. Glaser, and T. Skern, *Recognition of eukaryotic initiation factor 4G isoforms by picornaviral proteinases.* J Biol Chem, 2002. **277**(46): p. 44300-9.
195. Gradi, A., et al., *Proteolysis of human eukaryotic translation initiation factor eIF4GII, but not eIF4GI, coincides with the shutoff of host protein synthesis after poliovirus infection.* Proc Natl Acad Sci U S A, 1998. **95**(19): p. 11089-94.
196. Probst, C., M. Jecht, and V. Gauss-Muller, *Intrinsic signals for the assembly of hepatitis A virus particles. Role of structural proteins VP4 and 2A.* J Biol Chem, 1999. **274**(8): p. 4527-31.
197. Morace, G., et al., *The unique role of domain 2A of the hepatitis A virus precursor polypeptide P1-2A in viral morphogenesis.* BMB Rep, 2008. **41**(9): p. 678-83.
198. Palmenberg, A.C., et al., *Proteolytic processing of the cardioviral P2 region: primary 2A/2B cleavage in clone-derived precursors.* Virology, 1992. **190**(2): p. 754-62.
199. de Felipe, P., et al., *Use of the 2A sequence from foot-and-mouth disease virus in the*

generation of retroviral vectors for gene therapy. Gene Ther, 1999. **6**(2): p. 198-208.

200. Li, L., et al., *PLA2G16 promotes osteosarcoma metastasis and drug resistance via the MAPK pathway.* Oncotarget, 2016. **7**(14): p. 18021-35.
201. Wang, H., et al., *Effect of the LPA-mediated CXCL12-CXCR4 axis in the tumor proliferation, migration and invasion of ovarian cancer cell lines.* Oncol Lett, 2014. **7**(5): p. 1581-1585.
202. Lee, S.C., Y. Fujiwara, and G.J. Tigyi, *Uncovering unique roles of LPA receptors in the tumor microenvironment.* Receptors Clin Investig, 2015. **2**(1).
203. Staring, J., et al., *PLA2G16 represents a switch between entry and clearance of Picornaviridae.* nature, 2017. **541**(7637): p. 412-418.
204. Walter, T.S., et al., *A plate-based high-throughput assay for virus stability and vaccine formulation.* Journal of virological methods, 2012.
205. Anantharaman, V. and L. Aravind, *Evolutionary history, structural features and biochemical diversity of the NlpC/P60 superfamily of enzymes.* Genome Biol, 2003. **4**(2): p. R11.
206. Pang, X.Y., et al., *Structure/function relationships of adipose phospholipase A2 containing a cys-his-his catalytic triad.* J Biol Chem, 2012. **287**(42): p. 35260-74.
207. Lasch, J., et al., *Fluorometric assays of phospholipase A2 activity with three different substrates in biological samples of patients with schizophrenia.* Clin Chem Lab Med, 2003. **41**(7): p. 908-14.